



THESE DE DOCTORAT DE L'UNIVERSITE DE LYON
opérée au sein de
l'Université Claude Bernard Lyon 1

**Ecole Doctorale N° 52
de Physique et d'Astrophysique (PHAST)**

Soutenue publiquement le 15 Octobre 2015 par
Menka STOJANOVA

**Non-trivial aftershock properties in
subcritical fracture and in earthquake
dynamics**

Devant le jury composé de:

M. Daniel BONAMY	CEA Paris	Rapporteur
M. Jay FINEBERG	RIP Jerusalem	Rapporteur
M. Osvanny RAMOS	ILM Lyon	Codirecteur de thèse
M. Mohamed R'MILI	INSA Lyon	Invité
M. Renaud TOUSSAINT	IPG Strasbourg	Président
M. Loïc VANEL	ILM Lyon	Directeur de thèse

THANK YOU ...

It is impossible to thank properly all the people who have helped me to and through the PhD, without writing acknowledgments longer than this manuscript itself. I hope that this shortened version will still let you know how grateful I am.

To begin with the end, I would like to thank the members of the jury. I was honored to have a jury of such notoriety, even though its members were chosen for affability, not reputation. I thank Jay Fineberg and Daniel Bonamy for accepting to be the referees of this thesis and for turning the dreadful question session into a pleasant conversation. I thank Renaud Toussaint, the jury's president for his pertinent comments and the way he puts things in new perspectives. More importantly, I thank him for my internship he supervised a few years ago: it is under his guidance that I first felt like a scientist, and not a student.

My deepest gratitude is to my advisors. They made me want to do research five years ago and supported me ever since; it was nice feeling as part of a team, and knowing that someone has my back.

When looking for someone to mentor my first internship, being new and not knowing anyone in Lyon, I naturally turned to the professor I liked the most that year. I thank Loïc for being that professor, because I stopped being afraid of hydrodynamics and also because without it I probably never would have worked here. The kindness and patience he showed during the thesis put me in good conditions for exploring, and his feet-on-the-ground approach helped me keep on track when things got dispersed.

Osvanny is the advisor all students long for, for he is an audacious scientist, an excellent mentor and a generous friend. Despite his passion and devotion to his work he never let his ambitions become my burden. He showed outstanding understanding during my few rough times and was enthusiastic and available when work was good. I could thank him for so many things, but if it had to be one, I'd thank him for showing me how to observe without judging.

I thank Stéphane, who called himself a “privileged collaborator” but was an advisor to me, for his support and relentless joy whether at work or not. I regret that we did not collaborate more, and hope we will eventually get to see each-other more often.

I thank Rémy for the unfinished but interesting projects we started, Frédéric who generously lent us the fast camera and Mohamed R'Mili and Nathalie Godin for the collaboration at INSA that made for a chapter of this thesis.

The youngsters of “the fracture team” also have their share of responsibility in this work. A big thanks to Ramon, for without him I would have been forced to learn LabView, and to Marie-Julie, Gaël, Alexis and Hadil that shared the lab and a few laughs with me. I thank Sébastien, my closest teammate for the beers in King Kong, meals in the coffee room, walks home, the moving of my piano (two and a half times!), the hopeless afternoons in the cave and for sticking there for better and worse.

Moving to the bigger scale, the “liquids and interfaces and biophysics” group(s)

was a great team to be a part of, one that makes you feel at home. Many thanks to the “permanents” - Anne-Laure, Catherine B., Mathieu, Charlotte, Christophe P., Cécile, Hélène, Agnès, Marie, Gilles, Rémy, Osvanny, Christophe Y., Lydéric, François, Jean-Paul, Thomas, Loïc and Laurent for installing this atmosphere. I will always cherish the discussions we had with Luc, who spread kindness and wisdom in the lab. Thank you to the ones that welcomed my generation of students: Baudoin - who also welcomed some of us in Rennes, Henri, Xixi, Isaac, Pauline, Antoine, Nico W., Clara and Oriane; and to the ones that came the following years: Alex - who always seemed happy, Loren, Sébastien, Félix, Florence, Andrea, Baptiste, Nico B., Elisa, Pascal - the wisest post-doc that ever set foot on Earth, Ronan, Quentin, Marie-Emelyne, Teresa - who I hope will keep the good spirit, Tess - that I would have loved to know more, Angélique - the great cook and kind officemate, Calina and Manon. I thank Ludivine, for all the times she has listened to me, and for being the one to start our friendship.

Thank you to our three neighbors - Nora, Julien and Antoine for bringing change and fresh ideas to the Brillouin building. For years now Antoine has been my person of choice for confessions, and our coffee breaks, even though rare, kept my spirit up.

I was lucky to work with a few excellent teaching teams during the past years. I am grateful to all the people I collaborated with, and in particular to Franck Rabilloud, for being supportive with the teachers and considerate with the students.

Thank you to Fabio, Ruben, Delphine and Christelle, for arranging my mess whenever it was needed and never complaining about it. Their support is precious to all of us.

Thank you to Bojana, Marija, Seb, Joseph, Laura and Simon for proof-reading this thesis, even its most boring parts.

I thank also the most tenacious of my friends, the ones that supported me even at distance and whose visits were always a joy: Antoine (again), Cécile, Emma, Gabriel and Laura.

Thank you to Kevin for everything we shared during so many years and at the beginning of this work.

I would have never gone to France without the support of my family, and in particular my parents, who always made us think and choose. Many thanks to Bojana, for being my first and wisest advisor, to Marija for coming to Lyon at the right time to put up with me at the end of the thesis and to Anika for the family weekends that felt like home.

I could never thank enough the last-year ker-students of the team for the three years we spent together and for making the writing of the thesis so much more fun. Florence, qualified as a last-year student by her state of mind, was always there to understand my complaints. Knowing Alexis on the other side of “the hole” late at night kept me sane during the last few months of the thesis. I thank him for always sharing his calm, optimism and french fries. Catherine’s subtle mixture of honesty and diplomacy make for an excellent friend, and without her organization skills many of our trips would have been less interesting. Joseph’s absurd sense of humor animated the office since the very first day, keeping his open mind and tolerance hidden for a few months. I thank him for his silent support throughout

these years.

Finally, I thank Simon whose presence, passion for science and availability to talk helped with many aspects of this thesis. His pertinent yet delicate comments have improved the manuscript, and his encouragements and serenity improved my state of mind. I am lucky we ended this journey together and look forward to what follows.

RÉSUMÉ EN FRANÇAIS

Propriétés non-triviales des répliques dans la fracture sous-critique et dans la dynamique des tremblements de terre

Cette thèse s'intéresse à deux phénomènes invariants d'échelle : la fracture sous-critique dans les milieux désordonnés et les tremblements de terre. Bien que se déroulant sur des échelles complètement différentes, ces deux processus sont issus de mécanismes très similaires, et présentent donc des propriétés statistiques proches. Ils sont tous les deux caractérisés par une dynamique intermittente. Nous pouvons ainsi définir des événements discrets (sismiques ou de fracture), caractérisés par leur énergie et par leur temps d'occurrence. Ces deux grandeurs sont distribuées en suivant des lois de puissance sans avoir d'échelle caractéristique. Les exposants de ces lois sont un indicateur important de la dynamique du processus, et sont liés aux autres caractéristiques du système étudié. Ces exposants, leurs variations et interdépendance sont le sujet principal traité ici.

Expériences sur la fracture sous-critique

Le premier travail décrit dans cette thèse est une étude expérimentale de la fracture sous-critique du papier. Nous avons observé la propagation d'une fissure unique dans une feuille de papier par deux méthodes indépendantes: un suivi visuel et un suivi des émissions acoustiques. Initialement le but de ce travail était de vérifier la fiabilité du suivi acoustique des fractures, et de comparer les informations que l'on peut en tirer avec celles obtenues par le suivi visuel. Les études comparatives de ce genre sont très rares, bien que le suivi des émissions acoustiques est une méthode largement utilisée dans le génie civil. Nous avons observé la propagation d'une fissure unique dans une feuille de papier soumise à une force constante appliquée par un poids mort. La force appliquée sur la feuille est choisie de façon à ce que la fracture soit lente (avec une durée de 10 minutes à quelques heures avant la rupture totale de la feuille). Le papier étant un milieu désordonné constitué de fibres de taille et orientation différente, la fracture se fait de façon intermittente. Visuellement on observe une fracture qui n'avance pas la plupart du temps, et effectue de temps en temps des sauts discrets. Concernant le signal acoustique, il est la plupart du temps est au niveau du bruit, mais présente des bursts acoustiques séparés dans le temps. Nous définissons ainsi des événements de rupture, soit visuels soit acoustiques, caractérisés par leurs énergies et par les temps d'attente qui les séparent.

C'est aux distributions statistiques de ces énergies et ces temps d'attente que nous nous sommes intéressés. Dans les deux cas (visuel et acoustique) ces deux grandeurs sont distribuées en loi de puissance. Les distributions des temps d'attente visuels et acoustiques ont des exposants quasiment identiques, et proches de 1. En revanche, les distributions des énergies ont des exposants significativement différents, avec un exposant plus bas pour les énergies détectées visuellement. Nous avons observé que cette différence est liée la différence des fréquences des deux acquisitions (10 Hz pour le suivi visuel, et 2 MHz pour le suivi acoustique). Cette dépendance de l'exposant avec la fréquence d'observation est due à l'existence des corrélations temporelles, à savoir des répliques, dans le signal de rupture: tandis qu'un suivi à haute fréquence (acoustique) permet d'observer chaque événement séparément et de

déterminer exactement l'exposant de la distribution des énergies, un suivi à basse fréquence (visuel) ne permet pas de distinguer les répliques de l'événement qui les précède, résultant en un exposant plus bas.

La fracture des mèches de fibre de verre est une expérience de corrosion de sous contrainte, i.e. un cas particulier de la fracture sous-critique, où l'action conjuguée de la contrainte et d'une réaction chimique agressive vis-à-vis du matériau provoque la propagation d'une fracture. Dans le cas du verre, ce sont les liaisons Si-O-Si dont l'angle d'ouverture augmente sous l'effet de la contrainte et qui ensuite se font attaquées par les molécules d'eau. Nous avons étudié la fracture d'une mèche de 2 000 fibres sous déformation constante (donc à force par fibre constante) et immergée dans l'eau. Les fibres se cassent de façon discrète, le plus souvent une par une. Les temps de fracture sont distribués en lois de puissance, analogue à la loi d'Omori en séismologie. Nous avons étudié la variation de cet exposant en fonction de la contrainte imposée et de la température de l'eau. Les résultats obtenus ont été comparés avec un modèle de rupture de fibres thermiquement activée. Ce modèle, prenant en compte les fluctuations thermiques et le désordre de la mèche (avec une distribution gaussienne des seuils de rupture des fibres) s'est montré insuffisant pour reproduire les résultats expérimentaux, et devra être modifié pour prendre en compte le vieillissement des fibres de verre au cours de l'expérience.

Analyse des données sismiques

Le travail sur les séismes a été inspiré par les résultats obtenus sur la fracture dans le papier. En effet, les tremblements de terre sont aussi des événements discrets, caractérisés par des énergies distribuées en loi de puissance et de fortes corrélations temporelles. Nous avons donc voulu vérifier si dans le cas des séismes on observe aussi une diminution de l'exposant de la loi de puissance des énergies avec la diminution de la fréquence d'analyse du signal. Ce comportement a en effet été observé pour des données expérimentales des tremblements de terre et aussi pour une simulation par modèle par processus ponctuels (point process model). Plus exactement, lorsque la fréquence d'analyse du signal diminue, la distribution des énergies se sépare en deux lois de puissance : une partie des énergies suit une nouvelle distribution avec un exposant plus bas et l'autre partie reste avec sa distribution d'origine. Si la fréquence d'analyse est assez basse, uniquement la nouvelle loi de puissance est détectée. Ce résultat permet de généraliser ce qui a déjà été observé dans le cas de la fracture du papier, confirmant l'importance de la fréquence d'acquisition lors de l'observation des processus présentant des corrélations temporelles. Nous avons ensuite établi une relation empirique permettant de relier l'exposant des énergies biaisé à l'exposant des énergies d'origine et l'exposant de la distribution des temps d'occurrence. Ce résultat pourrait permettre de déterminer, à partir d'une mesure à basse fréquence, l'exposant d'origine des énergies des événements.

Nous avons ensuite abordé un sujet récent sur les tremblements de terre, portant sur la corrélation des magnitudes. Tandis que la corrélation temporelle entre les séismes (précurseurs et répliques) est bien connue, récemment des études ont suggéré que des corrélations existent aussi entre les magnitudes, à condition que les événements soient rapprochés dans le temps et l'espace. Depuis une dizaine d'années la discussion sur la validité de cette idée est ouverte, certains auteurs suggérant que

l'impression de corrélation est un artefact dû à des problèmes de détection. Nous avons utilisé des données des catalogues sismiques du Japon et de Californie pour étudier cette question. Nous avons montré, en utilisant une méthode qui permet de s'affranchir des corrélations temporelles des séismes, que dans une séquence de répliques associée à un séisme fort la fraction des grosses répliques est plus importante au début qu'à la fin de la séquence. Ce résultat s'explique par une corrélation entre les magnitudes (du choc principal d'un côté et les magnitudes des répliques de l'autre) qui diminue dans le temps et confirmerait donc l'existence de cette corrélation.

CONTENTS

Introduction	1
I Experiments on subcritical fracture	11
1 Fracture propagation in paper. The effects of time correlation	13
2 Fracture of a fibre bundle: experiments and model	31
II Earthquake statistics	51
3 Some history and a few technicalities	53
4 b-value and the frequency of analysis	75
5 Early aftershocks	91
Conclusion	105
Appendices	107

INTRODUCTION

1	Subcritical fracture	3
1.1	Stress concentration	3
1.2	Griffith's energy balance	4
1.3	The role of the disorder	5
2	Fracture and earthquakes	6
3	Power laws	7
3.1	Power-law distributed energies	
The Gutenberg-Richter law		8
3.2	Power-law distributed occurrence times	
The Omori law		9
4	Thesis summary	9

Understanding how things break is a matter of general interest. The practical reasons are obviously related to safety issues: fracture is part of everyday life, but when unwanted it can be disastrous. Hence, scientists have been studying fractures for decades, trying to understand what drives them, how they propagate, why do they follow certain patterns, and if they can be stopped or predicted.



Figure 1: (a) Fracture in a paved street in San Francisco, California, caused by the large earthquake that occurred on 18 April 1906. (b) A cracked mug. This kind of fracture usually becomes visible after a mild shock, and then increases as the mug is used and sustains repeatable shocks, until the mug breaks completely. Copyright 2015 Cherrico Pottery, LLC.

Creating a fracture takes energy, and depending on the rate at which the energy is brought to the system fracture can occur instantaneously or slowly. A sudden introduction of sufficient amount of energy can make an object break (in two or more pieces) quasi-instantaneously. For an example, think of a falling mug reaching the floor, a poked inflated balloon, or an explosion. Figure 1.a presents one such fracture, occurred in San Francisco, where displacement due to the earthquake of 1906 provoked fractures in the soil for dozens of meters. Now if there is some energy available for fracture, but not enough for an instantaneous one, the object can still fail, but this takes time. An every day example is a cracked mug (figure 1.b). The small shocks it experiences from time to time can make a small fracture slowly grow into a visible crack. As the crack grows stress intensifies at its tip, and the fracture can propagate more easily.

Slow fracture, and in particular slow fracture of disordered materials, is the central subject of this thesis. This introductory chapter reviews some of the important basis about this phenomenon, starting with the importance as well as the mechanisms of subcritical fracture.

1 Subcritical fracture

From a practical point of view, subcritical fracture is particularly dangerous because of its temporal delay - it can develop for years without being noticed, until failure occurs unexpectedly. When the object in question is a building or a bridge, the consequences can be catastrophic.

A textbook example of subcritical fracture are the Liberty Ships - a class of about 3000 cargo ships, constructed in the USA during World War II. Almost half of them presented damages due to brittle fracture until April 1946. More than 200 sank or were damaged beyond all hope of repair, and 12 spectacularly broke in half without any warning signals (figure 2.a). It is thought that fracture occurred because of poor welding and stress concentration in the vicinity of welding beads. A more recent example is the roof of the terminal E at the Charles de Gaulle airport in Paris which collapsed in 2004, 11 months after its inauguration (figure 2.b). Investigation showed that fractures propagated subcritically in the concrete blocks constituting the roof's vault, pressured by the metal support structure which pierces through the concrete blocks.

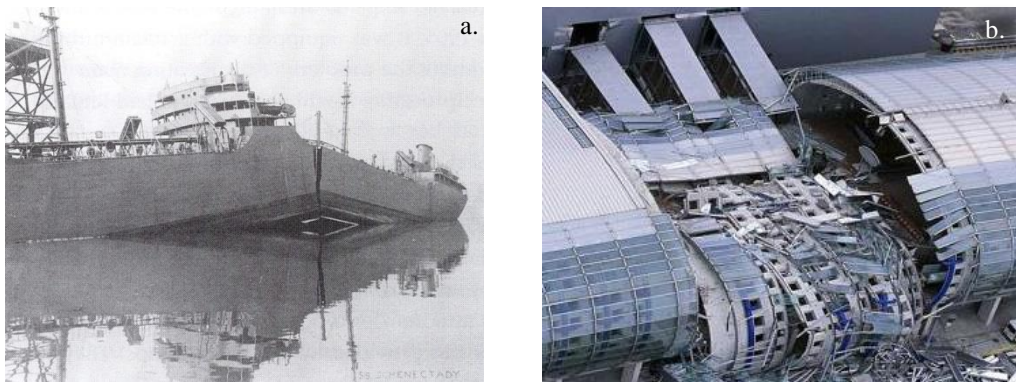


Figure 2: (a) One of the liberty ships, built in the USA during World War II, which broke in half due to subcritical fracture propagation.

The Design and Methods of Construction Of Welded Steel Merchant Vessels U.S. GPO (1947) (b) Terminal E of the Charles de Gaulle airport, whose roof collapsed in 2004 due to subcritical fracture propagating in its concrete blocks.

Report Berthier/ Ministry of Transport

The delayed fracture of solids under low stress has been studied for decades. The key element lies in the *stress concentration*: some parts of the solid (in particular in the vicinity of crack tips) can experience stresses much greater than the one applied globally.

1.1 Stress concentration

In 1913 Inglis analysed the stress distribution around a flaw in a material. He showed that for a two-dimensional material containing an elliptic crack with a length l and a radius of curvature ρ_c at one of its edges (figure 3), submitted to a stress σ , the

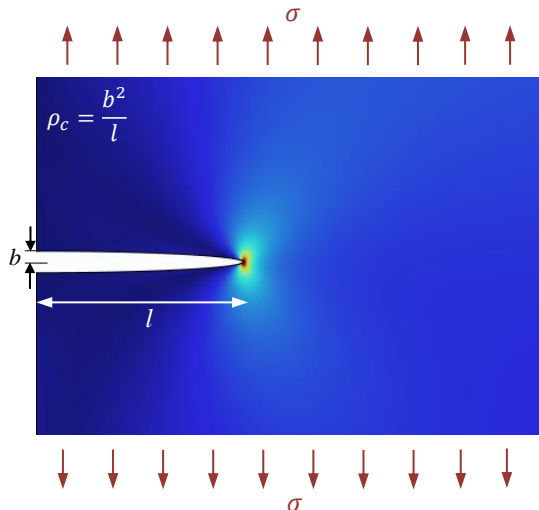


Figure 3: Schematic representation of a 2D solid containing an elliptical crack on one edge, submitted to a stress σ . The color code of the solid represents the local stress level, calculated by finite element method.

stress at the crack tip is:

$$\sigma_c = \sigma \left(1 + 2\sqrt{\frac{l}{\rho_c}} \right). \quad (1)$$

This shows that the maximal stress experienced by the material can be much greater than the globally applied stress. For example, the stress at the tip of a crack with a width of the order of $10 \mu\text{m}$ and a length of 1 cm^1 will be about 65 times greater than the applied stress. Figure 3 shows a simulation of a 2 dimensional material containing an elliptic crack on one edge, the different colors representing the stress level. The maximum of the stress is immediately at the crack tip and the stress decreases rapidly as the distance from the tip increases.

Hence, the maximum stress that a loaded material sustains is not only given by the average stress it is submitted to, but also by the length and shape of its flaws. This can be generalised by introducing the *stress intensity factor*:

$$K = \sigma\sqrt{l\alpha}, \quad (2)$$

where α is a geometrical correction factor. The toughness K_{IC} , defined as the maximum stress intensity factor which can be sustained in mode I fracture (figure 5) is a material characteristic.

1.2 Griffith's energy balance

Using a thermodynamic approach, Griffith [46] showed that once a fracture has nucleated in a body, and as long as the body is loaded, its only stable configuration is at complete failure. We consider a two-dimensional elastic body with a Young modulus Y , a surface tension γ and containing a crack with length l . A constant stress σ is applied at the outer boundary of the body (figure 4.a). Two contributions need to be taken into account for the energy balance. When a crack propagates, the

¹These dimensions correspond approximately to paper cracks which we will study in chapter 1.

mechanical energy U_E stored in the body decreases by an amount $\pi^2\sigma^2/Y$ and the surface energy increases by $2\gamma l$. Hence, the total system energy related to fracture propagation writes

$$\Delta U = -\frac{\pi l^2 \sigma^2}{Y} + 2\gamma l. \quad (3)$$

The fracture energy calculated by Griffith for a glass sample is represented on 4.b as a function of the fracture length l . Gray lines represent the mechanical (U_E) and surface (U_S) energy involved with fracture propagation, and the black line is their sum, i.e. the total fracture energy (U). The energy passes through a maximum for a critical length l_c , l_c depending on the value of the stress σ and material properties. Beyond this length the fracture propagates spontaneously and rapidly until the whole body fails.

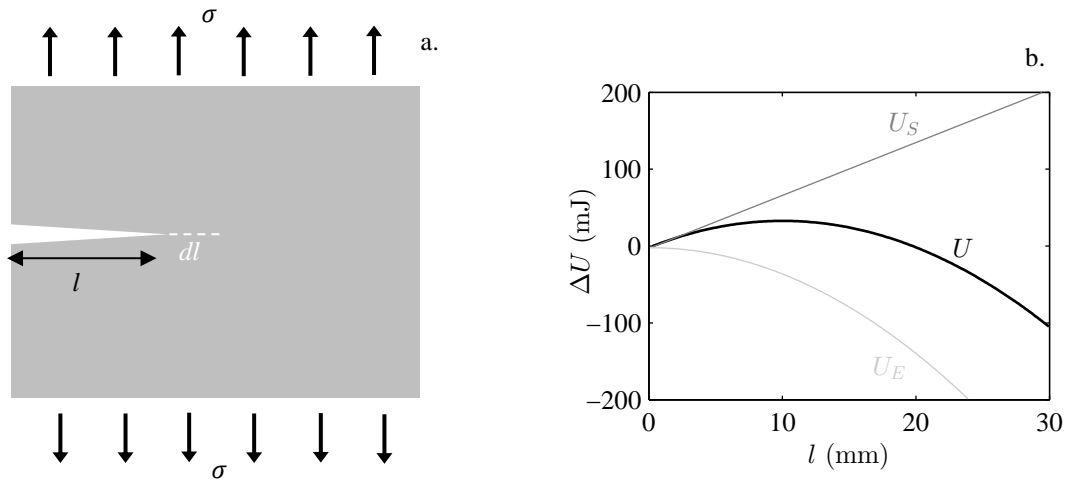


Figure 4: (a) Schematic representation of a 2D solid with a fracture of length l . (b) Representation of Griffith's calculation for fracture energy of glass.

If $l < l_c$ some energy input is needed for the fracture to advance. This *activation energy* can be brought by thermal fluctuations (see [145] and references therein). The slow crack propagation resulting from this process is the subcritical fracture propagation we are interested in.

1.3 The role of the disorder

Now let us consider a subcritical fracture propagation in a heterogeneous material. A structural heterogeneity of the material can induce heterogeneity of its toughness, which gives rise to some specific behaviours [15]. Since the material is heterogeneous there exist preferential, less energy-costly paths for the fracture to follow. This results in a rough crack surface [80, 107, 123]. Also, when encountering a high toughness region the crack can be arrested. It gets pinned until a large-enough energy input (like thermal or mechanical fluctuations) allows it to propagate further. This succession of pinning-depinning states is at the origin of the *intermittent dynamics* observed for fracture of heterogeneous materials [24, 78, 122]. The intermittent dynamic of fracture will be recurrently observed in this thesis, whether it comes to fracture experiments or earthquake statistics.

2 Fracture and earthquakes

More than half a century ago Mogi [87–89] conducted a series of studies on rock fracture, and observed a remarkable similarity between rock fracture and earthquakes, concerning the statistics and dynamics of these processes. The rocks broke in an intermittent manner, generating discrete fracture events. The time-series of these events showed the existence of earthquake-like phenomena (foreshocks and aftershocks), and the probability distributions of their energies and occurrence times are analogue to the ones of earthquakes. Few years later Scholz [126] refers to Mogi's work saying that “*the mechanism of shallow earthquakes is apparently some sort of fracture process*”.

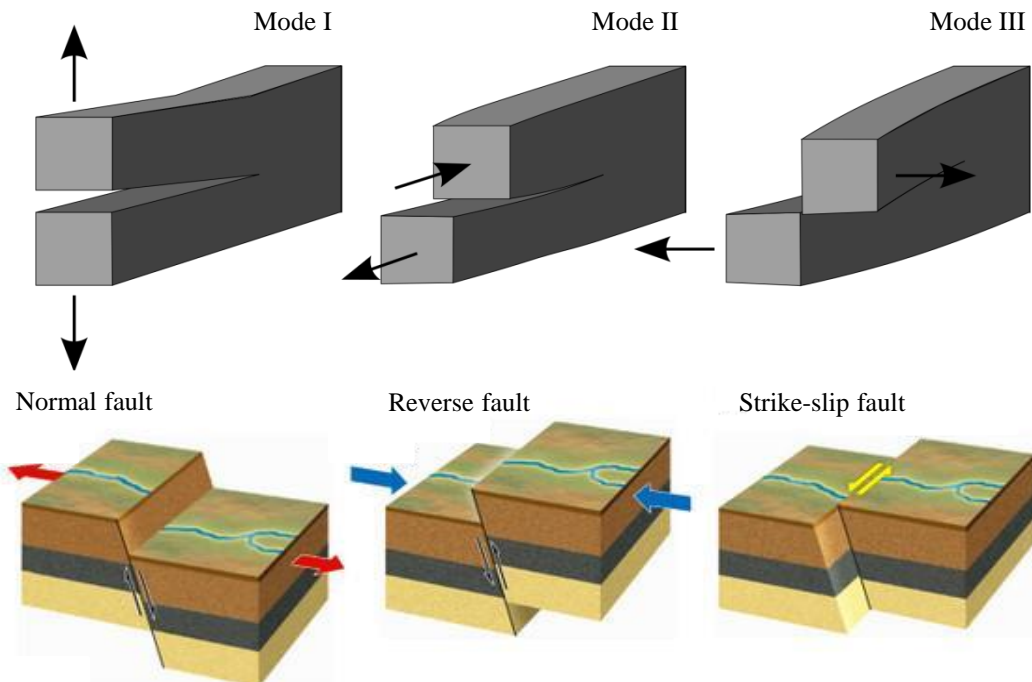


Figure 5: Illustration of the three fracture modes (top) and the three fault types (bottom). One can see that fault movements are combination of mode II and mode III fracture.

Nowadays we have more information about earthquake mechanisms than at the beginning of Mogi's work. The similarity between the friction of two compressed and sheared plates (an earthquake-like configuration) and fracture has been deeply studied [12, 19, 113, 114, 140]. We know that earthquakes result from fault motion, and the three fault types - normal, reverse and strike-slip - are simply combinations of mode II and III fractures (fracture modes and fault types are represented on figure 5). Hence it is not surprising that earthquakes and fracture present many similarities in their behaviour. In the laboratory, it is possible to generate fractures with similar statistics to the ones shown in real earthquakes. Comparing earthquake data with fracture experiments has become a common procedure [5, 55, 98, 146, 147]. In theoretical studies fracture mechanics is systematically used for explaining earthquake mechanisms [127].

3 Power laws

Both in earthquakes and subcritical fracture in disordered materials the events are distributed following a power law. Here we will review some generalities about power laws, then some of their specificities related to fracture.

Mathematically, a quantity A follows a power law if it is drawn from a probability distribution

$$p(A) \propto A^{-\beta}, \quad (4)$$

where β , the *exponent* is a constant and a parameter of the distribution. In the case of $\beta > 0$, this means that the probability of observing a certain value for x dramatically decreases as the value increases: small values of x are much more probable than large ones. Power law distributions are usually plotted in log-log coordinates because $\log(p(A)) = -\beta \log(A) + \log(\text{cst})$, so the distribution appears as a straight line. This can be seen on figure 6, representing the (non-normalised) probability of earthquake amplitudes in an aftershock sequence in Japan. The beginning and the end of the sequence are represented separately, and one can see that they follow power laws with slightly different exponents.

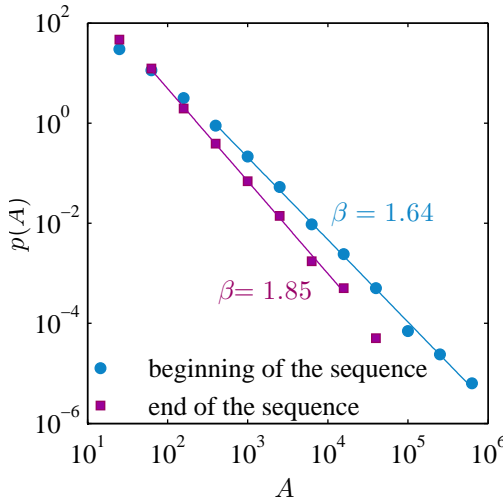


Figure 6: Power-law distributions of the amplitudes ($10^{\text{magnitude}}$) of aftershocks following the magnitude 7.6, 11 March 2011 Tohoku earthquake (the mainshock of this sequence is itself an aftershock of the great Tohoku earthquake which occurred the same day). Light circles represent the distribution of the first 3000 aftershocks of the sequence, and dark squares the second 3000 aftershocks.

The subcritical fracture process results in discrete fractures which represent intermittent energy release. Other processes, like snow or granular avalanches [4, 13, 40], solar flares [14], stock market crashes [42] or epileptic seizures [101] also result in sudden discrete bursts distributed over power laws. There is no universal theory explaining the generation of these power-law avalanches. Self-organised criticality [7] was considered the best known attempt for one, linking power-law distributed bursts to a self-organisation of a system towards a critical state, without any parameter tuning. Nevertheless, the universality of the theory was quickly questioned since experiments showed that some parameters (like the grains' shape or disorder) do need tuning [4, 40, 69] for the system to attain a power law distribution of events, which was considered by the authors the signature of a critical state.

Disorder is an important ingredient for generating a power-law behaviour. Experiments in granular piles [4] and earthquake models [110] have shown that when a system loses its disorder, it also loses the power-law behaviour. For example, the subcritical fracture of polymer films has shown a continuous crack propagation [22].

This also stands for earthquakes, which seem to deviate from the power-law distribution of their energies when the system loses heterogeneity. When the distribution of earthquakes energies is calculated in a region, it follows a power law. Nevertheless, if only earthquakes coming from one fault are considered, two possibilities exist for the energy distribution of earthquakes [138]. If the fault is relatively young and has large fault-trace complexity, it will slip by generating events distributed over a power law. If it is mature, and thus smoother, power law distribution holds for small events only, and large earthquakes (corresponding to a slip of the whole fault) are more frequent than expected according to the power law. Hence, in order to observe a power law the heterogeneity of the system must be assured either by the intrinsic properties of the fault, or by the existence of several different faults.

Statistical models of fracture of heterogeneous materials reproduce the dynamics and statistical properties of the process. Among the most widely-used ones are fibre bundles, lattice models and molecular dynamic simulations (see [3, 16] and references therein). Disorder can be implemented as a heterogeneity of the networks' elements, which can eventually vary with time. The network is loaded at constant stress or constant strain, and fracture occurs intermittently.

3.1 Power-law distributed energies The Gutenberg-Richter law

The power law distribution of the energies of acoustic bursts is commonly called the *Gutenberg-Richter* distribution, referring to the first observation of power-law distributed amplitudes in earthquakes. The value of the exponent of the energy distribution, which we will denote β throughout this thesis, measures the number ratio of small to big events. The greater β is, the more numerous are small events compared to big ones.

Figure 6 shows two power-law distributions of earthquake magnitudes. One can see that a slight difference exists between the two exponents. Let us calculate the ratio of probability for great earthquake (with a magnitude between 7 and 8) occurring for each of these distributions:

$$\frac{P\{(7 < m < 8)|\beta = 1.64\}}{P\{(7 < m < 8)|\beta = 1.85\}} = \frac{[(10^m)^{-1}]_7^8}{[(10^m)^{-1.1}]_7^8} \sim 26. \quad (5)$$

Thus, a change of about 0.2 in the exponent β makes it 26 times more probable for very large earthquakes to occur, which shows why forecasting great earthquakes needs a precise determination of β . The value of β is also important since it can be an indicator of the system's state: in equal load sharing fibre bundle models β decreases from 5/2 to 3/2 with the approach of failure [109] and for earthquakes it is related to the crust's stress state [128].

3.2 Power-law distributed occurrence times The Omori law

For non-stationary processes power-law distributions can concern both the energy of the fracture events and their occurrence times. A typical example are earthquake aftershocks, whose number decreases as a power law with respect to the time from mainshock [100]. This type of power-law decelerating dynamics, which we will refer to as *Omori law* can also be observed in fracture experiments and models. The exponent of the power law p was shown to depend on the system's disorder (p decreases when disorder decreases for simulations of creep of fibre bundles [118] and rate-and-state model of earthquakes [54]). For accelerating fracture processes, like in the case of creep experiments, the number of fracture events can increase as a power law [26], often referred to as the *inverse Omori law*.

4 Thesis summary

This thesis consists in two separate parts: one on subcritical fracture experiments, and another one on earthquake statistics. The dynamics of these processes was mainly studied through their scale invariant dynamics, reflected in power law distributions of event sizes and times between events. The analyses focuses particularly on the variation of their exponent values and the origins of these variations.

Subcritical fracture was studied by two experimental set-ups: creep experiments on paper, and constant-strain fracture of fibre bundles. Paper fracture has been studied in our group for more than 10 years now by visually observing the propagation of the crack. We added acoustic emission monitoring to the experimental set-up in order to compare it to visualisation. The comparison between low frequency image analysis and the high frequency acoustic monitoring allowed to identify the importance of the frequency of analysis for temporally correlated systems, and acoustic emission monitoring revealed the existence of aftershocks in the dynamics of paper fracture.

The fibre bundle experiments concentrate on the temporal distribution of the fracture events, which follows an Omori law. We studied the influence of the temperature and stress on its exponent, and compared it with results from fibre bundle model analytical predictions and simulations.

Our work on **earthquakes** was initially motivated by the results obtained on paper fracture experiments. Hence it starts by a study of aftershock sequences, their Gutenberg-Richter exponent, and the influence of the frequency of analysis on this exponent. By lowering the frequency of the time-magnitude signal we showed that at low frequencies the exponent of the Gutenberg-Richter law depends on the exponent of the Omori law.

The last chapter of this thesis is concentrated on the early aftershocks. We inspected the evolution of the properties of an aftershock sequence with time, and observed differences between aftershock occurring shortly after a mainshock, and late aftershocks. These results can be related to the recent proposition of existence of magnitude correlations in earthquakes.

Part I

Experiments on subcritical fracture

CHAPTER 1.

FRACTURE PROPAGATION IN PAPER. THE EFFECTS OF TIME CORRELATION

1	Introduction	14
1.1	Why paper?	14
1.2	Previous creep experiments on paper	14
1.3	Motivation	15
2	The experiment	16
2.1	Data recording	17
2.2	Data analysis	17
2.3	Details about the acoustic emissions	18
3	Results	19
3.1	First observations	19
3.2	A rough comparison between acoustics and visualisation	20
3.3	Probability distributions of time and energy	22
3.4	The influence of the acquisition frequency	24
3.5	Aftershocks	26
4	Conclusion	27
5	Perspectives	28

1 Introduction

The focus of this chapter is experimental work on subcritical fracture in paper. We studied the intermittent propagation of a single fracture in a sheet of paper under constant load (figure 1.1, on the left). The fracture was observed both by direct visualisation and acoustic monitoring, in order to compare the information from these two measurements.

1.1 Why paper?

Using paper in fracture experiments is very convenient: it is cheap and industrially produced, so samples are very easy to obtain. It is quasi two-dimensional, allowing for the fracture to be visualised. It is disordered, which results in particular properties regarding slow fracture (see section 1.3 from the Introduction), in particular an intermittent fracture propagation. Hence, paper is commonly used as a model material when a two-dimensional disordered system is needed [60, 111, 112, 119–122, 124]. Details of its disordered nature can be seen when observing under microscope. Figure 1.1 shows the microscopic structure of a sheet of paper: it is a complex network of cellulose fibres with various sizes (between 4 and 50 μm and average of 18 μm [121]) and oriented in random directions.

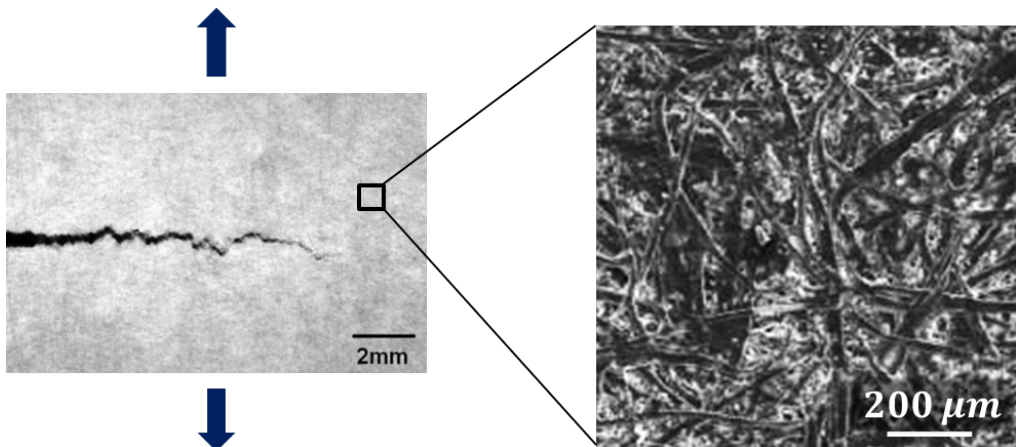


Figure 1.1: Left: photograph of fracturing paper. The arrows represent the direction of the applied force. Right: microscope image of a paper sample.

1.2 Previous creep experiments on paper

Some aspects of subcritical fracture in paper have already been studied in our group. In particular, paper fracture was studied during creep experiments on samples with a pre-existing macroscopic fracture [120–122]. Even though the samples were subjected to a force below their failure threshold, they experienced subcritical fracture. As discussed in section 1 of the introduction, the stress concentrates around the fracture's tip, and the stress intensity increases with the fracture length. The more the fracture advances the more the stress intensity increases, until reaching a critical length where the whole system fails (figure 1.2). For experiments made under the same conditions (temperature, humidity and force) the critical length l_c is well defined. The time until complete rupture τ is quite dispersed (inset of figure 1.2), but it can on average be related to the experiment's conditions. The variability of τ

as well as the propagation of the fracture itself can be explained when considering fracture as a thermally activated process.

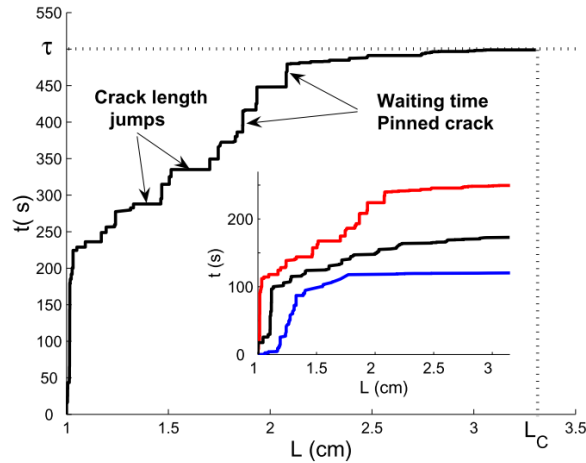


Figure 1.2: According to [121]: Typical stepwise growth curve for a creep experiment with an initial crack length $l_i = 1$ cm submitted to a constant load $F = 270$ N. The lifetime of the sample is $\tau = 500$ s and the critical length $l_c = 3.3$ cm. In inset, a strong dispersion is observed in crack growth profile and in lifetime for 3 creep experiments realised in the same conditions.

Since paper is a disordered material, the fracture will propagate intermittently, making discrete fracture jumps separated by waiting times (figure 1.2). The length of the fracture jumps was statistically analysed and it was shown that it is distributed following a power law with an exponential cut-off, with an exponent of 1.23 [124].

The experiment which will be presented in this chapter is very similar to the one we just discussed, the main difference being that this time we will combine direct visualisation with the monitoring of acoustic emissions.

1.3 Motivation

Subcritical fracture in heterogeneous materials is usually observed by either acoustic emissions (AE) monitoring [32, 43, 105, 112, 119] or direct imaging (DI) [11, 78, 111, 120–122, 124]. Both AE and DI measurements show that fracture results in a succession of discrete burst-like events (also called jumps or avalanches), whose energies and waiting times follow power law distributions. AE detection is an important tool for characterising rupture. It is a non-invasive, easy to implement method of monitoring fracture. It has been used for decades in civil engineering for monitoring the progressive damage in constructions such as bridges, dams and buildings [93, 97]. Nevertheless, the extent to which it delivers the same information on the damage amount and dynamics that the one obtained by direct visual inspection is still an open issue. To our knowledge, a comparative analysis between AE and DI was still lacking, and a combined approach has only been applied to plastic deformation so far [148]. Thus, the initial goal of the work on paper fracture was to provide such information, by directly comparing signals delivered by acoustic and visual monitoring of a fracture.

2 The experiment

We use fax paper samples from Alrey (as in Refs.[111, 120–122, 124]). The samples have a thickness of 50 μm , effective dimensions of 21×4 cm and they are attached to clamping jaws along the longer sides (figure 1.3). In order to localise the fracture and control its path, an initial crack of length ℓ_0 is prepared at one of the short free sides of the sample, both in a parallel direction and equidistant from the clamped borders. Experiments are performed by applying a constant force F perpendicularly to the direction of the initial crack. The lifetime of a sample cannot be exactly predicted, but it depends on the length of the initial crack and the intensity of the force. Once the force is applied, the fracture grows following two different regimes: a slow, intermittent regime at start, corresponding to the subcritical fracture, followed by a catastrophic, quasi-instantaneous fracture propagation. By setting $\ell_0 = 4.75$ cm and $F = 200$ N, most of the samples reached catastrophic failure within 30 minutes after the application of the force.

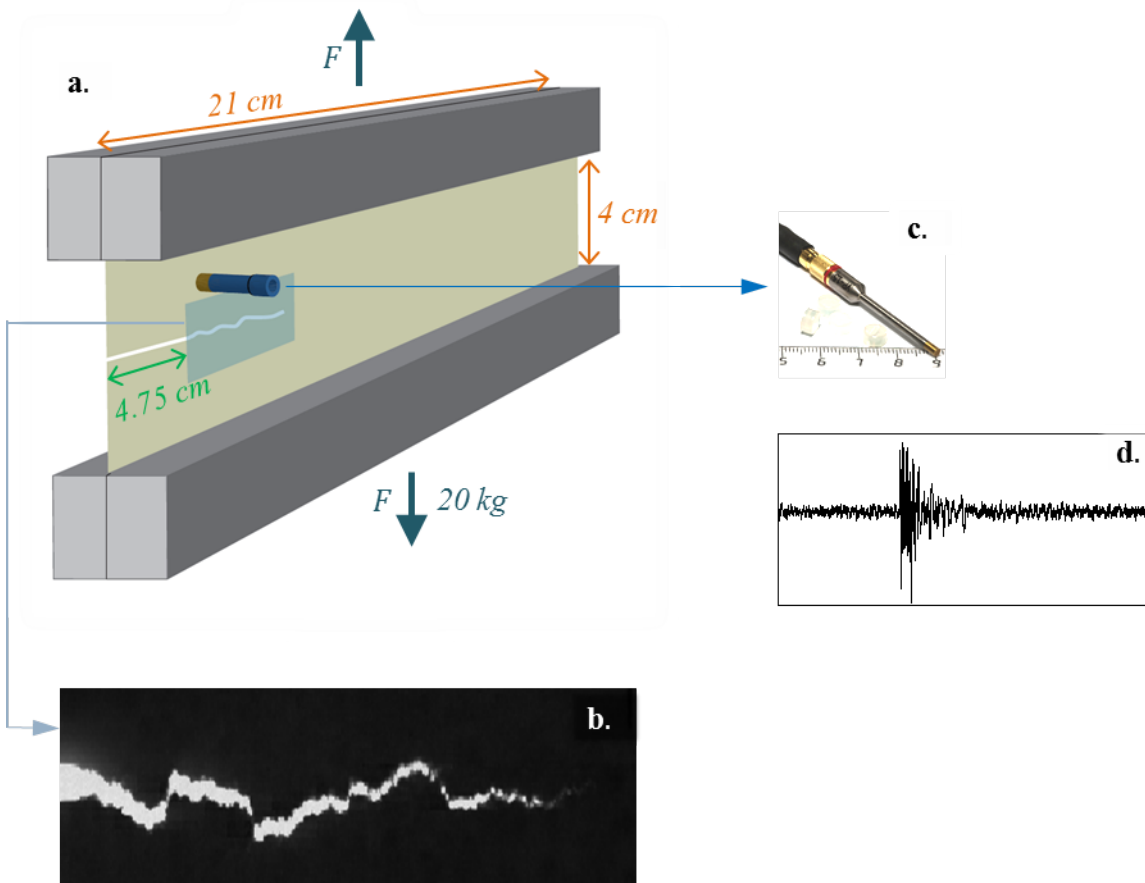


Figure 1.3: (a) Schematic representation of the experiment. (b) Typical image obtained from DI. (c) The piezoelectric transducer. (d) Typical acoustic signal containing an acoustic burst.

Nine experiments are analysed, all of them performed under the same conditions. The temperature and relative humidity were $26.5 \pm 1^\circ\text{C}$ and $45 \pm 2\%$ respectively. In these conditions Young's modulus of the sample is $Y = 2.4 \pm 0.2 \text{ GPa}$, and its toughness is $K_c = 5.3 \pm 0.2 \text{ MPa m}^{1/2}$.

2.1 Data recording

A piezoelectric transducer of diameter 2.3 mm (*Valpey Fisher VP-1.5*) is placed in contact with the paper at 5 cm from the free side containing the initial crack and at 1 cm from the fixed border (which also corresponds to a 1 cm distance to the initial crack line). An ultrasonic gel guarantees a good contact between the sensor and the sheet of paper. The AE signals are amplified by 64 dB and recorded continuously during the whole experiment by a *NI USB-6366* card at 2 MHz. A high-speed camera (*Photron FASTCAM SA4*) takes images in a rectangular area containing the advancing crack at a frequency of 10 Hz and a spatial resolution of 100 $\mu\text{m}/\text{pixel}$.

2.2 Data analysis

2.2.1 Image analysis

Crack contours are extracted using a digital image analysis routine [120]. The fracture on the images is well visible, constituting a white zone on a dark background, so contour extracting is straightforward (figure 1.4.a-c). For each image the position of the crack tip is found. In the case of disconnected islands forming the crack, the furthest point of the ensemble of all zones is defined as the crack tip. Three variables are defined to describe the crack length (see figure 1.4.d): s , the difference in real length of the interface of the fracture between two consecutive images; the size of the jump s_s , defined as the distance between the crack tip in two successive images; and s_l , defined as the projection of s on the initial direction of the crack (see its time series in figure 1.7.a).

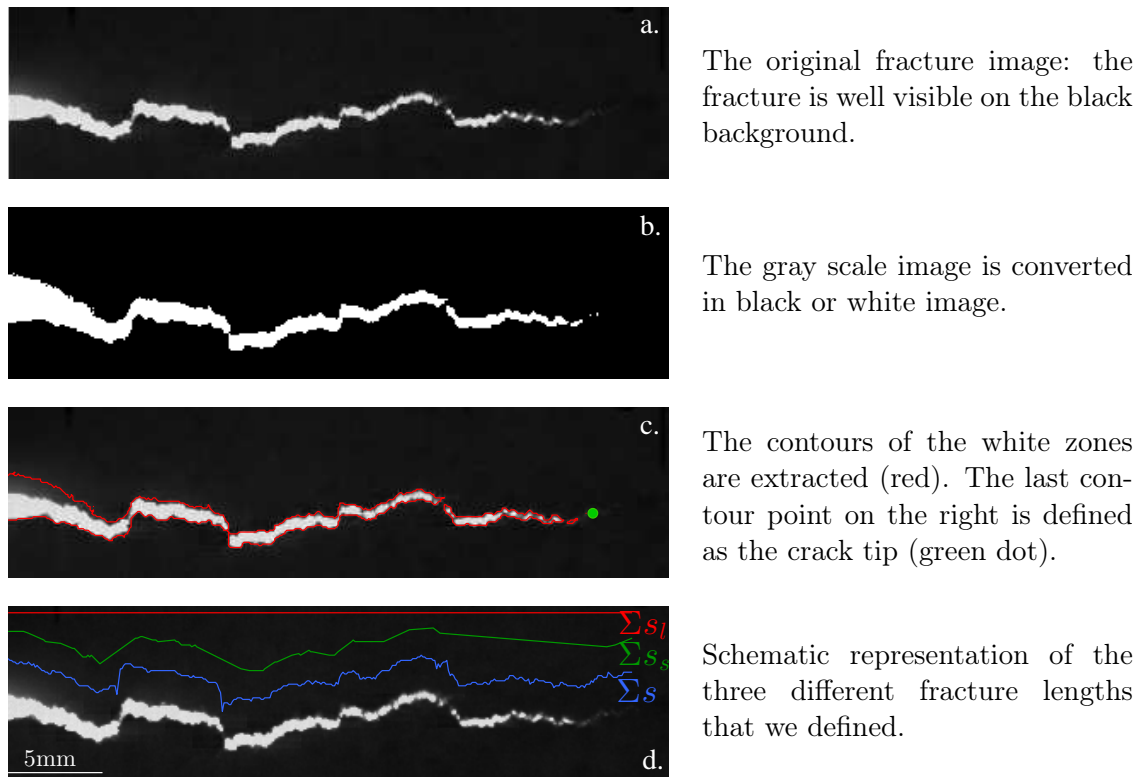


Figure 1.4: (a-c) Representation of the different steps of the fracture detection procedure. (d) The three different crack lengths that we define.

2.2.2 Acoustic emission analysis

In order to detect acoustic events we define a *spectral distance* $D_{S,N}(t)$, which is basically the difference between the power spectrum of the signal and the power spectrum of a noise signal. The spectral distance $D_{S,N}(t)$ is calculated as the integral over a time window w_d of the difference between the power spectra of the signal averaged over all the frequencies, $\langle \bar{S} \rangle_f(t)$, and the power spectra of the noise, averaged over all the frequencies and over a time interval of at least 0.5 s, $\langle \bar{N} \rangle_{f,t}$:

$$D_{S,N}(t) = \frac{1}{w_d} \int_{t-\frac{w_d}{2}}^{t+\frac{w_d}{2}} [\langle \bar{S} \rangle_f(t') - \langle \bar{N} \rangle_{f,t}] dt'. \quad (1.1)$$

$D_{S,N}(t)$ is less noisy than the signal itself (figure 1.5) and it is related to the signal's energy, rather than its amplitude. Acoustic events can be detected by imposing a threshold on $D_{S,N}(t)$. The energy of the events is calculated as the integral of the spectral distance over their duration. This technique allows to detect on average 4 times more acoustic events than a direct amplitude thresholding. Details about it are presented in the appendix A.

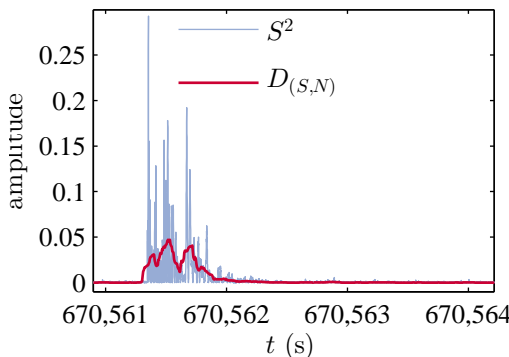


Figure 1.5: Gray line: square of the acoustic signal as delivered by the acquisition system. Red line: spectral distance of the acoustic signal from the noise.

2.3 Details about the acoustic emissions

Calibration

The amplitude of the acoustic signal depends on the contact between the transducer and the sheet of paper, which varies between different realisations. In order to compare the energy of the events from different experiments, a calibration was performed for each experiment. It consisted in normalising the AE signal by the averaged response of the sensor (E_c) to six localised rupture events produced on every sample (by piercing it with a computer controlled thin needle of 250 µm of diameter).

Attenuation

To evaluate the source energy of each acoustic event we need to characterise the attenuation of the acoustic waves in paper. An additional series of experiments was done: 10 to 20 localised rupture events were induced on a sheet of paper submitted to a force of 200 N, but with no initial crack to ensure that no uncontrolled rupture would occur. The events were made on a line parallel to the longer sides of the paper, in the same direction as the fracture in the actual experiments. The acoustic

signal was recorded by two sensors placed at 4 cm from each other. By comparing the energy ratio of signals detected by the two sensors to the distance separating each event from the sensors, we obtained that the energy is attenuated following

$$\frac{E(r)}{E_s} \sim \frac{1}{r} e^{-\frac{r}{r_c}},$$

where E_s corresponds to the energy at the source ($r \rightarrow 0$) and r_c is a characteristic length equal to 11.1 cm.

For the experiments on fracturing paper, we do not directly have access to the position of each acoustic event. To estimate the position of the source of an acoustic event we use the images and assume that it occurred at the position of the crack tip at the corresponding time. By knowing the distance between the source and the sensor, we can compute the attenuation of the energy.

Finally, the energy of an acoustic event E (see its time series in figure 1.7.b) is expressed as $E = E_s/E_c$.

Echoes

Before continuing, we assured that no echoes are detected by the acoustic monitoring, which could considerably change our results. Given the size of our samples and the velocity of the waves in the loaded paper, we estimated that the first echo of an acoustic event (reflecting from the top or the bottom clamped edge) would arrive approximately $\sim 300 \mu s$ after the original signal. For high energy events this would mean that the echo would arrive during the signal and amplify its energy. A detailed analysis of the structure of single events did not show any interference effect or secondary structure linked to the possible arrival of the echo. This can possibly be due to the interior sides of the metallic clamps being coated with rubber bands which decreases the reflectivity of the waves at the clamps.

3 Results

3.1 First observations

As the applied force is low and the material heterogeneous, we expect the initial crack to propagate in an intermittent manner (section 1.2). Indeed, images show that the length of the fracture is constant for most of the time and increases by making fast discrete crack steps - *jumps* (figure 1.6.a). Each jump constitutes a direct imaging (DI) event. The acoustic data shows discrete *bursts* with a finite duration between 180-1000 μs (see figures 1.3.d and 1.6.b). Each burst constitutes an acoustic emission (AE) event.

It can be seen on figure 1.6 that the dynamics of the fracture accelerates towards the end of the experiment. We measured a critical length $\ell_c = 7.8 \pm 0.7$ cm reached up to 30 minutes after the application of the force. ℓ_c is linked to the material toughness, defined by the critical stress intensity factor K_c and the applied constant stress σ through the relation $K_c \sim \sigma \sqrt{\ell_c}$. The regime of slow crack propagation occurring at $l < \ell_c$ will be referred to as the subcritical fracture.

Since the fracture accelerates in time, the waiting time between events decreases, until it is not possible to distinguish between acoustic events. We decided to work

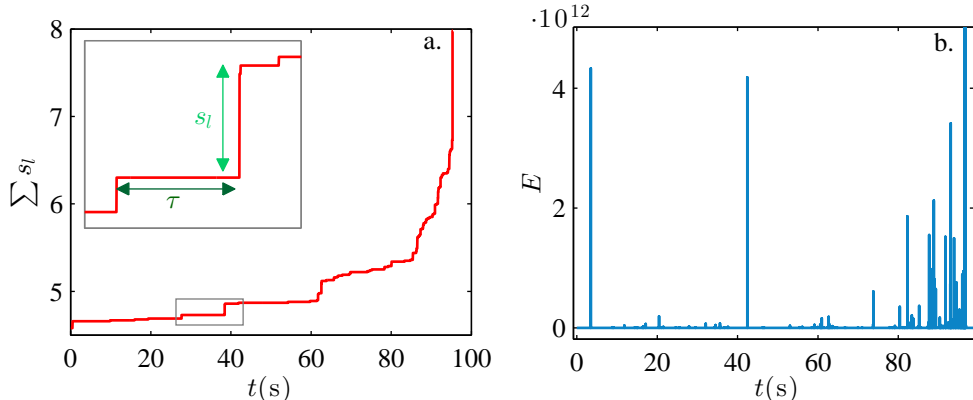


Figure 1.6: (a) Evolution of the fracture length with time. In the inset an example of waiting time τ and a fracture jump s_l are represented. (b) Energy-time diagram of the acoustic bursts during the experiment.

only with the part of the data where the typical waiting time between the events is at least as long as their duration (1 ms). In practice this corresponds to excluding the end of each experiment (up to 1 s).

3.2 A rough comparison between acoustics and visualisation

First we check if any obvious similarity can be detected between the AE and DI signals. We compare the number and occurrence times of jumps and AE events, without considering their energy value. Each of the experiment results in approximately 50 jumps and a few hundred acoustic events (figures 1.7 a and b), which is a clear indication that the AE is much more sensitive than the image analysis.

Now let us compare AE and DI signal by imposing the same frequency to each of them. By integrating the energy of the AE signal in consecutive time windows of $w = 0.1$ s, which corresponds to the temporal resolution of DI, we obtain a new time series denominated $\mathcal{E}(t_w)$ where t_w corresponds to the starting time of each window. Each nonzero value of $\mathcal{E}(t)$ constitutes an integrated event. Figure 1.7.c shows that the activity in terms of cumulative events' number is very similar for DI(t) and $\mathcal{E}(t)$. The number of AE events to number of DI events ratio is equal to 1.02, 1.13 and 1.54 for e1, e2 and e3 in figure 1.7.c respectively, and 1.07 ± 0.31 when we consider all the experiments. The dispersion of these coefficients may be associated to the variations in the contact between the transducer and the paper; however, the fact that they are of order 1 suggests that AE delivers the same information as DI, provided it is analysed at the same time scale as DI, and in particular the number of DI events become equivalent to the number of integrated AE events.

From the original acoustic signal, up to ten times more AE events can be detected than by DI. We verified that this is not only due to the lower time scale of the DI analysis. Even for a higher image acquisition rate (2000 Hz) and a better spatial resolution (10 μm per pixel), DI was unable to detect the more-elementary events that are captured by the acoustics. Figure 1.8 shows the time series of DI and AE events for one of these experiments (we intentionally represent data from the end of the experiment in order to get several DI events in a short time interval). Even in this case AE events are more numerous, and a direct link can not be established between AE and DI events.

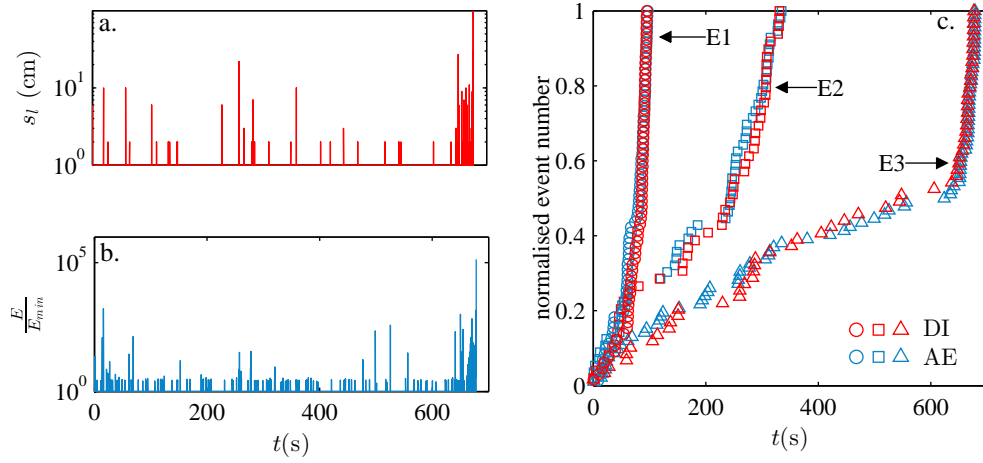


Figure 1.7: Time series of (a) s_l and (b) the energy of AE (normalised to its minimum value E_{min}) during one experiment. (c) Comparison between DI activity and AE activity integrated in 0.1 s time intervals for three experiments (e1, e2, and e3). The experiment represented in (a) and (b) corresponds to experiment 3 in (c).

The difference in the two measurements is related to the physical process they measure: acoustics is a technique that may be able to detect events down to the fibre scale, and DI requires the accumulation of enough elementary rupture events able to produce an observable damage. We can roughly say that a DI event (macroscopic opening of the fracture) is an accumulation of AE events (individual fibre fractures). This idea is corroborated by the fact that the direct temporal correlation between $s_l(t)$ and $\mathcal{E}(t)$ is very weak.

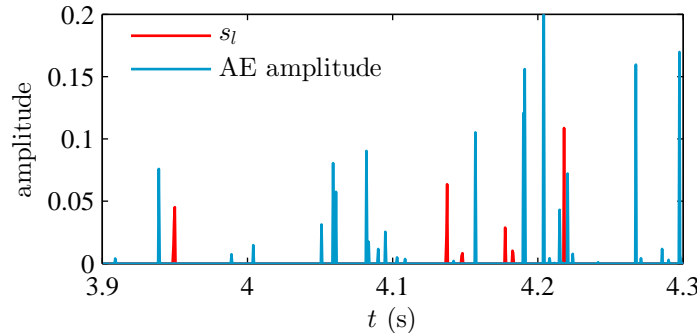


Figure 1.8: Time series of DI (red) and AE (blue) events, for an experiment with 2000 Hz image frame rate.

The fundamental difference between AE and DI events results makes it impossible to match them individually. However, our data is suitable for statistical analysis. In the following, we will study and compare the probability distributions of two different variables characterising subcritical fracture: waiting times and energies.

3.3 Probability distributions of time and energy

3.3.1 Waiting times

For subcritical fractures the time between two discrete events τ often follows power-law distributions [32, 67, 122]. Figure 1.9.a shows the probability distributions of waiting times between the events for the jumps τ_{DI} and the acoustic emission data τ_{AE} for all the experiments combined. The probability distribution for τ_{AE} was multiplied by 500 in order to make data collapse visually. The distributions were fitted as power laws and the obtained exponents are very similar: 1.06 ± 0.05 and 1.00 ± 0.03 for DI and AE waiting times respectively. Furthermore, cut-offs seem to appear for the same values of τ .

The distributions also match, without adjustment, when the acoustic signal is processed in order to get a signal with frequency (10Hz) equal to the images' frame rate (figure 1.9.b).

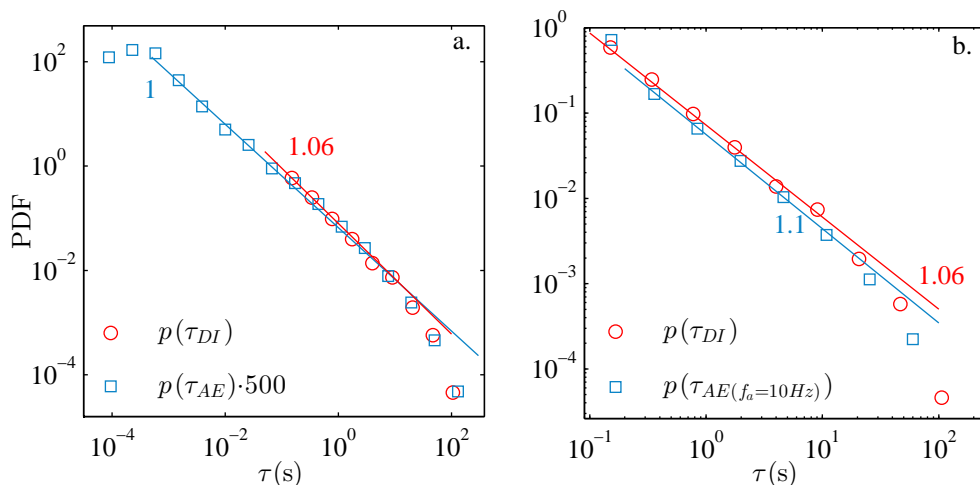


Figure 1.9: (a) Distribution of waiting times of the fracture jumps, obtained by DI (red circles) and distribution of waiting times between acoustic events multiplied by 500 (blue squares). (b) Distribution of waiting times of the fracture jumps, obtained by DI (red circles) and distribution of waiting times between acoustic events for a modified acoustic signal with a frequency 10Hz (blue squares).

The only difference between the two distributions in figure 1.9.a is in the span of values they cover. Since acoustic data acquisition has a much better time resolution, acoustic waiting times spread on a larger set of values - going as low as 10^{-4} s. The overall similitude between the two probability distributions indicates that all the acoustic bursts may correspond to fracture events.

3.3.2 Energies

Direct Imaging

In this two-dimensional system, fracture energy scales to first order as the crack's length. Therefore, the normalised distribution of jump sizes is also equal to the normalised distribution of jump energies. We defined three different lengths for the fracture jumps: s , s_s and s_l (section 2.2.1). Their probability distributions are represented in figure 1.10.a. The three distributions follow a power law over approximately one decade followed by a cutoff. By fitting the power laws we extracted

an exponent of 1.3 ± 0.2 for s_s , 1.3 ± 0.2 for s_l , and 1 ± 0.1 for s . These values are coherent between them, since the value of the exponent of the s distribution is the smallest, which can be related to the fractal structure of the fracture edge.

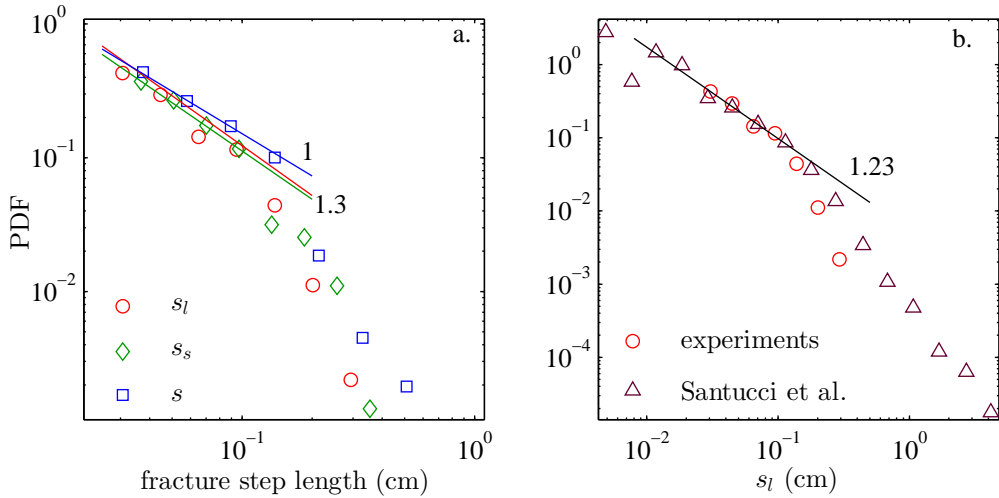
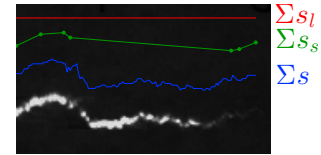


Figure 1.10: (a) Probability distribution of fracture jump length (s_l , s_s and s), as defined in section 2.2.1 (reminder of lengths definitions here on the right). (b) Probability distributions of s_l for our experiments, and experimental results from [124].



Because of the relatively small number of jumps and the limited span of the power law, we cannot rely on the results obtained about the jumps' statistics. Fortunately, we dispose from data from previous work, where subcritical fracture on the same type of paper was observed under similar conditions [124]. In this study an exponent of 1.23 has been found for the power law distribution of s_l . Figure 1.10.b shows the distributions of s_l resulting from our experiments and from the ones reported in [124]. Although our statistics is considerably poorer, it is possible to notice a good agreement between the two distributions having a common power law with a long cut-off.

Acoustic Monitoring

The estimated acoustic energy E follows a power law with an exponent $\beta = 1.51 \pm 0.06$. It spans over more than 2 decades (figure 1.11), and few hundreds of events are taken into account for the fit, which makes the estimation reliable. Contrary to what was expected, this value is significantly different from the exponent of the power law distribution of jumps.

One of the possible reasons for obtaining such a difference in the energy exponents may be the difference in the recording's resolutions: 10 Hz for the image frame rate, and 2MHz for the acoustic emission monitoring. In the following, we will discuss the influence of the frequency on the estimated exponent.

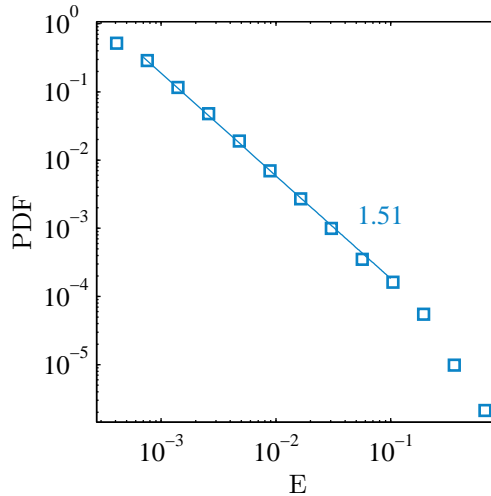


Figure 1.11: Probability distribution of the energy of the acoustic fracture events.

3.4 The influence of the acquisition frequency

In order to compare analysis of measurements at the same frequency, we will lower the frequency of the acoustic data down to 10 Hz. The time-energy signal of the experiment is separated in windows of length $w = 0.1$ s each. The energy of all acoustic events occurring in one window is summed up (this process is illustrated in figure 1.12). Hence, we obtain a new series of acoustic events, corresponding to a recording with a frequency of analysis $f_a = 10$ Hz. We will alternatively talk of frequency of analysis f_a or integration window w , since they both represent the same process, and $w = \frac{1}{f_a}$.

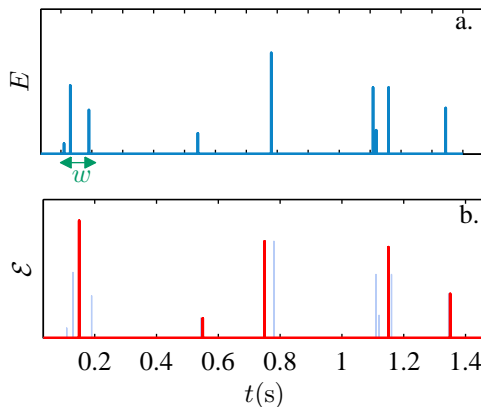


Figure 1.12: Illustration of the process of lowering the frequency of the AE signal. (a) The initial signal and the integration window w . (b) The newly obtained signal (the initial signal is in very light blue).

Figure 1.9.b shows that this analysis has no influence on the exponent of the waiting times distribution (except for reducing the span of the power law), which is expected, since times of the events were not modified.

Now, if we look at the distribution of the acoustic energy \mathcal{E} which has been obtained at $f_a = 10$ Hz, we find a power law over about three decades with an exponent $\beta = 1.35 \pm 0.04$, closer to the one found for the distributions of jump sizes (figure 1.13.a). This similarity between the distributions of energy for DI and AE has also

been verified at larger time windows (0.2 s, 0.5 s and 1 s). In these cases both signals were integrated over the time window.

For the AE data we can do the same analysis for shorter time windows. The resulting exponent β for $0.05 \text{ ms} < w < 1 \text{ s}$ is shown on figure 1.13.b (dark violet circles). We find that β varies continuously from its initial value - 1.51 - to a value around 1.3, with an abrupt change around a time scale of 1 ms. Though the difference between the initial and final exponents - 1.51 and 1.34 - might seem small, it is important. Firstly, it is larger than the incertitudes on these values, so it is not a statistical artefact. Secondly, a small change in this exponent can induce significant changes in the probability distribution of the event's energy, and particularly in the number of large events that are expected (see discussion in section 3.1 in the Introduction).

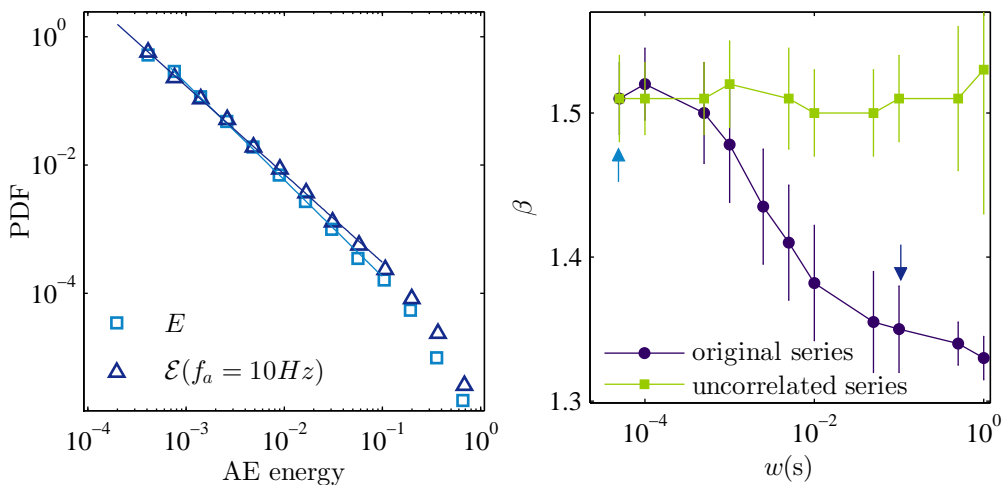


Figure 1.13: (a) Probability distribution of the acoustic energy E for the original AE data, and the acoustic energy \mathcal{E} for data integrated over windows of $w = 0.1 \text{ s}$. (b) The effect of increasing the integration window w on the value of the energy exponent β , for the original experimental time-energy series, and for series with uncorrelated (mixed-up) energies. The two arrows point at the exponent values of the probability distributions in a.

The strong dependence of β on w , with a decrease for small¹ w may result from temporal correlations, linking small waiting times with high energy events. To begin with, we verify this by generating a new signal where correlations can not exist: we assign random magnitudes from the experimental data to random event times from the same data, in order to "break" the correlation existing in the signal. In this case, integrating the energy signal over finite times does not change the energy distribution (light green squares in figure 1.13.b). This confirms that temporal correlations are responsible for the change in the exponent obtained when analysing the experimental AE signals at different time scales.

The autocorrelation of the AE signal also shows the existence of temporal correlations at the same time scale ($\sim 1 \text{ ms}$)². The signal that we work with being very long

¹ w needs to be larger than 1 ms for the effect to be observed, but this duration is small compared to the lifetime of the sample. It corresponds to the lower limit of the power law distribution of waiting times (figure 1.9.a) in figure compared to the sample's lifetime

²Studying the length of the events and the dead-time between them, as well as the waveform of events that occur closely one after another, we verified that this correlation is not an artefact linked to the duration of the events.

and mostly padded with zeros (because of the long inactivity times), the correlation is very weak (figure 1.14), but still stands out. In the next section we show that this correlation comes from aftershocks following the important fracture events.

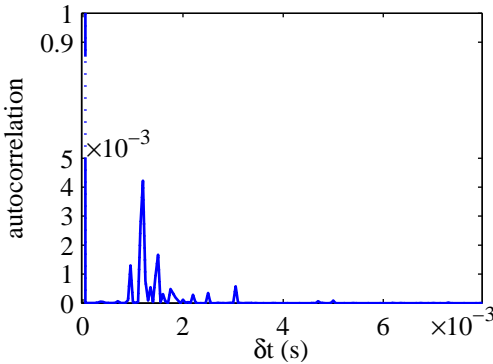


Figure 1.14: Autocorrelation of the signal of all the experiments.

3.5 Aftershocks

In order to determine what the time correlation is due to, we study waiting times and energies of the events of all the experiments combined. In figures 1.15 a-c, each event is represented by a point on an energy-waiting time diagram. Each event is defined by its energy and can be represented with (a) the waiting time that precedes it, (b) the waiting time that follows it or (c) an uncorrelated waiting time. We can already see in (b) that large energies (top) are preferentially followed by small waiting times (left). To compare this to a situation where waiting times and energies are uncorrelated, we construct an artificial time series in which we destroy correlations by keeping the same AE event arrival times, but redistributing randomly the values of the AE event's energies, as was done above (c). The three diagrams are divided in 14×9 cells, and the number of events in each cell is stored in 14×9 matrices: B for waiting times before the events, A for waiting times after the events, and D for the uncorrelated waiting times. For more accuracy we generated 1000 artificially uncorrelated series and calculated D as their mean density of events (figure 1.15.f). Finally, a comparison between the experimental results (A and B) and the uncorrelated case (D) is made by calculating the relative difference between the matrices. The result is shown in figures 1.15(d) and (e). We find that the number of events having large energy and followed by small waiting times (aftershocks) is significantly larger for the experimental data than for the uncorrelated case (top arrow in figure 1.15.e). On the other hand, this behaviour is not observed for waiting times preceding the events (figure 1.15.d). This shows the existence of aftershocks during the propagation of the crack, with typical waiting time of 10^{-3} s, and no foreshocks. Also, for both waiting times (before and after the event) we observe a large density for small energies (arrows at bottom right of (d) and (e)), meaning that there exist "inactivity times" characterised by long waiting times and low energy events.

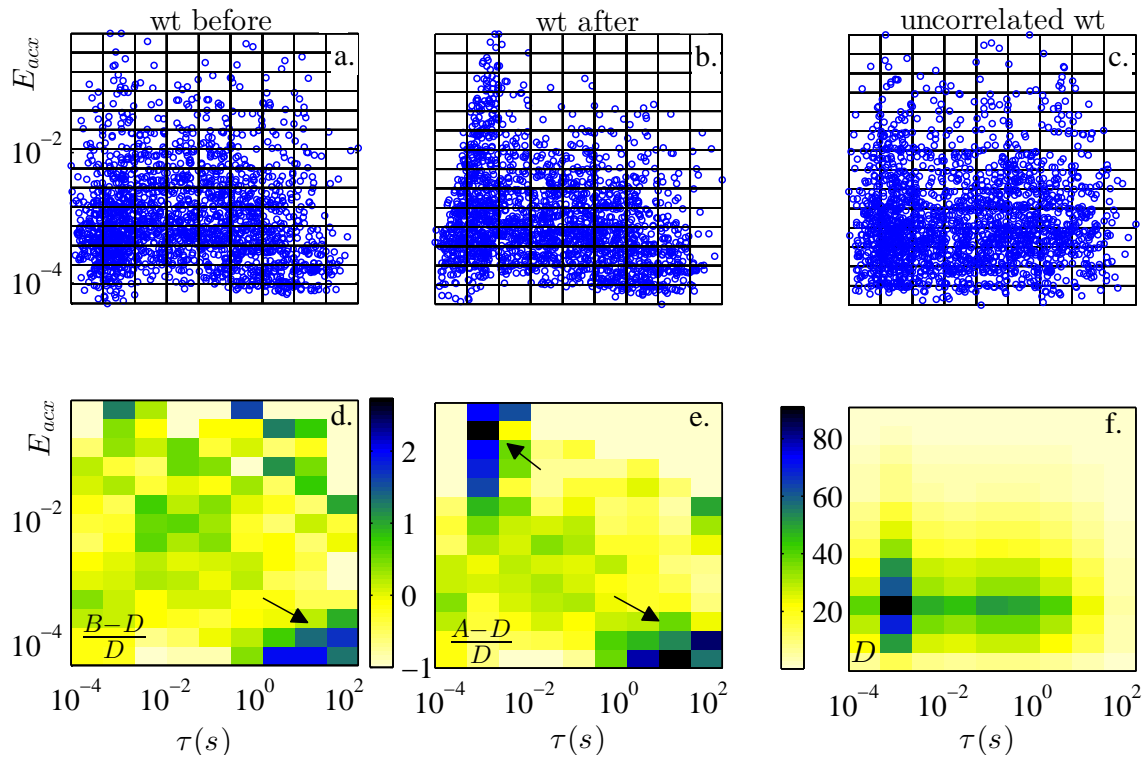


Figure 1.15: (a) Repartition of events’ energies and waiting times before events. (b) Repartition of events’ energies and waiting times after events. (c) Repartition of events’ energies and mixed-up waiting times. (d) Relative difference between the number of events in each interval for waiting times before the event and decorrelated waiting times. (e) Relative difference between the number of events in each interval for waiting times after the event and decorrelated waiting times. (f) Mean number of events in each interval for 1000 uncorrelated event series.

4 Conclusion

We studied the subcritical crack growth of a single crack in a sheet of paper submitted to a constant force. By combining DI and AE measurements we showed that the two methods operate at different scales both spatially and temporally: acoustics captures fast rupture events at the scale of the fibres, while the accumulation of these events provokes a damage zone that will eventually be detected by the image analysis. Hence, the two signals present poor correlation, and events resulting from DI and AE can not be matched individually. In spite of these differences, DI and AE result in similar distributions of waiting times and of events’ energies, provided AE is analysed at large time scales, corresponding to the images acquisition rate.

We observed a dependence of the exponent of the probability distribution of AE energies with the time scale at which measurements are done. The dependence results from temporal correlations, i.e. aftershocks in the acoustic signal. This observation indicates that when a system containing temporal correlations is studied, the frequency of the measurements must be high enough to resolve each event. Otherwise, the probability distribution of the events’ energies can not be precisely determined. In our case we were not able to resolve aftershocks by DI, resulting in a misleading, lower exponent for the probability distribution of the energies [139].

5 Perspectives

Increasing the images' frame rate

We already conducted few experiments at higher frame rate (2000 Hz). As we already discussed, we did not identify any direct link between individual fracture jumps and acoustic bursts. We used digital image correlation (DIC) in order to analyse the deformation of the sample. The sample deforms continuously and we did not identify any sudden changes which could be related to the AE signal.

Nevertheless, using DIC we observed paper oscillations occurring after large acoustic events. Figure 1.16.a shows the temporal evolution of the vertical position of one point near the crack tip as determined by DIC. There are permanent oscillations: these are due to oscillations of the experimental set-up, as well as of the camera. After the great acoustic event (figure 1.16.b) the amplitude and frequency of the oscillations seem to change.

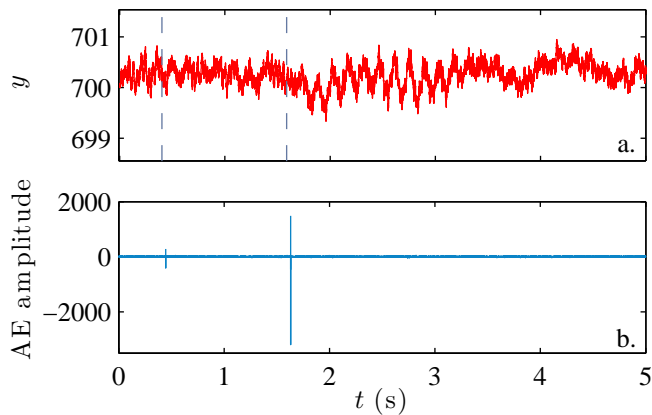


Figure 1.16: (a) Vertical position of one point near crack tip, determined by digital image correlation. The vertical lines represent the time of the two acoustic events on figure b. Note how oscillations change their frequency and amplitude after the greater acoustic burst. (b) Acoustic signal corresponding to the same time span as results in a.

These oscillations were almost systematically observed after strong acoustic events, and might be associated to a mechanical wave passing through the sheet. For the time being they are difficult to characterise because of the coupling with background oscillations, but the study could be continued by eliminating the background oscillation. The wave propagation can be important for energy balance calculations. Also, one could investigate the possibility of two cracks interacting through the generated waves, similarly to the dynamic earthquake triggering (section 2.5.2 in chapter 3).

Fracture of a single fibre

We studied paper fracture from a statistical point of view, considering the sheet of paper as a whole. Some questions can not be answered with this kind of approach. In particular, we still do not know if the power-law distribution of the energies is due to the dispersion of fibres sizes, to avalanches of fibre fractures, or both. We do not have any details about the scenario of a single fibre fracture: does it break instantaneously or by slow damage accumulation, or how important is the presence of other fibres? Also, until now we only had a relative estimation of the acoustic energy. Using single fibre fracture one could determine the acoustic energy

associated to a single fibre fracture and compare it to values from experiments on global paper fracture.

In order to answer these questions, the idea of doing experiments on single fibre fracture is being considered. Observing and manipulating single fibres would be done using a micro tensile tester set inside a Scanning Electron Microscope (SEM). Simultaneous observation of the force-deformation relation, acoustic emissions and visual aspect of the bundle will provide valuable information about how single paper fibres break.

Application on other correlated systems

We saw that decreasing the frequency of the time signal of fracture had some influence on the exponent of the energy distribution. The same analysis can be applied to other phenomena exhibiting time correlations. In chapter 4 we will look at earthquake aftershock sequences as an example of correlated system and study the influence of the time resolution on the energy distribution.

CHAPTER 2.

FRACTURE OF A FIBRE BUNDLE: EXPERIMENTS AND MODEL

1	Introduction	32
2	Model on thermally activated rupture in fibre bundles	33
2.1	The democratic fibre bundle model with thermal noise	
	Previous results on creep simulations	33
2.2	Simulations at constant strain	34
3	Experiments on bundle fracture	39
3.1	Stress corrosion of glass	39
3.2	Experimental procedure	40
3.3	Analysing the acoustic events	42
3.4	Some basic considerations on mechanics	43
3.5	Strength distribution of fibres	43
3.6	Experimental results	44
4	Comparing experiments and simulations	49
5	Conclusion and perspectives	49

The experiments presented in this chapter were done in collaboration with Mohamed R'Mili and Nathalie Godin in the CERA Group at MATEIS, Lyon

1 Introduction

In the previous chapter we studied the fracture of a sheet of paper, which is actually a fracture of a complex network of fibres with different sizes. The fibrous structure of the paper and the disorder which it creates are crucial for observing a discrete fracture propagation. What happens if all interactions and contacts between fibres are removed? Imagine one could separate all the fibres from a sheet of paper, straighten them up, remove friction, but still keep them together. The result is a bundle of fibres with various diameters - hence various strengths. The bundle can be submitted to a load, just like the paper sheet in the previous chapter. This defines a fibre bundle model (FBM).

Fibre bundles are a classical, widely used system for studying delayed fracture. In its original version [25] the FBM consists of parallel fibres fixed at both ends to rigid supports and loaded in tension. In the democratic version of this model all unbroken fibres share the load equally. Fibres are elastic, with the same stiffness for all of them, and brittle, with a random distribution of failure strength. This model is completely deterministic and many of its properties can be solved analytically. Different features have been added to the FBM since: loading share rules [154], coupling to an elastic block [30], thermal fluctuations [20, 106], damage accumulation (resulting in plasticity) [66] and viscoelasticity [59] (for a review see [109]), hence fibre bundle models can have behaviours representative of many different processes. The simplicity of the model and the complexity of the features that it allows to observe, make the fibre bundle model a very efficient way of studying fracture of heterogeneous materials.

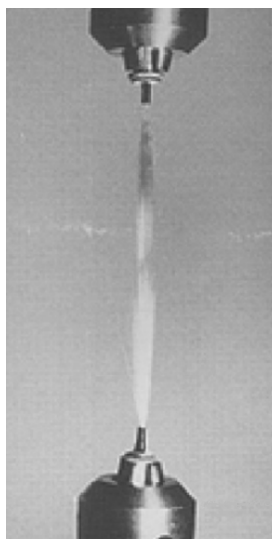


Figure 2.1: Lubricated E-glass bundle after fracture. From [117].

Experimental studies on fibre bundle fracture are more complicated to carry out, and thus less common than simulations. They particularly took off since the development of fibre reinforced composites. In fibre reinforced composites, small fibres of one material (glass, aluminium, steel, graphite, etc.) are trapped into a matrix made of some other material, in order to improve some of its properties (stiffness, strength, weight, cost, etc.)[1]. Because they are widely used in industrial processes and civil engineering, characterising the fibres' properties has become important. Testing a bundle of fibres, rather than fibres one by one is a more efficient way of gathering this information. Hence, a large part of the experiments on fibre bundle fracture were designed in order to determine the strength distribution of fibres [23, 35, 45, 155].

In this chapter we will compare results from simulations and experiments on fibre bundle fracture. Simulations are done using a FBM with thermally activated noise in a disordered fibre. Experiments use bundles of E-glass fibres immersed in water. Both studies are at their beginning, and though results are not exhaustive, they show some important aspects of bundle fracture and establish the basis and protocols for possible future work on the subject. In particular we concentrated on the slowing

fracture dynamics of a bundle under constant strain, the Omori law it follows, and the variations of its exponent.

2 Model on thermally activated rupture in fibre bundles

We will present some results obtained by using a democratic fibre bundle model with thermal noise, in conditions of constant strain. This study is very short, but considering simulations before the experiments allows to understand some of the observations on fibre bundle experiments (which are presented later in this chapter). Previous work on this model within our team already provided results from analytical calculations and simulations [79]. We continued this work, firstly by comparing analytical calculations to the simulation results and then by studying the dynamics of the fracture. This model results in an approximate power-law distribution for the number of broken fibres in time, similar to the Omori law for earthquakes. We will study the variations of the exponent of the Omori law p with the different parameters of the model.

2.1 The democratic fibre bundle model with thermal noise Previous results on creep simulations

We are interested in a fibre bundle model with equal load sharing among fibres (hence a democratic one). The two main elements of the model are disorder and thermal fluctuations. The disorder is implemented by defining fibres with different failure thresholds: they are normally distributed, with a mean $\sigma_c = 1$ and a variance T_d . Hence, T_d is a quantity that reflects the dispersion of fibre strengths, and will be called the *disorder temperature*. The influence of the thermodynamic temperature T is modelled as a random, normally distributed additional contribution to the stress applied to each fibre, which will be denoted $\eta(t)$. $\eta(t)$ is determined at each time step and follows a zero - mean value normal distribution with a variance T , where T is the adimensioned thermodynamic temperature ¹. Thus, each fibre has a rupture threshold which is constant in time, and the force which is applied to it experiences slight fluctuations due to thermal noise. The basic idea of the model is schematically represented in figure 2.2. Models with the same ingredients have already been well studied for a constant load applied to the bundle [20, 106]. In this case (i.e. a creep experiment) the dynamics of the fracture follows three different stages. After the application of the force the strain rate decreases rapidly, which constitutes the primary creep stage. The secondary creep stage is a steady state where strain is constant. Its duration is very variable, and the number of broken fibres per unit time follows an approximate Omori law [118]. As fibres break, the constant force applied to the bundle is redistributed to the remaining fibres, hence the force per fibre increases constantly, until it is so high that strain increases rapidly until the rupture of the whole sample.

The presence of disorder changes the behaviour of the system. The failure time of

¹For commodity, in the model we only use adimensioned quantities.

$T = \frac{k_B \bar{T}}{YV}$, where Y is the elastic modulus, k_B the Boltzmann constant, \bar{T} the absolute temperature, and V the fracture nucleation volume.

$\sigma_c = 1$, hence all the stress-related quantities (σ_0 , σ_s , T_d) are normalised by $\bar{\sigma}_c$, the value of the mean strength of fibres

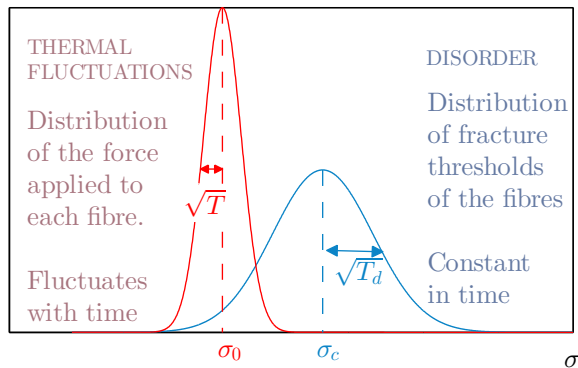


Figure 2.2: Schematic representation of the strength and force consideration of the fibre bundle model we work with.

the bundle is usually shorter for disordered fibres [20, 106] and the influence of the disorder temperature was described as a lowering of the fracture energy barrier. Also, adding disorder makes the exponent of the Omori law during the secondary creep stage p decrease [118]. This is in agreement with the idea of disorder accelerating the fracture dynamics, since a lower p means that the number of broken fibres decreases more slowly.

2.2 Simulations at constant strain

The simulations we performed are based on the same principles as the previous model. The only difference is that we study bundles of fibres submitted to a constant strain ϵ [79]. Supposing the fibres are elastic with a Young modulus Y , the applied stress $\sigma = Y\epsilon$, is constant in time also. This implies some important differences with respect to the creep simulations. Since the force per fibre does not change, and supposing (very reasonably) that fibres break from weakest to strongest, the energy barrier for the fracture of each fibre increases as fracture advances. Thus, the number of broken fibres per unit time inevitably decreases with time. In this case, high disorder implies some very weak - but also some very strong fibres, and without a force increase (and depending on the parameters) the rupture time of the last ones can diverge.

In this section we review the assumptions and the main steps of the **analytical calculation** of the number of broken fibres calculation (for details see [79]), which leads to an Omori law (equation 2.4). Considering the thermal fluctuation of the applied stress, and for a slow enough process ($\sqrt{T} \ll \sigma_s - \sigma_0$), the mean fracture time (i.e. the inverse of the probability for $\sigma_0 + \eta(t) > \sigma_s$) of a fibre with a failure threshold σ_s is:

$$\tau(\sigma_s) = \sqrt{\frac{2\pi}{T}(\sigma_s - \sigma_0)} e^{\frac{(\sigma_s - \sigma_0)^2}{2T}}. \quad (2.1)$$

Supposing that the fracture of each fibre occurs exactly at its mean fracture time, and knowing the distribution of failure thresholds σ_s is a Gaussian, one finds the following equation for n , the number of broken fibres in the bundle:

$$\frac{dn}{dt} = \frac{N}{t} \sqrt{\frac{T}{T_d}} \frac{1}{2\sqrt{\pi \ln(t)}} \exp \left[-\frac{(\sigma_0 + \sqrt{2T \ln(t)} - \sigma_c)^2}{2T_d} \right] \quad (2.2)$$

and so

$$\ln \frac{dn}{dt} = - \left(1 + \frac{T}{T_d} \right) \ln(t) - \frac{1}{2} \ln(\pi \ln(t)) + (\sigma_c - \sigma_0) \frac{\sqrt{2T}}{2T_d} \sqrt{\ln(t)} + K. \quad (2.3)$$

When t is large enough, the contribution of the term proportional to $\ln(\pi \ln(t))$ is negligible, and we can consider that the rupture rate follows an *approximate* power law, with an exponent:

$$p \simeq 1 + \frac{T}{T_d} - c(\sigma_c - \sigma_0) \frac{\sqrt{2T}}{2T_d}, \quad (2.4)$$

where the constant c should be approximately equal to $\frac{\sqrt{\ln(t)}}{\ln(t)}$, and thus depends on the time range we choose for fitting.

Simulations on this model were done by considering bundles of 2000 fibres and $5 \cdot 10^6$ time steps. The simulation procedure is quite straightforward. Once all the parameters are fixed, one generates the distribution of fibre thresholds. Then, at each time-step a new value of $\eta(t)$ (the thermal noise contribution to the applied force) is generated for each fibre. If the force applied on a fibre ($\sigma_0 + \eta(t)$) is greater than its failure threshold, the fibre is considered broken. The number of broken fibres will be denoted $n(t)$.

2.2.1 Results

For both simulations and analytical calculations dn/dt follows an approximate power law with t , at long times. The agreement between the results from the two methods (calculations and simulations) depends on the system's parameters, and is better for large (figure 2.3.b) than small (figure 2.3.a) temperatures. Nevertheless, even when the exact value of dn/dt does not match the simulations, both methods show the same tendency of $dn/dt = f(t)$: a power law for long times, eventually saturating for short times.

Influence of the temperature and the disorder on the Omori law exponent

The power law for dn/dt at long times is an approached one, so the value of p is sensitive to the time interval that we fit on. We chose to fit on the last two decades of simulation time, i.e. on the interval $[5 \cdot 10^4, 5 \cdot 10^6]$ ².

Results from analytical calculations and simulations are represented on figure 2.4: the value of p is represented as a function of T , the thermodynamic temperature, for different values of T_d , the disorder temperature. The dashed black lines on figure 2.4 represent the calculation of p according to equation 2.4 and the color curves correspond to values of p obtained for simulations. In the interval $[5 \cdot 10^4, 5 \cdot 10^6]$ the value of c varies from 0.25 to 0.3. Since the approximation of a constant value of c is not quite accurate, we chose to fit c as a free parameter rather than fix it, and found $c=0.29\pm0.01$. Since a number of approximations were made in the analytical calculations the curves do not match perfectly, especially for low T and low T_d .

²For high stress and temperature the whole bundle breaks at times shorter than $5 \cdot 10^6$, so we calculated the power law at the end of the bundle's lifetime.

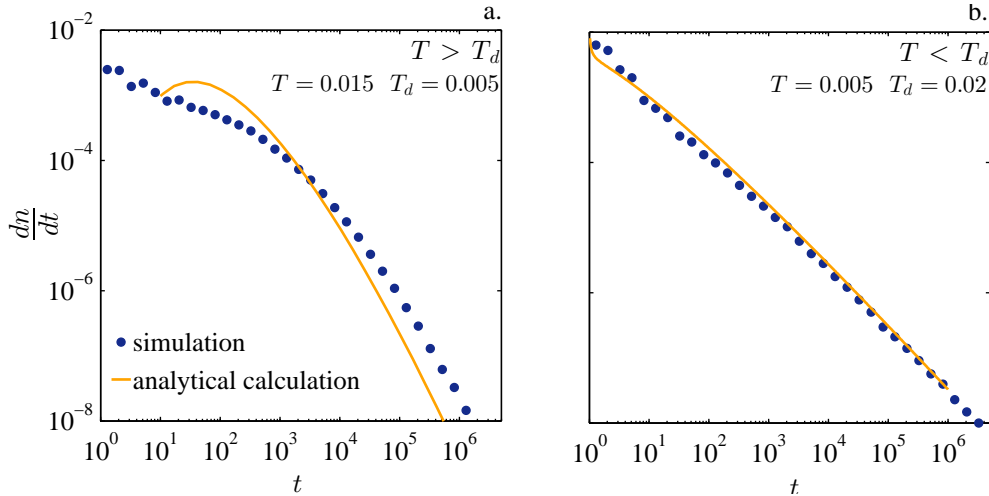


Figure 2.3: Decrease of dn/dt with t for simulated bundles (blue circles) and analytical calculation, according to equation 2.2 (yellow line).

(a) $\sigma_0 = 0.55$, $T = 0.015$, $T_d = 0.005$.

(b) $\sigma_0 = 0.55$, $T = 0.005$, $T_d = 0.02$.

Despite the differences, simulations and analytical calculations show the same tendency for the variation of p , the exponent of the Omori law, with the temperature T and the disorder temperature T_d . p systematically increases with T , regardless of the disorder. It increases with increasing T_d for low T , and decreases with increasing T_d for high T . For simulations, the crossover between the two regimes can be identified as the point where all curves representing $p = f(T)_{T_d}$ meet: $T \sim 9.3 \cdot 10^{-3}$. For the analytical calculation this corresponds to the temperature which makes the second and the third term of equation 2.4 cancel each-other, hence $T_{cross} = \frac{c^2(\sigma_c - \sigma_0)^2}{\sqrt{2}} = 1.2 \cdot 10^{-2}$, for $\sigma_0 = 0.55$.

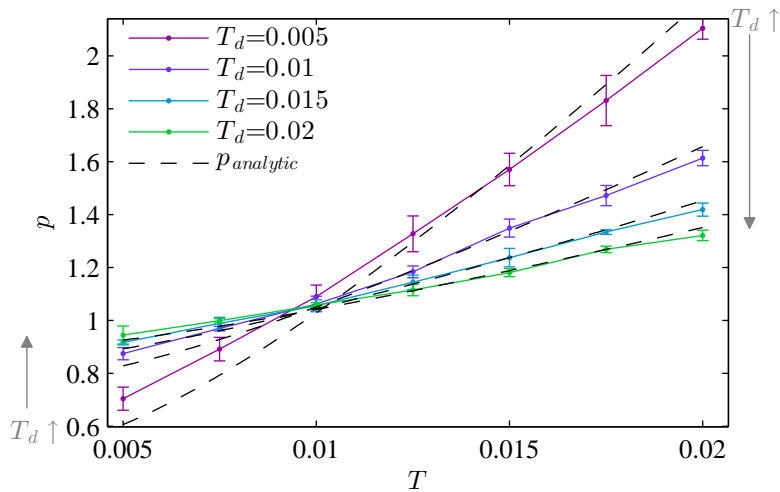


Figure 2.4: The Omori law exponent p as a function of T at constant T_d , for different values of T_d , and at $\sigma_0 = 0.55$. Dashed black lines: calculation of p according to equation 2.4 ($c = 0.29$). Colour curves: values of p obtained by simulations.

Total number of broken fibres

Now let us concentrate on the total number of broken fibres in a simulation. Figure 2.5 shows the fraction of broken fibres n/N_0 within $5 \cdot 10^6$ iterations as a function of the disorder temperature T_d , for different values of the thermodynamic temperature T . n/N_0 increases with the disorder for low temperatures, and decreases with the disorder for high temperatures. The change occurs for $T_{cross} \sim 0.75$, which is lower, but close to the values found previously. For this temperature $n/N_0 \sim 0.5$. Hence, the two regimes actually correspond to the two parts of the fibre strength distribution: one concerns the weak fibres (the half of the fibres with higher strengths), and the other one the strong ones (the half of the fibres with lower strengths).

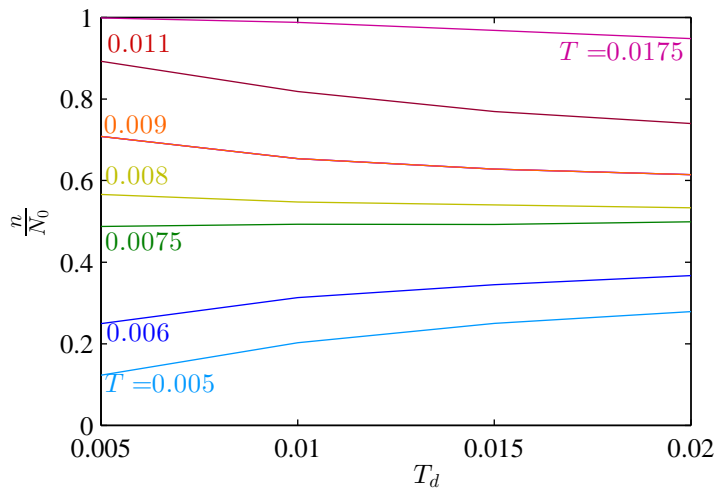


Figure 2.5: Fraction of broken fibres within $5 \cdot 10^6$ simulation steps as a function of T_d , for different values of T . $\sigma_0 = 0.55$

The importance of the strength distribution

The observations we just made on the dynamics of the fracture and the total number of broken fibres can be explained considering solely the fibre strength distribution. Indeed, in the case of constant strain, there is no force transfer on the fibres, no accelerating dynamics, and the fracture dynamics is governed by the fibre's strengths.

In the case of low temperature (figure 2.6, on the top), the power-laws exponent is extracted from the fracture dynamics of weak fibres. In this case, increasing the disorder means that the number ratio of strong to weak fibres decreases. Thus, the number of strong fibres, which are broken toward the end of the simulation, decreases (compared to the case of low disorder), and the fracture dynamics slows down more rapidly. This explains the increase of the Omori law exponent when T_d increases. Increasing the disorder also means that the average strength of weak fibres drops, hence more of them will be broken, and n/N_0 increases.

For high temperature, the case is exactly the opposite (figure 2.6, on the bottom). Increasing the disorder would increase the ratio of strong to weak fibres, so p decreases. Also, it increases (on average) the strength of strong fibres, hence n/N_0 decreases.

Hence there is a fundamental difference in the role of the disorder in constant force and constant strain fibre bundle models. For constant force, and due to the acceler-

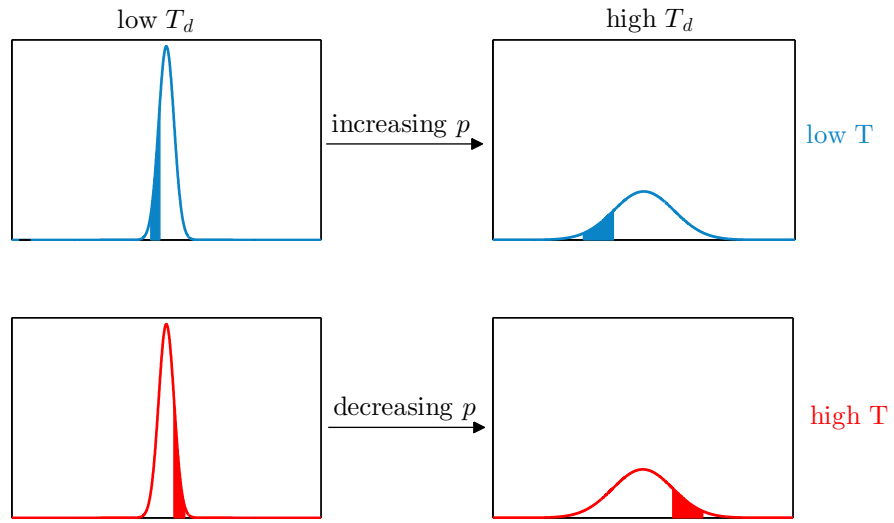


Figure 2.6: Schematic representation of the part of the strength distribution implicated in the end of the fracture simulation for different values of T and T_d .

ating nature of the fracture, increasing the disorder accelerates the fracture dynamic (the total failure time gets shorter, and p gets lower). For constant strain, increasing the disorder can accelerate or decelerate the dynamics, depending on the applied temperature and stress, a behaviour which is related to the distribution of fibres' strengths.

Influence of the applied stress on the Omori law exponent

For consistency with the experimental results, we will also discuss the influence of the applied force per fibre σ_0 . We set in a configuration closer to the experiments by choosing a highly disordered system ($T_d = 0.1$). For simulations p increases systematically with σ_0 (figure 2.7) which is in accordance with the expression of p obtained by analytical calculation (equation 2.4).

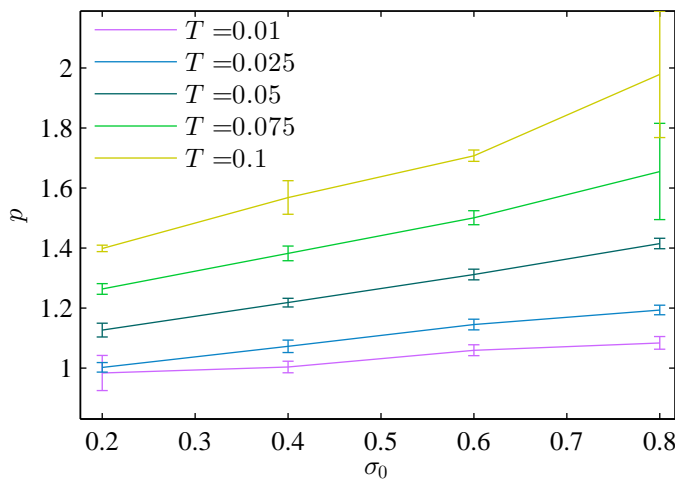


Figure 2.7: The Omori law exponent p as a function of the applied stress σ_0 for different temperatures, and for $T_d = 0.1$. Here simulations are 10^5 time steps long.

3 Experiments on bundle fracture

We conducted experiments whose protocol is quite similar to the simulations on fibre bundles. We studied the fracture of bundles of about 2000 fibres each, under constant deformation. The fibres are made of E-glass³, and have a mean diameter of 14 μm . The bundle was completely immersed in water, because of the high sensitivity of strained glass to water presence (section 3.1). This is a simple way of controlling "humidity" and it will accelerate the fracture process, so more data will be available for analysis. The fracture is monitored using either acoustic emissions (AE) or force measurements.

3.1 Stress corrosion of glass

Glass is particularly sensitive to the presence of water when stressed. By studying the fracture of different types of materials in the late 60's and the 70's, Wiederhorn [149, 150] showed that increasing humidity or temperature accelerates the propagation of a fracture in a glass sample loaded in tension. This behaviour is due to stress corrosion: a fracture mechanism occurring due to a chemical reaction, favoured when a sample is stressed. We will not be interested in the details of this process, nevertheless it is supposed to influence the experiments on glass fibres fracture. Thus, here we provide a very brief summary of the principles of stress corrosion.

In the case of stressed glass, the Si-O bond experiences strain, [84, 85] which increases its probability for interacting with other molecules. Hence, it can react with water molecules from vapour present in the air (figure 2.8). The reaction is stress enhanced and thermally activated, so the fracture velocity depends on stress, temperature and humidity.

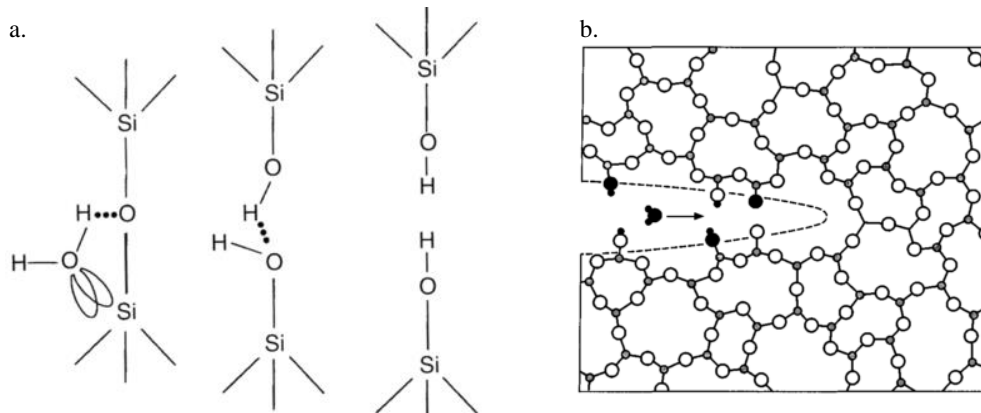


Figure 2.8: (a) The mechanism of glass hydrolysis under strain. (b) Representation of glass stress corrosion on molecular level. From [84].

Experimental observations showed that the velocity of the crack propagation v it is a strongly increasing function of the stress intensity factor K . The relationship between v and K has been described as a high-exponent power law [83] or an exponential [150]. Due to the multiple parameters involved in the process, a universal law for this relation is still lacking, and the work on this subject still continues [68, 108].

³this is the most popular type of fibres used for fibre reinforced composites, composed of SiO₂ (54%) mixed with Al₂O₃ (14%), CaO+MgO (22%), B₂O₃ (10%) and Na₂O+K₂O (< 2%)

Knowing that fracture of glass fibres is a consequence of glass corrosion, we do not expect for glass fibres to break instantaneously due to thermal fluctuations, as suggested in the previous fibre bundle model. Nevertheless, some creep experiments and simulations show that the time to failure of a sample varies as a decreasing exponential with the applied stress, similarly to the result from equation 2.1 [145, 150]. Hence, while the model studied previously (section 2) does not correspond to the microscopic fracture mechanism of glass fibre bundles, it still could reproduce some features of the experiment that we will now present.

3.2 Experimental procedure

This section provides a very brief description of the procedure used for the experiments; details are available in appendix B. The bundle preparation method and most of the experimental procedure were already well developed before the beginning of this thesis, and the same methods are applied to previously published work [116, 117].

We use a commercial bobbin of E-glass to prepare the bundles. Each bundle contains approximately 2000 parallel fibres, and its active part has a length $l_0 = 6.5$ cm. The bundles are connected at both sides to metallic parts (figure 2.9.c) which allow for the acoustic sensor to be fixed, and for the bundle to be held by chucks. Before mounting on the testing machine the sample is equipped with half a plastic bottle (necessary for immersion) and a micro 80 acoustic sensor (figure 2.9.a). Then the sample is set on an *Instron 1995* testing machine (figure 2.9.b).

Most of the experiments were done at room temperature ($\sim 23^\circ\text{C}$), and a few at controlled temperature ($\sim 45^\circ\text{C}$ or $\sim 1^\circ\text{C}$). For experiments at high and low temperature we use the liquid of a thermostatic bath for exchanging heat with the water in the bottle.

The force is monitored using two force sensors independent from each-other. The acoustic signal is recorded using *PCI2*, a data acquisition system which allows for immediate detection of acoustic bursts. The characteristics of each burst (occurrence time, amplitude, duration, energy, peak frequency) and waveforms (i.e. continuous acoustic signal during the burst) are recorded.

At the beginning of the experiment the bundle is loaded at a continuous strain rate (0.5 mm min^{-1}), until a previously fixed force value is reached. Then a constant deformation is maintained.

A total of about 30 experiments were done. Some of them were used for calibration of the bundles properties and acoustic analysis only (see section 3.3). About half of the constant strain experiments could not be used because of sudden detection problems, bundle slipping from the chucks, a bundle twisted during its mounting on the machine or water leakage. Some of these problems were detected only during the data analysis (section 3.6.1). The results from the remaining 12 experiments are discussed in this chapter.

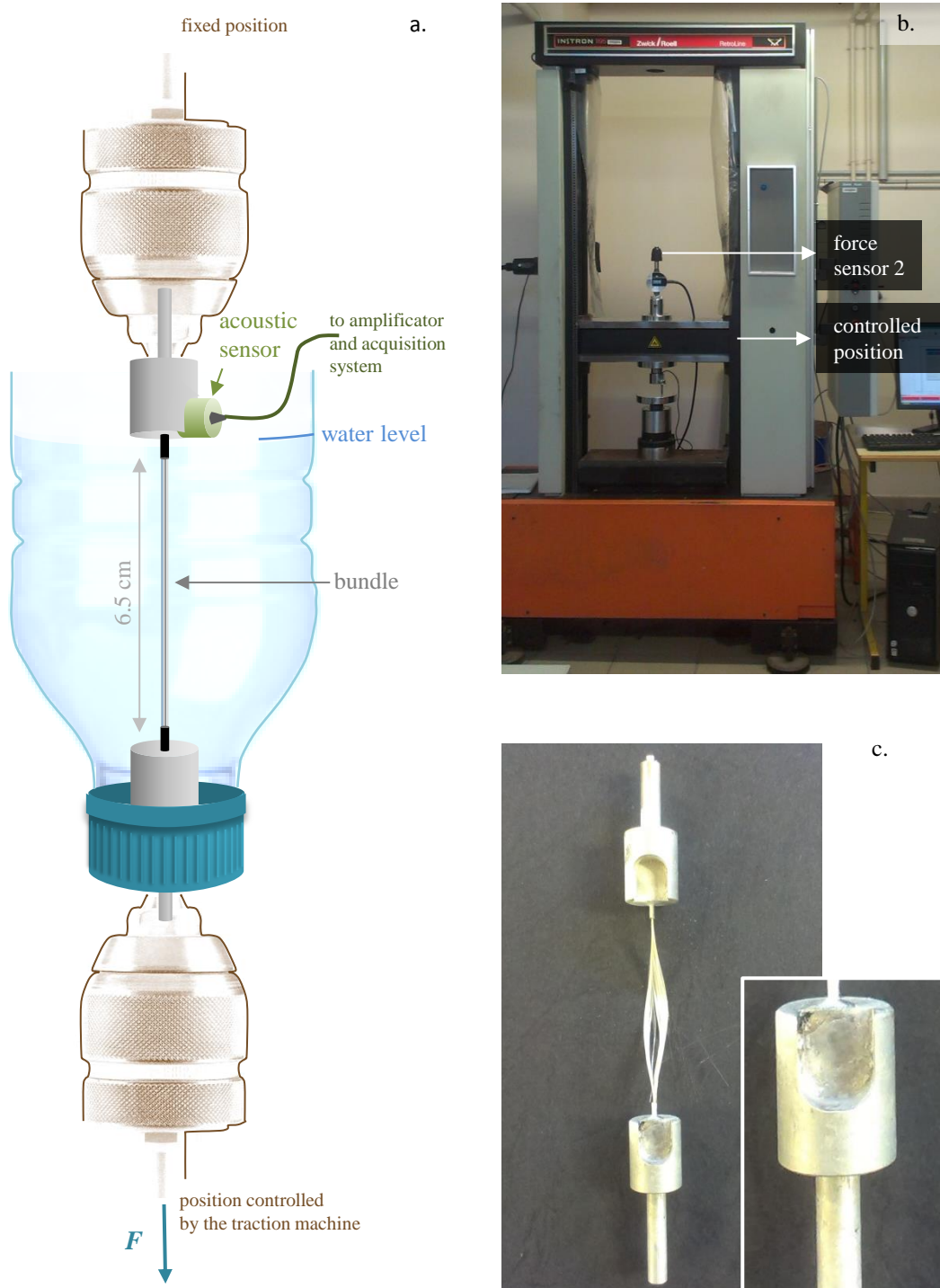


Figure 2.9: (a) Schematic representation of the experimental set-up. (b) Photograph of the traction machine (Instron 1195) used for the experiments. c. Photograph of a prepared bundle.

3.3 Analysing the acoustic events

Previous experiments on fracture of E-glass fibre bundles in the CERA group at MATEIS were done using two acoustic sensors. Events were localised, and all acoustic bursts occurring in the active zone of the bundle were considered as fracture events. Since our study concerns immersed bundles we could only use one sensor, on the top metallic part of the bundle, so a new method needed to be defined for discriminating between acoustic events related to fracture and noise.

We did a series of non-immersed experiments and we studied the acoustic bursts properties. The spectral distribution of energy appeared as a good discrimination criteria. Figure 2.10 shows the mean normalised power spectrum of (a) all events localised within the bundle and (b) all events which could not be localised, or were localised outside the bundle, during a creep experiment on a bundle. The two types of events do not have the same power spectra. The energy of the fracture events is mostly concentrated on higher frequencies ($f > 100$ kHz), than the energy of noise recordings ($f < 100$ kHz).

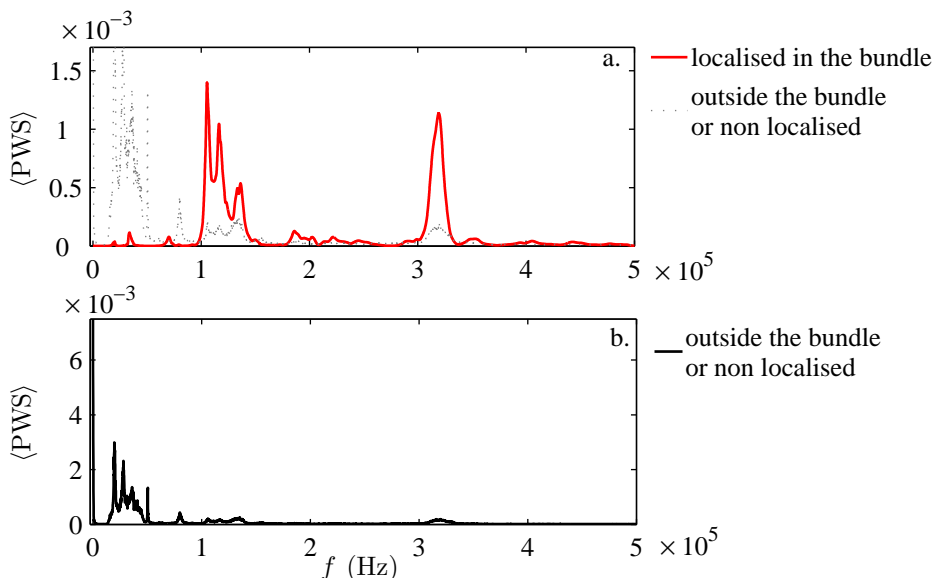


Figure 2.10: Mean power spectrum of all the events determined as (a) fracture events or (b) noise, using the localisation of the events for the discriminating criteria. The power spectrum of the noise is also represented on (a) with dashed lines.

We defined as fracture each event whose power spectrum is dominated by high frequencies (100 to 350 kHz). Figure 2.11 shows that this criteria is equivalent to the localisation criteria: events which were localised in the bundle were also detected as fracture by the power spectrum method in most of the cases. Very few exceptions exist (examples are marked by arrows in the figure). Tests on other bundles showed similar results, confirming that the analysis of the power spectrum is as efficient in discriminating fracture events from noise as is the localisation method.

The power spectrum of the fracture events differs between experiments, especially if we change the acoustic sensor. Unfortunately, we were not able to use the same sensor for every experiment. Nevertheless, it is always true that fracture events have similar power spectra with each other, and their energy is concentrated on higher frequencies than it is for the noise signal, so a discriminating criteria can

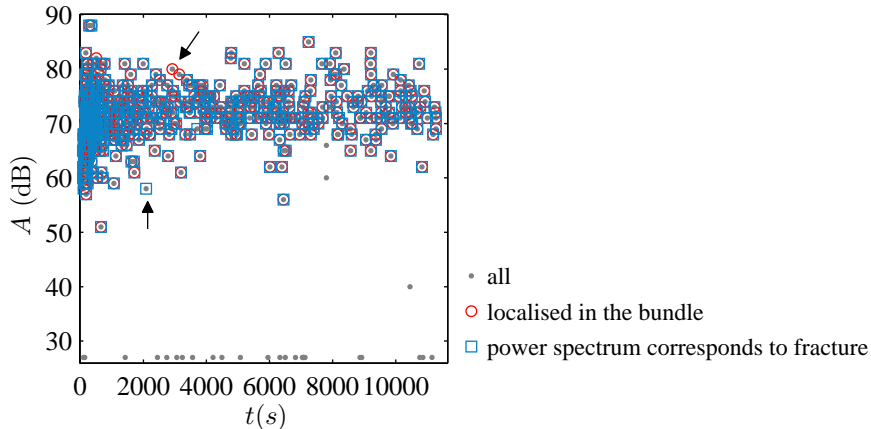


Figure 2.11: Time amplitude diagram of the acoustic events. Gray dots: all acoustic events. Red circles: acoustic events localised within the bundle. Blue squares: acoustic events having a power spectrum corresponding to fracture.

easily be established for each experiment. We assured that some noise is recorded at the beginning of each experiment so that we could verify the efficiency of the discriminating method.

3.4 Some basic considerations on mechanics

During each experiment we directly recorded the force F applied to the bundle, the force F_{max} reached at the end of the loading, the number of AE bursts and the position of the mobile bar of the testing machine (figure 2.9.b). Knowing the mechanical properties of the bundles (dimensions and Young modulus) and having made some calibration tests before the series of experiments, for each experiment we can extract:

- N_0 , the exact number of fibres in the bundle. N_0 varies between 1500 and 2200.
- $n_{loading}$, the number of broken fibres during the loading.
- n , the number of broken fibres after the loading.
- ϵ , the strain of the bundle, which is of the order of 1%.
- F_{fib} , the force per fibre applied to the bundle. Note that once the loading is done, the deformation is constant and so is F_{fib} . Two independent ways of calculating F_{fib} were used, one based on the force measurement during loading (F_{fib}^F), and the other on the AE recordings (F_{fib}^{AE}). Typical values are around 0.1 N.
- σ , the stress applied to each fibre, deduced from F_{fib} , which is of the order of 700 MPa.

Details about these calculations can be found in appendix C.1.

3.5 Strength distribution of fibres

Due to variability in the flaw size, fibres have different strengths. Using experiments where the bundle is loaded with a constant strain rate until rupture, it is possible to estimate the distribution of strength σ_s by counting the number of fracture events

which occurred at given strain. The distribution follows a Gaussian (figure 2.12⁴), with a mean value $\sigma_c \sim 1.1$ GPa.

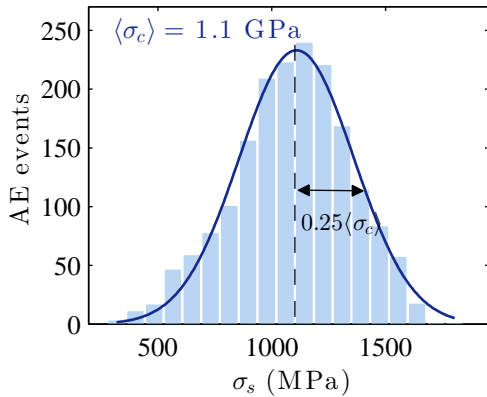


Figure 2.12: Histogram of fibres strength.

The distribution of the fibres' strengths was calculated for all bundles used for the constant strain experiments, using only data from the loading phase. This allowed to detect anomalous bundles (presenting too many weak fibres) and rule them out from the analysis. Details about the determination of σ_s are given in appendix C.2.

3.6 Experimental results

3.6.1 A typical experiment

Figure 2.13.a shows the three physical quantities that we follow during each experiment. The test machine loads the bundle by imposing a constant strain rate. The strain ϵ is represented with a dashed blue line, with a multiplicative factor corresponding to the stiffness of a bundle with N_0 fibres. The force is represented with a plain blue line. During the beginning of the loading the measured force and the one calculated using ϵ are the same. As soon as fibres start breaking, the measured force F deviates from the linear force-time curve. When a force F_0 is attained the loading stops, and a constant strain is maintained. During the relaxation phase, as fibres break, the force applied to the bundle decreases. The AE activity is very high during the loading and the beginning of the relaxation phase, then decreases rapidly with time. Figure 2.13.b shows the same quantities but concentrates on the loading phase.

The decreasing number of surviving fibres in the bundle $N^{AE}(t)$ is represented on figure 2.13.c. It was calculated by subtracting the number of detected acoustic events from the initial number of fibres in the bundle. The number of surviving fibres and the total force F are related by the force per fibre $F_{/fib}$:

$$F = F_{/fib} N^{AE}, \quad (2.5)$$

which can be seen on figure 2.13.d.

This result is trivial but useful: we used it to check the reliability of our measurements. Few experiments did not show a linear relationship between F and N and

⁴Results from CERA group internal report (M. R'Mili)

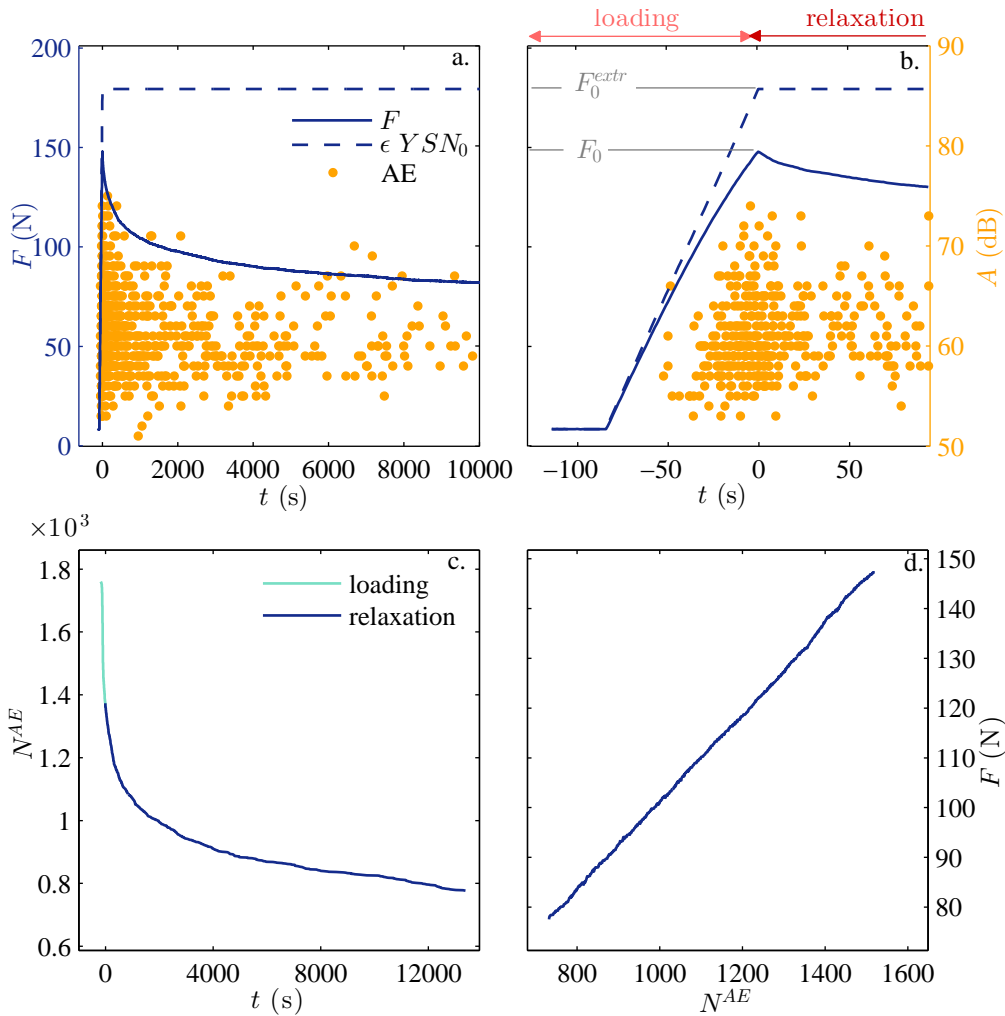


Figure 2.13: (a) Main quantities measured during the experiment. Dashed blue line: strain (with a multiplicative factor) imposed to the bundle by the testing machine. Plain blue line: measured force on the bundle. Orange circles: amplitude of the detected AE events. (b) Zoom on the same quantities, for short times. (c) Evolution of the number of surviving fibres with time. (d) Number of surviving fibres calculated using AE vs force applied to the bundle, during the relaxation (constant strain) phase.

The experiment was done at $T = 23^\circ\text{C}$ and $\sigma = 659 \text{ MPa}$.

were ruled out from the analysis. This behaviour may be due to a twisted bundle (so some of the force is redistributed by friction), a problem in the deformation control, or strong variations of the AE detection sensitivity. All the remaining experiments showed a linear relation between F and N . For four of them the estimated value of $F_{/\text{fib}}$ was larger than the one calculated previously (see annexe C.1, equation 12 for details). We suppose this to be due to incomplete acoustic burst detection. These experiments were kept for the analysis since they can be used for studies on the force decrease. The remaining bundles were found to have similar values of $F_{/\text{fib}}$ for the two estimations.

3.6.2 Total number of broken fibres

We studied the total fraction of broken fibres n/N_I within 10^4 seconds after the loading for the different experiments (figure 2.14). We consider the force measure-

ment more reliable than AE monitoring, so the calculation of n/N_I will be based on the force decrease. Since the number of fibres is proportional to the force, n/N_I was calculated as $1 - \frac{F(t=10^4\text{s})}{F_{max}}$. As expected, n/N_I increases with the applied stress on the bundles, except for one experiment at room temperature which had an abnormally low number of broken fibres, without showing any other abnormal behaviour. For cold water the number of broken fibres is the lowest. Surprisingly, experiments at 45°C experience less fracture than the ones at room temperature. For the time being we are wondering if an explanation could be the use of tap water for our experiments. Hot water, being heated in a boiler, may have a slightly different composition than water at room temperature or cold water.

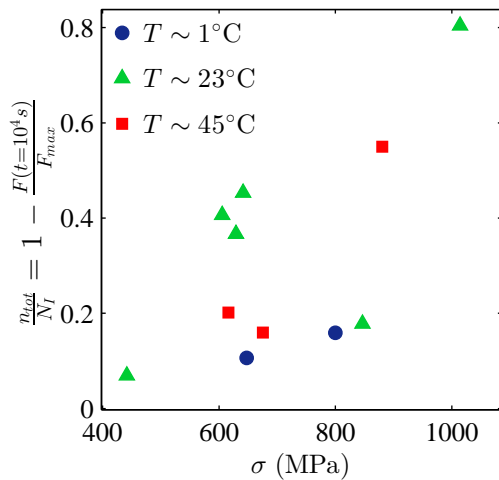


Figure 2.14: Total fracture of broken fibres within 10^4 seconds of each experiment n_{tot}/N_0 , regarding the applied stress σ . Different symbols represent different temperatures: 1°C (○), 23°C (△), 45°C (□).

3.6.3 Omori law

In accordance with what was observed for simulations, the number of broken fibres per unit time dn/dt decreases with time as a power law, for mean and long times (figure 2.15). For most experiments a power-law regime establishes at around $t = 100$ s (and even earlier for some). Because of the AE detection problems identified earlier (section 3.6.1), we can not solely rely on AE for the calculation of the number of broken fibres. Hence we will simultaneously use AE and the force decrease for the estimation of n . The number of broken fibres within an interval $[t, t + \Delta t]$ was either estimated as the number of AE events occurring during the interval, or as the force decrease divided by the force per fibre F_{fib}^F . The results from the two methods are very similar for the experiments with reliable AE detection (for an example see figure 2.15.a). For the experiments with incomplete AE detection there was an almost constant shift between the values of dn^{AE}/dt and dn^F/dt (figure 2.15.b).

For each experiment we fitted⁵ dn/dt as a power law for $t \geq 10^2$ s. The resulting exponent p is represented as a function of the applied stress σ , for different values

⁵The fit was done on several curves (about 10, depending on the number of broken fibres) representing the same data with different bin sizes. The resulting p is the mean value of all the estimations, and the incertitude on p is the standard deviation of all the calculated values.

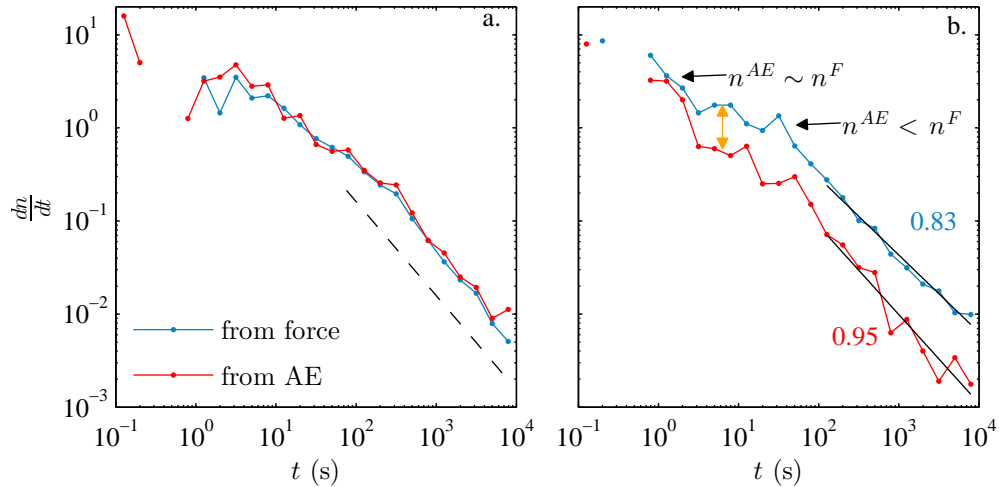


Figure 2.15: Evolution of dn/dt with time, calculated using the number of acoustic events (red) or the force decrease (blue). (a) Experiment with no AE detection problems, at room temperature and $\sigma = 641$ MPa. (b) Experiment where some AE events were missing, at room temperature and $\sigma = 606$ MPa.

of the temperature, in figure 2.16. Open and full symbols represent the Omori law exponent calculated using the acoustic signal (p_{AE}) and the force decrease (p_F), respectively. The values of p_{AE} and p_F match with each-other when incertitudes are taken into account, except for the experiments with acoustic detection problems, marked with black arrows. In the rest of the chapter we will only rely on the value of p_F .

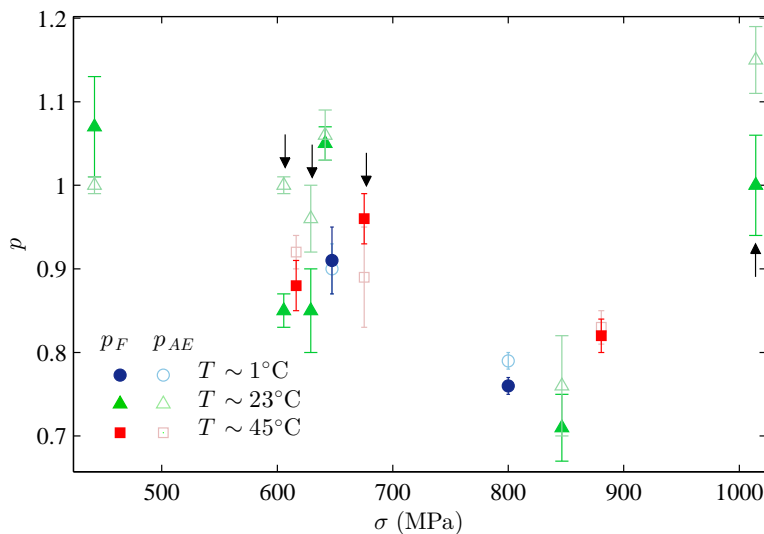


Figure 2.16: Variation of the exponent of the power law distribution of the fracture events p with the stress σ applied to the fibres. Different symbols represent different temperatures: 1°C (\circ), 23°C (\triangle), 45°C (\square). Open symbols: p calculated using the acoustic signal. Full symbols: p calculated using the force decrease. The black arrows point at the experiments where acoustic events are missing (section 3.6.1).

To facilitate the interpretation we represent only p_F on figure 2.17. The results are separated by temperature, and also by the total fraction of broken fibres n_{tot}/N_0 (the schematic representations of the fibres' strengths on top of figure 2.17 show the difference in the bundles involved in the estimation of p). For the simulations on fibre bundles we saw that this parameter is very important since it delimits two different behaviours regarding the disorder temperature (section 2.2.1).

Firstly one can see that the results are not easily reproducible. There are three experiments done at room temperature having similar applied stress (between 600 and 650 MPa), and they show an important difference in the calculated value of p ⁶. Even so, some tendencies can be observed on this figure.

There does not seem to be any systematic variations of p with the temperature. Since an unusual behaviour was detected when studying the total fraction of broken fibres for high temperature experiments (section 3.6.2) it is possible that the estimation of p is also biased. Still, low and room temperature also seem to result in similar p values.

p varies with the applied stress. For experiments with $n_{tot}/N_0 \leq 0.6$, p decreases

⁶This dispersion of the results as well as the dependence of p with σ are not artefacts arising from the varying fibre strength. This was verified by comparing results for bundles having very similar fibre strengths, and also by observing the differences between bundles with different bundle strengths

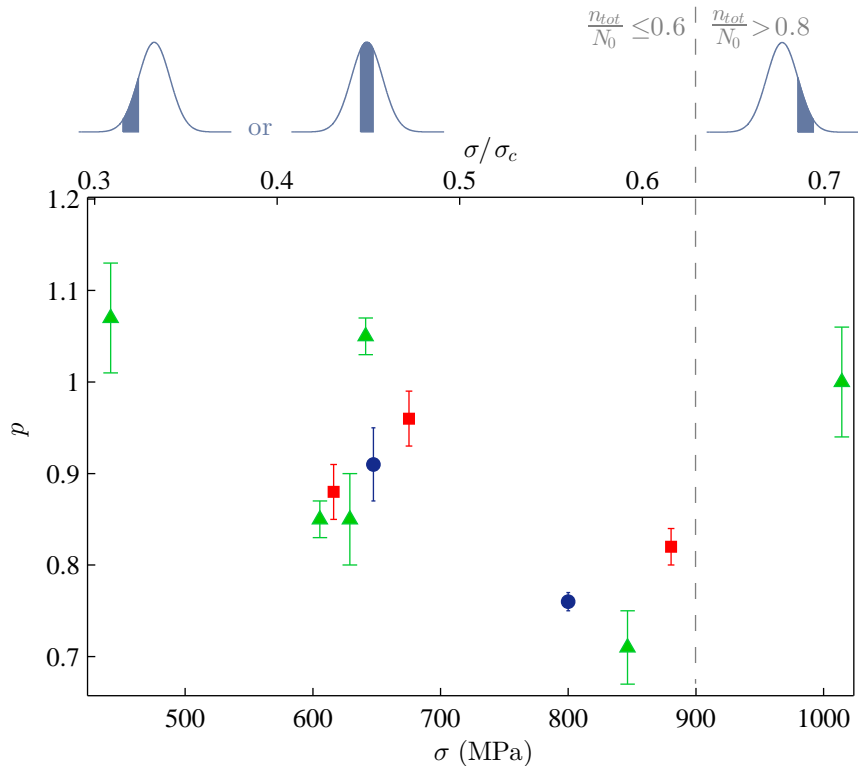


Figure 2.17: Variation of the exponent of the power law distribution of the fracture events p with the stress σ applied to the fibres. Different symbols represent different temperatures: 1°C (○), 23°C (\triangle), 45°C (\square). The schemas on the top represent the strength distribution of the fibres, and the coloured part corresponds to the part of the distribution used for the determination of the power law.

with σ . There is only one experiment with $n_{tot}/N_0 > 0.6$, so we can not know how p varies with stress in this regime.

4 Comparing experiments and simulations

The most obvious observation from the experimental data is that when the fracture concerns the low and mean-strength fibres from the bundle (less than 60% of the bundle is broken) the exponent of the Omori law decreases with the increase of the applied stress σ . For the simulations the exponent of the Omori law systematically increases with σ regardless of the other parameters. We think that one explanation for the difference between experiments and model could be due to the subcritical fracture propagation within the fibres (section 3.1) which is not taken into account by the model.

Let us consider that fibres become weaker with time during the experiment. Obviously, this increases the number of fracturing fibres at long times - as fibres weaken they are more likely to break. Hence the number of fractured fibres does not decrease as fast as expected, making p decrease. Furthermore, stress corrosion is more effective when stress increases, so the higher the stress, the more important the effect of the subcritical fractures. The decrease of p with σ could be explained by the increased damage accumulation in the fibres when σ increases. To our knowledge, the effect of damage accumulation has only been studied in fibre bundles submitted to a constant load. In this case, for democratic load-sharing the ageing accelerates the already accelerating dynamics of fracture [72].

Developing a model matching the experimental results needs more experimental results than the ones we presented. Damage accumulation can simply be added by making the failure threshold of each fibre σ_s decrease in time, like in [56]. This seems like the best approach for glass fibres in water, since the decrease of σ_s corresponds to an increase of the flaw length, which is the actual physical consequence of stress corrosion. The way σ_s decreases should take into account the microscopic mechanism of stress corrosion of glass (section 3.1).

5 Conclusion and perspectives

We studied the fracture of a bundle of E-glass fibres under constant strain and immersed in water. We established an experimental protocol where fracture is monitored with one acoustic sensor and the force decrease is continuously recorded, and we proposed verifications which need to be applied to experimental data in order to verify their quality (mostly based on the comparison between AE and force measurements). The results from the experiments were compared to simulations of thermally activated fracture in a fibre bundle model.

At constant strain, the number of broken fibres per unit time dn/dt decreases as a power-law with time. This applies for both simulations and experiments, at long times (approximately $t > 10^2 s$). The experimental results showed an important variability for p , even when experiments are made in similar conditions. Nevertheless, we could observe that experimentally the exponent of the power law p seems

to decrease as the applied stress increases. This behaviour does not correspond to results from FBM simulations, where p systematically increases with σ . The difference between experiments and model was attributed to the damage accumulation in fibres (subcritical fracture of nanocracks within each fibre, due to stress corrosion) which is not taken into account in the model.

More experiments are needed in order to confirm our conclusions. The same experimental protocol could be applied, but with replacing tap water by distilled water (or simply not using boiler water for high temperature experiments) for the observations about the influence of temperature to be reliable. Once the experimental results are well established, it could be possible to compare them to existing damage accumulation FBMs, or eventually create a new model.

Part II

Earthquake statistics

CHAPTER 3.

SOME HISTORY AND A FEW TECHNICALITIES

1	Introduction	54
1.1	Time clustering of earthquakes	54
1.2	Our focus: mainshock-aftershock sequence	55
2	The statistics of aftershocks - a matter of details	55
2.1	The well known (power) laws	55
2.2	Short time aftershock incompleteness - STAI	60
2.3	Magnitude correlation	62
2.4	b-value and differential stress	62
2.5	Earthquake triggering	63
2.6	The challenge of studying earthquakes	64
3	Methods	66
3.1	Data collection	66
3.2	Extracting the power law exponent	66
3.3	Dealing with STAI	72
3.4	Simulations The Branching Aftershock Sequence Model	72

1 Introduction

Earthquakes are the consequence of a combination of fracture and stick-slip in the earth crust. Fault slip can occur on lengths from less than a centimetre to hundreds of metres, resulting with earthquakes of “all scales”. With a span of over 10 decades of magnitudes¹, and times going from tens of seconds to more than decades², both obeying power-law distributions, earthquake data is probably what resembles best a scale-invariant phenomenon on earth. This process is monitored by more than 22000³ stations worldwide, generating tremendous quantity of seismic information.

There is a variety of different approaches suitable for the study of earthquakes. In the case of geophysical surveys, extremes go from studying one single earthquake in details (by describing its fault type, fracture speed, stress level, stress drop, radiated energy, etc. [57, 58, 102]) to studying thousands of earthquakes considering only a few of their properties. In this thesis it is the later (statistical) approach that prevails. We will consider earthquakes as punctual events characterized by their occurrence times, magnitudes and positions, and study the statistical properties of large groups of earthquakes in Japan and California. Our work on earthquakes was initially motivated by the results on paper fracture experiments, so it is oriented towards aftershocks and correlations considerations. We will discuss the probability distributions of aftershocks times and energies, and mostly try to understand how and why they vary.

1.1 Time clustering of earthquakes

Earthquakes are clustered in time and space. Temporal clustering is often related to the existence of a great earthquake, followed by aftershocks which are close in time. Spatial clustering is directly related to the distribution of faults whose slip generates earthquakes. The causality relations between earthquakes will be discussed in section 2.5. Here we will only remind some definitions about classifications of clustered earthquakes.

Large and shallow earthquakes are very likely to be followed by numerous daughter earthquakes, named *aftershocks*. Just like in the case of paper fracture experiments, it is the heterogeneity of the medium (the earth crust) that causes the intermittency of the process and the existence of aftershocks. The stress released during a major earthquake is redistributed on the neighbouring, disordered faults. The faults that have been subjected to an already large stress would then experience failure [96]. Large earthquakes can also be preceded by more-than usual smaller earthquakes, i.e. *foreshocks*, which are fewer and less intense than aftershocks. Aftershocks and foreshocks are both temporally correlated to the mainshock, as they are most numerous near the mainshock. Groups of earthquakes can also occur closely in time and space, with no significant mainshock nor power law distributed times: this constitutes an earthquake *swarm*.

¹The largest earthquake detected in the last decades is the Valdivia (Chile) earthquake in 1960, of magnitude 9.5 and with the current sensitive seismographs even earthquakes with negative magnitudes are detected

²Aftershock sequences have been shown to last for decades, but some authors discuss even longer durations[137]

³Number of seismic stations in the International Registry of Seismograph Stations

Since there is no physical difference between mainshocks, aftershocks and foreshocks [51, 52, 129], this classification is completely artificial and can only be done *a posteriori*. Furthermore, the aftershock of one sequence can provoke its own secondary aftershock, hence becoming a mainshock. Thus most of the time determining the links between earthquakes is complicated. In order to tackle this problem we focused our attention on the simplest scenario of correlated earthquakes, a mainshock-aftershock sequence with very few secondary aftershocks.

1.2 Our focus: mainshock-aftershock sequence

Most of our work on earthquakes will concern one particular earthquake configuration: one very intense mainshock producing a series of aftershocks, which produce no or very few secondary aftershocks⁴.

We will refer to it as a mainshock-aftershock (ms-as) sequence. This considerably simplifies our work: a long and strong aftershock sequence with negligible secondary aftershocks is easy to identify, characterise and simulate. Its activity is high above background activity for a very long time so we do not have to take the former into account. Moreover, this configuration is the most suitable for the features that we will discuss, such as magnitude correlation for earthquakes close in time, or temporal variation of the exponent of the earthquake energy.

2 The statistics of aftershocks - a matter of details

2.1 The well known (power) laws

Aftershocks are characterised by power laws, whether one looks at their energy, occurrence time, or position relative to the mainshock. For a long time, these power laws were considered to be robust and their exponents constant within an aftershock sequence, without any variation with respect to time, magnitude threshold, dead-time of the detection or power-law span. Hence, an aftershock sequence used to be characterised by calculating a few constants, and this approach is still used when an aftershock sequence is being globally described [92, 131, 143].

In reality, aftershock sequences are more complex than this. When they need to be described more thoroughly, variations and interdependencies of the different parameters come up. Some of these features remain unexplained or even unclear. It also can occur that studies treating the same issue render different results or interpretations, mostly because the data processing methods or the studied regions are different. This section will provide a reminder of the "well known" power laws on earthquakes, and a summary of the recent (controversial) features, their (un)robustness with respect to certain parameters, and some important technical details.

⁴See section 3.1.1 for details.

2.1.1 Omori law

The first law established about earthquakes concerns their occurrence times. In 1894 F. Omori proposed a power law for the decreasing number of earthquakes, with a constant exponent equal to 1 [100], now known as the Omori law:

$$n(t) = \frac{K}{(t + c)}. \quad (3.1)$$

We now use the Omori law in its modified form [144], which allows for the activity to decrease faster or slower than in the equation 3.1:

$$n(t) = \frac{K}{(t + c)^p} \quad (3.2)$$

where $n(t)$ is the number of earthquakes in a time interval $t + \Delta t$ after the mainshock and K , c and p are constants. K is related to the productivity of the sequence, p is an exponent close to 1 describing the decrease of the number of aftershocks in time and c is the time immediately following the mainshock, during which aftershock productivity is roughly constant (figure 3.1.d).

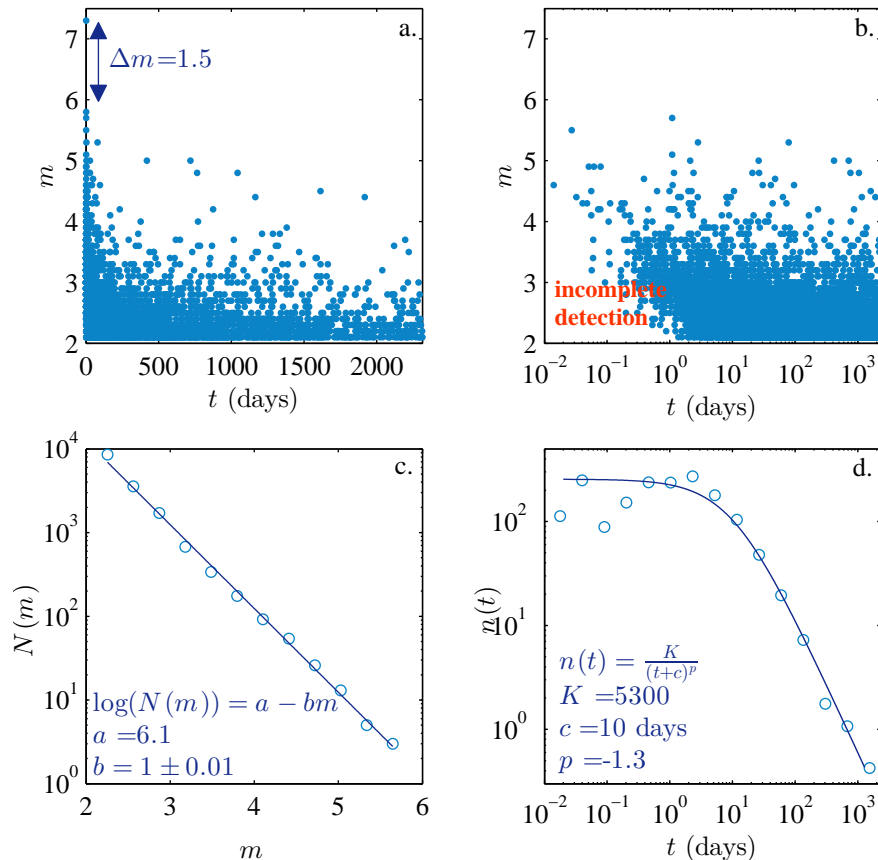


Figure 3.1: The Landers earthquake aftershock sequence (California 1992). (a) Time-magnitude representation of the sequence. The double arrow represents the magnitude difference between the mainshock and the largest aftershock. (b) Time-magnitude representation with logarithmic time. Notice low amplitude events are missing in the beginning of the sequence. (c) Gutenberg-Richter law. (d) Omori law.

The constant c is very difficult to estimate due to incomplete detection of small aftershocks. Immediately after a mainshock small aftershocks are impossible to detect since their signal is covered with the mainshock coda and bigger aftershocks [49, 62, 103] (see discussion in section 2.2.1). When this problem was pointed out [62], efforts were made to get a more accurate estimation of c , but it is still unclear to what extent the estimate of c is biased by the incomplete detection of small aftershocks. Though zero and even negative values of c have been proposed [63], the idea of a positive c -value seems to prevail. Recent studies in which small earthquakes were carefully detected show that c is very small (a few minutes, a duration that could correspond to the mainshock's fault rupture) and positive [34, 103, 130].

The exponent p on the other hand is quite robust regarding the mainshock magnitude or the magnitude threshold [88]. For different aftershock sequences or different regions its value varies from 0.6 to 2 [144] and has been shown to depend on the temperature [65, 90, 98] and the heterogeneity of the stress distribution [54].

Nevertheless, some recent studies suggest that the Omori law is actually made of two power laws: one low exponent power law for small times after the mainshock, then a larger exponent power law for longer times [27, 103].

2.1.2 Gutenberg-Richter law

The most general law about earthquakes is the Gutenberg-Richter law [47]. It is valid at local and global scales, for background seismicity as well as for triggered seismicity. It states that $N(m)$, the number of earthquakes having a magnitude equal or greater than m , verifies:

$$\log_{10}(N(m)) = a - bm, \quad (3.3)$$

where a and b are constants characterising the sequence (figure 3.1.c). Though this law indicates that magnitudes are distributed following an exponential, one must remember that magnitudes are only a logarithmic measure of earthquakes' amplitudes or energies, and these two variables are distributed following power laws.

Since the energy E of the earthquakes is proportional to $10^{\alpha \cdot m}$ ($\alpha \sim 1.5$) [48, 50], the number of earthquakes having an energy greater or equal to E follows a power law:

$$N(E) \propto E^{-b/1.5}. \quad (3.4)$$

Thus, the probability of an earthquake with energy E occurring is:

$$p(E) \propto E^{-\beta_E}, \text{ where } \beta_E = b/1.5 + 1, \quad (3.5)$$

and $\beta_E \sim 5/3$ for $b = 1$.

The exponents b and β_E provide the same information about earthquakes, and are related to the number ratio of small to large earthquakes. β_E is here analogue to the exponent β we calculated for the energy distribution of fracturing paper (section 3.3.2, chapter 1). The constant b from equation 3.3, commonly called *b-value*, is systematically used in geophysics and seismology studies. For consistency with previous studies we chose to also work with b rather than β_E .

The exact determination of the exponent of the energy distribution is very important for earthquakes, as it is for characterizing any scale-invariant phenomena (section 3.1 in Introduction). In the case of earthquakes, however, this estimation can be vital, since it is crucial for earthquake forecasting. In the Introduction (3.1) we showed that small variations in the value of the exponent cause significant changes in the probability of great events occurring. The difference between Japan and California seismicity illustrates this point very well. We examined data from central Japan and south California, for the period from 2002 to 2012, considering only earthquakes with magnitudes ≥ 3 . The difference in the b-values is small: $\Delta b = 0.12 \pm 0.03$ (figure 3.2.c), but the change in the number of very strong earthquakes is remarkable. Figures 3.2.a and b show that the number of earthquakes with magnitudes higher than 6 is ten times higher in Japan (0.3% of all earthquakes) than in California (0.03%).

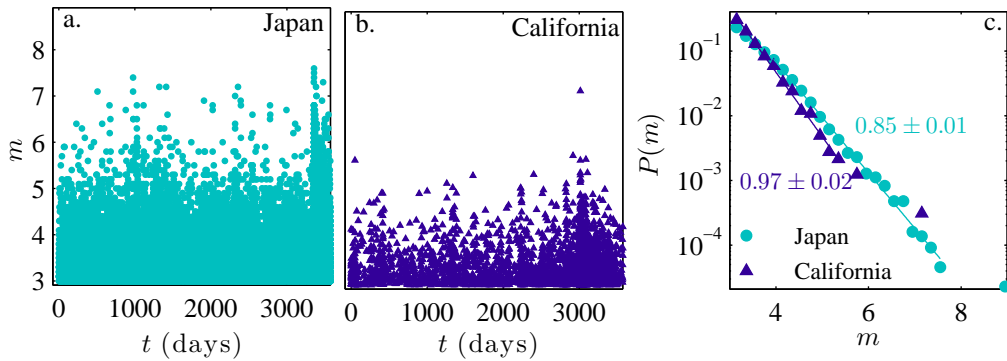


Figure 3.2: (a) and (b): Magnitude-time diagrams of earthquakes in central Japan and south California respectively, for the period from 01.01.2002 to 01.01.2012. (c) Probability distribution of the earthquakes in central Japan (light circles) and south California (dark squares).

The b-value can present important variations on local scales, which are often related to the crust heterogeneities or the differential stress level [33]. Its value can differ within distances of several kilometres. A map of the b-value of the aftershocks of the Tottori earthquake in Japan is shown in figure 3.3. Though the earthquakes have a common mainshock, a single b-value cannot be defined since the spatial variations are strong.

2.1.3 Båth law

Another empirical law about aftershocks is the Båth law, which states that the magnitude difference Δm between a mainshock and the largest aftershock of its sequence is *on average* equal to 1.2:

$$\Delta m = 1.2, \quad (3.6)$$

and this difference is independent of the mainshock magnitude. The validity of this law is still discussed, some authors [52] arguing that the value of Δm is a result of the way mainshocks and aftershocks are chosen and can be linked to the productivity (number of aftershocks triggered by the mainshock) of a sequence.

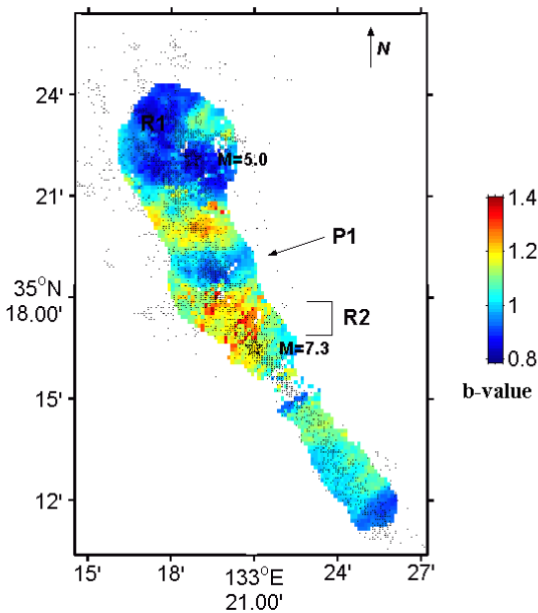


Figure 3.3: According to [33]: b-value map for the aftershocks of the 2000 Western Tottori earthquake.

For simulations, strictly imposing the value of the largest aftershock magnitude seems unrealistic. In this case a much more elegant solution is proposed with the modified Båth law [132]. Rather than imposing the magnitude of the greatest mainshock, the modified Båth law only imposes the number of aftershocks which have a magnitude greater than $m_{ms} - \Delta m$, by fixing it to 1:

$$\log_{10}(N(\geq m_{ms} - \Delta m)) = a - b(m_{ms} - \Delta m) = 0. \quad (3.7)$$

Thus one can replace the constant a from the Gutenberg-Richter law (equation 3.3) by $b(m_{ms} - \Delta m)$, and the probability distribution of aftershocks provoked by a mainshock with magnitude m_{as} is:

$$\log_{10}(N(\geq m)) = b(m_{ms} - \Delta m - m). \quad (3.8)$$

This result is often interpreted as a truncated Gutenberg-Richter law, though the magnitudes of the aftershocks are not actually truncated⁵. What equation 3.8 controls is the number of generated aftershocks. This number will depend on the difference $m_{ms} - \Delta m$, and will increase as this difference increases. There is no direct link between the magnitude of the mainshock and its largest aftershock⁶. It is the combination of the number of generated aftershocks and the Gutenberg-Richter law which makes it probable to have only one aftershock with magnitude greater than $(m_{ms} - \Delta m)$.

⁵The magnitude of the largest generated aftershock is not limited: it can even be greater than the mainshock magnitude (which is a rare occurrence but does happen in nature).

⁶This is an important aspect of how we currently consider aftershocks. While we know they form clusters in space and time, very few studies consider magnitude clustering. In general aftershocks magnitudes are considered to be independent from each other and from the mainshock magnitude. This is an issue that will be discussed later.

2.1.4 Spatial distribution of aftershocks

Though a strong earthquake can remotely trigger aftershocks on long distances, most of the aftershocks occur closely to their parent mainshock. Studies suggest that the distance from the mainshock also follows a power law, with an exponent close to 2 [37, 38, 81]. The distribution is often anisotropic, following fault lines, crust asperities and high stress regions (see figure 3.4 for an example of spatial distribution of earthquakes in California).

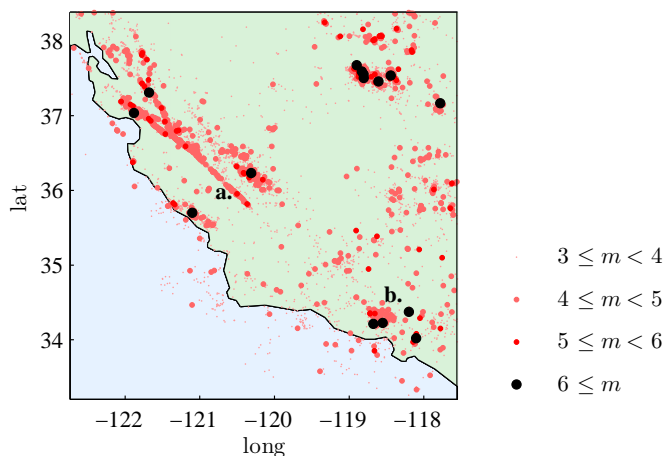


Figure 3.4: Example of spatial distribution of earthquakes in north California, which occurred between 01.01.1980 and 01.01.2013. While some earthquakes are concentrated on fault lines (a) others form clusters (b). In both cases visual identification of event groups is quite easy.

2.2 Short time aftershock incompleteness - STAI

At the beginning of an aftershock sequence the number of small magnitudes events figuring in the catalogues is unexpectedly small (compared to the number of high magnitude events). The effect can be seen in figure 3.1.b. In this figure are represented the occurrence times and magnitudes of the earthquakes from the Landers earthquake aftershock sequence. For short times after the mainshock all small earthquakes are missing. While it is possible that weak earthquakes are indeed less numerous shortly after the mainshock⁷, we know that an important part of the early aftershocks, especially the weak ones, are simply missing from the catalogues. Indeed, when a weak earthquake occurs shortly after a strong one, its signal might not stand out in the coda of the preceding strong earthquake. Since a great mainshock has a long coda (which can last up to hundreds of seconds) and its first big aftershocks will also have long codas, many of the weak magnitude aftershocks can not be detected shortly after a great mainshock [49, 62, 103]. We will refer to this effect as *short time aftershock incompleteness* (STAI).

The existence of STAI was confirmed by studies which directly point out the missing aftershocks, using continuous seismogram recording rather than catalogue entries. Peng et al [103] showed that five times more earthquakes can be detected within

⁷The possibility of magnitude correlation among aftershocks and the difference between early and late aftershocks will be discussed later in this thesis.

the first 200 seconds on a mainshock, by studying the high frequency part of the recordings (figure 3.5.a). Figure 3.5.b shows a comparison between earthquakes from NCSN catalogue (arrows) and earthquakes hand-picked by Peng et al. (stars): many early aftershocks are indeed missing from the earthquake catalogues. It is striking that even earthquakes with amplitudes comparable to the $m = 4.2$ earthquakes are missing (figure 3.5.b).

Although this may seem like a technical detail, its consequences on the estimation of earthquake properties are very important. In particular, it is obvious that all considerations about early aftershocks must take into account the fact that a large part of these aftershocks is actually missing.

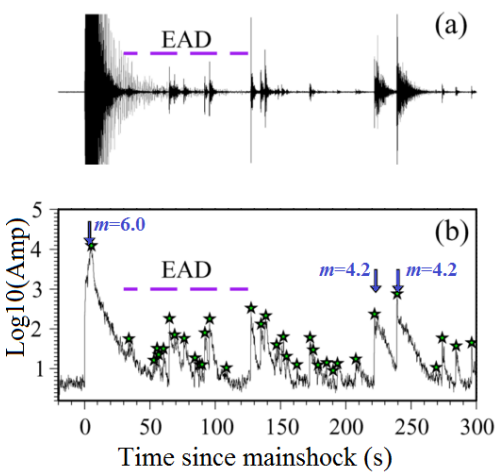


Figure 3.5: According to [103]. (a) Original (gray line) and high-pass-filtered (dark line) vertical-component seismogram recording for the 2004 Parkfield earthquake. (b) Logarithm of the envelope (dark line) generated by stacking the envelopes the signal in (a). Stars marks events identified by a handpicking procedure. The vertical arrows mark the two events listed in the NCSN catalogue. The dashed purple line marks the time period when Early Aftershock Deficiency (EAD) is observed.

2.2.1 STAI and Omori law's c value

STAI renders the estimations of the Omori law dead time c particularly difficult. The under-reporting of aftershocks at short times completely modifies the estimated value of c [62, 63]. As a result, this value depends on the minimal threshold magnitude used for the calculation [130]. As figure 3.6 shows, the bigger the magnitude threshold, the smaller is the value of c . Moreover, the value of c seems to coincide with the time at which the detection of earthquakes with magnitudes greater than M_c is complete (black squares on figure 3.6.a). It seems that values of c calculated on earthquake catalogue data are actually estimations of the duration of STAI effects.

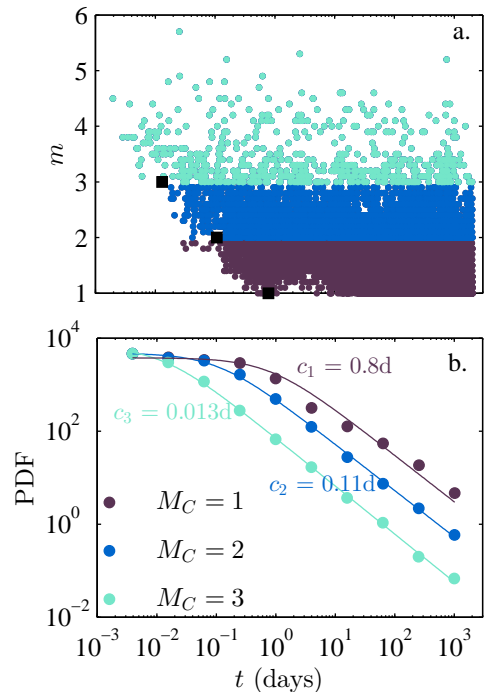


Figure 3.6: (a) Time-magnitude diagram of an aftershock sequence. The black squares represent the value of c fitted for $M_c = 1, 2$ or 3 form a line that corresponds to the completeness magnitude. (b) Fit of the modified Omori law (equation 3.2) and estimation of c for events such that $M_c = 1, 2$ or 3 .

2.2.2 STAI and magnitudes statistics

It is obvious that under-reporting small events alters the small to big event ratio. Whenever small events are missing from the statistics, the calculated b-value will be an underestimation of the real one. In section 3.3 we describe how we dealt with STAI for the studies on early aftershocks b-value.

2.3 Magnitude correlation

The temporal correlation of earthquakes, manifested by the existence of aftershocks, has been known for a long time. The question about the existence of magnitude correlations, on the other hand, is a rather new one. Lippiello et al. [73, 74] studied the probability of two earthquakes having similar magnitudes when they occur closely in time and space. They showed that this probability is significantly higher when using the original data from earthquake catalogues than for catalogues with reshuffled magnitudes. This indicates that magnitudes of earthquakes close in space and time are correlated. These results were immediately followed by discussions on whether they are a spurious effect due to STAI [28], or not [76].

The importance of this question lies in the fact that the current widely-accepted models of seismicity are based on the idea of independent magnitudes [95, 142]. If a correlation indeed exists, these models, as well as the approaches for forecasting seismicity rates will have to undergo substantial change. Results confirming [73, 74, 76] and dismissing [28, 29, 71] the existence of magnitude correlations are still being presented and this subject remains an open question.

2.4 b-value and differential stress

When observing at a global level, the b-value does not vary significantly; there is little difference between the b-values of different tectonic regions [41, 61]. This result holds as long as the observation regions have lengths of hundreds or thousands of kilometres. Nevertheless, when it comes to local or regional scales the variations of the b-value are obvious (e.g. 3.2.c and 3.3).

The first observation of a link between stress and the b-value was made in 1968 by C. H. Scholz [126]. He measured b-values for the fracture of rock samples and obtained b-values that decrease with increasing differential stress applied to the rock, and do not vary regarding the confining pressure. He interpreted this with a model suggesting that when the differential stress is higher, large fractures are more probable to propagate by connecting two remote regions of high stress. The increased probability of large fractures results in a lower b-value. The idea of earthquake mechanisms being similar to fracture was already known, so he supposed that this kind of variation of the b-value should also be observed for earthquakes.

It took almost 50 years for Scholz to propose a quantitative relationship between the differential stress and the b-value [125]. The main difficulty of this subject is that since stress in the earth crust is not obvious to estimate, proving its influence on the b-value is difficult. Typically, studies on the subject relate the stress to some other measurable parameter, in order to deduce a stress - b-value relationship. For example, variations of b with focal mechanism⁸ [128] or depth [125, 134] have been

⁸The focal mechanism is a description of the fault motion during slip. Different mechanisms are associated to different fault types (see figure 5 in the Introduction).

related to stress variation. These findings combined with results from laboratory experiments designed to simulate earthquakes [5, 146] established the differential stress as the main parameter influencing the b-value.

2.5 Earthquake triggering

Although earthquakes serve the overall function of relieving built-up elastic stress in the crust, in some cases stress is redistributed on other faults, making them slip after some time delay (which may last up to few years) and provoking another earthquake. This defines one type of earthquake triggering (static triggering). Note that the stress change that can provoke an aftershock is very small compared to the stress drop occurring during the aftershock [136], meaning that stress changes provoked by one earthquake do not *cause* other earthquakes, they just *trigger* them, on faults which are already under high stress.

We distinguish between two triggering mechanisms: static and dynamic triggering. They differ by their mechanisms and the distance at which they act.

2.5.1 Static triggering

Static triggering explains the delayed (up to few years after the mainshock) and localised occurrence of aftershocks after a large earthquake. When a slip occurs at an earthquake fault (this is the slip related to the mainshock), the stress distribution near the fault changes. The stress change does not only concern the fault's extremities but also its surroundings [64]. Depending on the geometry of the fault and of the neighbouring faults, some regions will experience stress increase, and others stress decrease. Aftershocks will occur mostly in regions experiencing a stress increase (figure 3.7). In these regions faults are brought closer to failure, and will

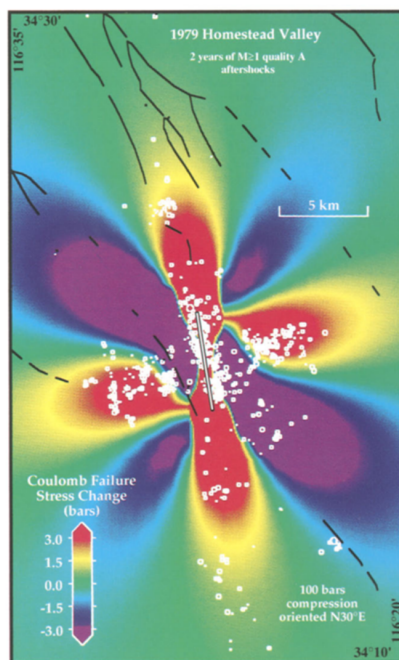


Figure 3.7: According to [64]: stress changes caused by the 15 March 1979 Homestead Valley earthquake sequence. The fault is represented with a white line. The stress increase regions (red color) correspond to the localisation of most of the aftershocks (white dots).

experience fracture much sooner than expected without the initial slip. The region subjected to significant static stress change defines the *aftershock zone*. The static triggering is at the origin of aftershock sequences following the Omori law [39].

While static triggering explains the aftershock occurrence near the parent earthquake (at a distance of a few fault lengths, which we refer to as the aftershock zone), it cannot explain the long-distance triggering that is sometimes observed.

2.5.2 Dynamic triggering

Earthquakes can trigger seismicity at distances far beyond the aftershock zone, in regions where the static stress change is too low to cause considerable effects. A famous example of this remote triggering is the seismic activity all over the west of the United States that increased after the Landers earthquake in 1992 [6], sometimes at distances as far as 1000 km. This kind of triggering, called dynamic triggering, is due to the passage of transient seismic waves after a large earthquake. The peak dynamic stresses associated with a seismic wave are important enough to trigger earthquakes immediately, or to alter the crust structure enough to accelerate the dynamic of earthquakes.

It is obvious that any remote triggering can not result from static stress changes, and is thus provoked by dynamic triggering. Nevertheless, dynamic triggering can also occur at small distances. It is still unclear which triggering method prevails in the aftershock zone (recent studies on this question are summarised in [135]), some authors even suggesting that static stress change does not trigger earthquakes at all [37].

2.6 The challenge of studying earthquakes

Earthquakes have been intensively studied for more than a century. Still, from the geophysics point of view, very few laws persisted through time without major modifications. New features about earthquakes are constantly discovered, and old ones are often questioned.

Many crucial issues are still being debated, like the value of the Omori law's c parameter (section 2.1.1), the question on the importance of static and dynamic triggering (section 2.5.2) or the more recent idea that aftershock magnitudes are correlated (section 2.3). For each of these issues reaching a consensus is complicated since contradictory results were published over the years. Probably the most important reason for this is that different studies on earthquakes are rarely done in the same conditions: the region of the earthquakes (and thus their properties), the quality of the data and the data processing methods vary from one study to another. Considering this, it is not very surprising to find different results or to make different interpretations of them, even for studies which *a priori* address the same issue.

A typical example of this is the variation of the b-value prior to great earthquakes: some authors observed an increase [33, 133]⁹ and others a decrease [91] in the b-value prior to a great event. In [133] and [91] the number of earthquake localisations studied is quite large (9 and few tens, respectively), with earthquakes coming from

⁹In [133] sometimes a decrease followed the increase of the b-value. Nevertheless, the accent of the study is put on the increase of b , and eventually its peak.

several different regions, indicating that these contradictory observations probably result from the data processing method rather than from an unfortunate coincidence.

2.6.1 The main problems

There are some problems that are regularly encountered when comparing different earthquake studies.

Working on a non-representative sample: Some results on earthquakes are difficult to generalise because they either consider data from only one local catalogue [17, 36, 75], or use a very small data set and treat only a few examples [141]. Using only one catalogue is justifiable, since it assures the uniformity of the data. Nevertheless, when all of the data comes from the same region, the results may be influenced by the typical regional characteristics that are not encountered elsewhere. The problem with small sets of data appears when the selection criteria of the data needs to be very restrictive. When only a small amount of suitable data is left, the results may only concern a few examples, and are difficult to generalise. These two problems are often combined in studies about aftershocks: often very few (as little as 2 or 3) aftershock sequences coming from the same region are considered [99, 156], sometimes even for observations that need to be universal (like the validity of a model).

Indirect measures and observations: When a study deals with variables which are not directly accessible for a measurement (or processes not suitable for a direct observation), they can only be estimated by establishing relations with other, measurable variables. This is typically the case for the differential stress (see section 2.4) and the debate on static and dynamic triggering (section 2.5.2). This process takes time and the conclusions depend (more than usual) on the interpretation of the author.

Varying recording conditions: The temporal variations in the detection quality can considerably change the output of a study. The most common detection quality problem is STA/I (section 2.2), and taking this into consideration we could identify two major problems. First, there are studies not considering STA/I [44, 86], which are hard to rely on. Then, several techniques exist on dealing with STA/I (two of them are discussed in section 3.3), but to our knowledge, there is no comparative study on the influence of these methods on the data quality.

Different data processing methods: Even common analyses about earthquakes (like power law fitting or determining a power law span), can be made in several different ways. The following section summarises some of them. For less common analysis the differences between the possible techniques can be very important. Of course, it is very delicate to compare results from studies using different data processing.

3 Methods

3.1 Data collection

We analysed earthquake data searching for subtle variations in the earthquake statistics. Due to the sensitivity and precision we needed, the quality of the data was particularly important. We decided to use local earthquake catalogues because they are usually more complete and uniform than global ones. We needed long aftershock sequences produced by strong mainshocks, so we used data from two highly active regions - Japan and California.

The Japan Meteorological Agency Catalogue **JMA**¹⁰ collects data from earthquakes in and near Japan, and recordings from 2002 to present are available. Though the quality of the detection varies according to regions, most of the time the data has quite low completeness magnitudes, sometimes getting as low as 1. We used data collected from 2002 to 2014, which corresponds to a total of about $1.7 \cdot 10^6$ events, more than $3 \cdot 10^5$ of them having magnitudes greater than 2.

The South California Seismic Network Catalogue **SCSN**¹¹ collects data from the south of California. We used recordings from 1970 to present, making a total of about $4.4 \cdot 10^5$ events, more than $1.2 \cdot 10^5$ having magnitudes ≥ 2 .

The North California Seismic Network Catalogue **NCSN**¹² has similar characteristics to SCSN, but concerns the north of California. Some of the recordings overlap regions from SCSN. It has less events than SCSN, for the same duration ($4.5 \cdot 10^4$ events with magnitudes ≥ 2).

3.1.1 Defining an earthquake sequence

Earthquakes naturally form clusters which are easy to identify visually (figure 3.4). In order to define an earthquake sequence we started by choosing a spatial earthquake cluster in a catalogue (figure 3.8.a). In the cases where the span of a cluster is not easy to define, we plotted its biggest event, and the 100 earthquakes following this event - this allows a visualisation of the aftershock zone and an easier determination of the cluster boundaries. When a polygon limiting the cluster boundaries is set, we look at the time-magnitude distribution of events within the cluster (figure 3.8.b). When a mainshock-aftershock sequence is identified, the time and magnitude of its mainshock are stored.

In some cases it was necessary to identify sequences with low number of secondary aftershocks. For these purposes sequences were inspected visually, and it was verified if they present large deviations from the Omori law.

3.2 Extracting the power law exponent

The estimation of the power law exponent is a crucial step of our study. The variations of the b-value that we will study are small, and the data in the time window of analysis poor, so we need to implement an estimation method that is as reliable and accurate as possible. On the other hand, the power-law fitting will be

¹⁰Catalogue available on the [NIED Hi-net](#) website.

¹¹SCEC (2013): Southern California Earthquake Center.

Caltech.Dataset. doi: [10.7909/C3WD3xH1](https://doi.org/10.7909/C3WD3xH1)

¹²NCECD (2014), Northern California Earthquake Data Center.

UC Berkeley Seismological Laboratory. Dataset. doi: [10.7932/NCEDC](https://doi.org/10.7932/NCEDC)

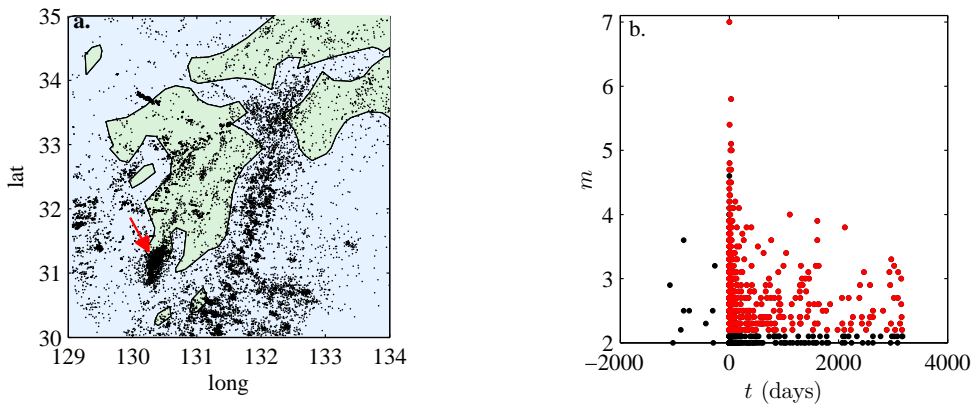


Figure 3.8: (a) Part of the Japan map, where earthquakes occurring from 01.01.2002 to 01.01.2014 are represented by black dots. The red arrow marks an identified cluster. (b) Time distribution of the events within the cluster on (a). A mainshock and its sequence can clearly be identified.

done for numerous series of different power laws and should not take more than few minutes to be done.

As will be discussed hereafter, extracting the exponent is the easy part of the procedure; the amount of published resources available on this subject is very large, but they all seem to converge toward the *maximum likelihood estimation* (MLE). The hard part is determining the span of the power law. We will often be dealing with power laws with limits on the bottom and the top of the distribution, and the estimation of β is very sensitive to the choice of these limits [8]. We will discuss few methods that were proposed for this task before choosing the one that suits our study best.

3.2.1 Estimating the exponent of a power law

One widely used method for extracting power-law exponents consists in doing a linear least square fit on a logarithmic binning histogram of the data (LSLB). Its implementation is very easy, the calculation is fast and it gives satisfactory results when the data is complete, the events are numerous and the power-law span is large. We cannot guarantee satisfying these conditions with the data that will be treated. Thus we compared the results of LSB with results from MLE. The calculation time is somewhat longer in the later case, but the estimation of the exponent is supposed to be more precise.

Maximum likelihood estimation

This method [2] consists in finding the exponent β which maximises the probability of having a certain set of values x_1, x_2, \dots, x_n . The probability, also called the *likelihood of the set* is expressed as:

$$P(\{x\}|\beta) = \prod_{i=1}^n p(x), \quad (3.9)$$

where p is the probability of a single event x occurring.

In our case we work on the distribution of the earthquakes' magnitudes. Though magnitudes are distributed following an exponential $N(m) = 10^{a-bm}$, the amplitudes

of the earthquakes, defined as $A = 10^m$, follow a power law $N(A) \propto A^{-b}$. Thus, the probability distribution function of amplitudes also follows a power law

$$p(A) = A^{\beta_A}, \text{ where } \beta_A = b + 1. \quad (3.10)$$

The procedure to determine the b-value for a set of magnitudes is the following: we convert the magnitudes to amplitudes, then calculate the exponent β_A of the power-law probability distribution of the amplitudes, and then this exponent is converted into the b-value. Hence, in the following, the set of values $\{x\}$ corresponds to the amplitudes of the data to be fitted, and the exponent β is linked to the b-value as:

$$\beta = b + 1. \quad (3.11)$$

The expression of the probability $p(x)$ depends on whether magnitudes are discrete or continuous, and whether they have a maximum or/and minimum limit. In our case, we will be dealing with discrete magnitudes (magnitudes in catalogues have a precision of 0.1 or 0.01) having both upper and lower limit. Nevertheless, we will actually use a continuous magnitude method with upper and lower limit [10], since it is much simpler to implement and faster to compute. We will implement corrections due to the fact that magnitudes are discrete [82]¹³. This leads to:

$$p(x) = \frac{-\beta + 1}{x_{max}^{-\beta+1} - x_{min}^{-\beta+1}} x^{-\beta}. \quad (3.12)$$

Finally, rather than maximizing the likelihood of the set, we will maximise its logarithm. This simplifies the calculation significantly by converting products into sums.

$$\beta = \underset{\beta}{\operatorname{argmax}} \left[\log \left(\prod_{i=1}^n p(x_i) \right) \right] = \underset{\beta}{\operatorname{argmax}} \left[\sum_{i=1}^n \log(p(x_i)) \right] \quad (3.13)$$

This equation with $p(x)$ given by 3.12 can only be solved numerically. We calculate this expression for values of β within an interval of typical values (usually from 1 to 3) with a step of $2 \cdot 10^{-4}$. The estimated β is the one maximizing $\log(P(\{x\}|\beta))$, and its uncertainty is given by the standard error of $P(\{x\}|\beta)$.

We tested the fitting method on some synthetic sets of power-law distributed data. We observed that MLE and LS LB result in the similar estimations for the exponent, but the error on the estimation was systematically at least twice as small for MLE (see the results for a series of 500 events fitted with both methods on figure 3.9).

¹³The main problem with the use of discrete data is that it is binned and this leads to define incorrect limits for the power-law span [82]. In the particular case of our catalogues, magnitudes are recorded with a precision δm of 0.1 or 0.01. As a result, working with earthquakes with magnitude m actually means that we use all the earthquakes such as $m - \frac{\delta m}{2} \leq m < m + \frac{\delta m}{2}$. Thus, if we limit the MLE to catalogue magnitudes such as $m_{min} \leq m \leq m_{max}$, the real magnitude limits are $m_{min} - \frac{\delta m}{2} \leq m \leq m_{max} + \frac{\delta m}{2}$. This problem is simply corrected by fixing the "real" limits of the power law span.

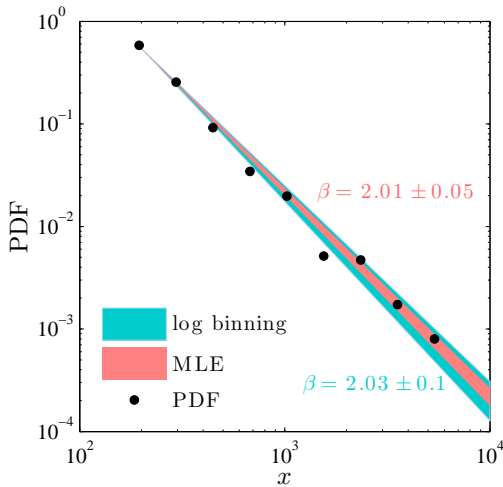


Figure 3.9: Estimation of β for 500 simulated events using LSLB or MLE.

3.2.2 Determining the power-law span

For earthquakes, the magnitude above which the detection is complete i.e. the *completeness magnitude* (M_c) is a very important parameter. Several different methods have been proposed, criticised, defended and corrected in the past few decades [18, 21, 31, 115, 152] trying to get its most accurate estimation. Most of them are based on an inspection of the power law quality or of the stability of its exponent. They result in similar estimations and differ mostly by the amount of calculation (and thus the computing time) they need. For high quality data especially, any method can give satisfactory results, which is probably why there is still no consensus on this question. What we need is a method of determining a lower *and* a higher limit of the power law, so we need to choose one of these methods and adapt it.

The choice of the M_c estimation method is imposed from the characteristics of the data we are dealing with. First of all, we know that we need a method that is adaptable to an upper threshold calculation. Thus we need an algorithm more sensitive to change than the maximum curvature method¹⁴ [152]. Also, some of the distributions to analyse will present double power-laws, so we cannot use methods based on b-value stability [18]. We intend to analyse a lot of simulated and experimental aftershock sequences, and each one will need few dozens of fittings, so the method needs to be quite fast, not longer than few minutes. All algorithms that calculate the plausibility of the data following a power law by repeating Kolmogorov-Smirnov test¹⁵ on hundreds of simulated data sets [21, 31] are too time-demanding for our case. Ruling out most of the existing methods, this left us with only one option satisfying all the criteria we have.

Wiemer and Wyss method

The method we chose to work with is the one introduced by Wiemer and Wyss [152], to which we added some modifications. It is fast enough, but does include a

¹⁴The maximum curvature method determines the completeness magnitude as the point of maximum curvature on the curve representing the logarithm of the distribution of magnitudes.

¹⁵The Kolmogorov-Smirnov test is a way of comparing a data set with a synthetic data set that follows a presumed probability distribution. It consists in calculating the maximum distance between the cumulative distribution function of the experimental data and the synthetic data.

goodness-of-fit test. Also one of its steps consists in binning the magnitudes, so it is particularly adapted to discrete data. Initially it was conceived for calculating a minimum threshold magnitude, but it is easily adaptable for calculating a maximum threshold too. The original procedure is the following:

- Make the values of the lower threshold M_l vary, starting from the lowest magnitude and incrementing progressively.
- For each set of magnitudes separate the data into magnitude bins. Count the number of events in each bin S_i^{exp} .
- For each set of magnitudes calculate the parameters of the power law using MLE. Calculate S_i^{fit} , the number of events in each bin for the synthetic power law.
- Calculate the goodness-of-fit, which is basically the normalised difference between the number of events in the experimental data and the fitted case:

$$r(M_l) = 1 - \Delta r = 1 - \frac{\sum_{i=1}^{n_{bins}} |S_i^{exp} - S_i^{fit}|}{\sum_{i=1}^{n_{bins}} S_i^{exp}} \quad (3.14)$$

Δr is an estimation of the fraction of events that can not be described by the power law.

- Calculate M_c as the lowest M_l satisfying $r(M_l) > r_{trsh}$. The threshold r_{trsh} corresponds to the fraction of events we want to be represented by a power law, and is usually fixed to values close to 0.9

Adaptation for a power-law span determination

This method can be easily adapted to the case where we want to define the lowest and the highest magnitude limits of a power law. We introduce an upper magnitude threshold, M_u , and do the same procedure as previously for magnitudes within $[M_l, M_h]$. We make M_l and M_h vary, and look for $r(M_l, M_u) > r_{trsh}$. The result of this calculation can be observed on goodness-of fit maps (figure 3.10).

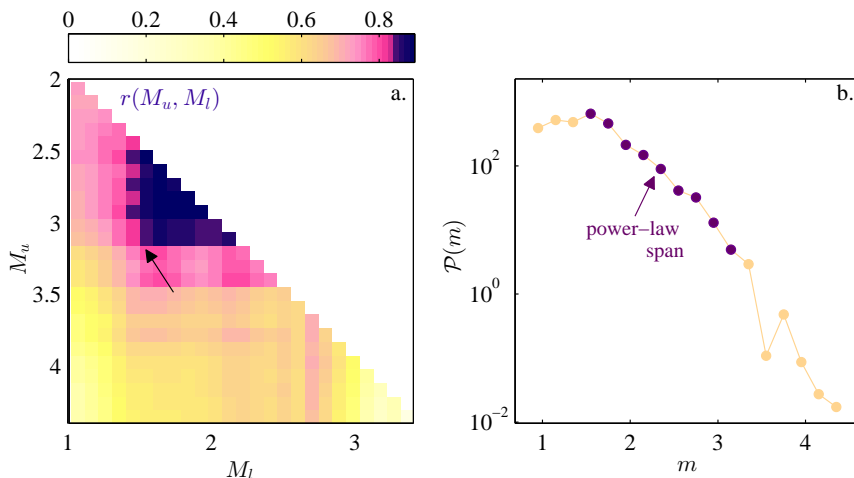


Figure 3.10: (a) Map of the goodness-of-fit for the magnitudes of a set of 500 consecutive earthquakes in Japan. The arrow points on the chosen $\{M_l, M_u\}$ pair. (b) Probability distribution of the same magnitude set, and the determined power law span (dark circles).

The only difference with the case $M_u = \infty$ is that for finite M_u we usually find several intervals $[M_l, M_u]$ satisfying the condition $r(M_l, M_u) > r_{trsh}$. In this case, we are free to define a criteria to choose definitely the lower and upper limits, like searching for the longest interval (as in figure 3.10), or the interval containing the most events.

Corrections to the Wiemer and Wyss method

In the particular case of discrete power laws limited by an upper and lower limit, the original Wiemer and Wyss method needs to be implemented taking some precautions and adding some corrections.

The magnitudes we work with are discrete with a precision δm . In practice this means that the magnitudes are already binned, in bins with length δm (which we will call “original bins”). The best choice for any further binning are bins with lengths that are multiples of δm . Otherwise the number of original bins within each new bin will not be constant, resulting in the number of events being artificially increased in some, and decreased in other bins. This would engenders a noisy histogram and a low goodness-of-fit value.

Wiemer and Wyss have not discussed the dependence of the goodness-of-fit coefficient on the number of events used for the calculation. The deviation from the power law Δr scales as \sqrt{N} ; hence if the number of events is small, the calculated value of r will be low. Since we work with power laws, the number of events decreases rapidly as M_l increases. Therefore, r is systematically smaller for high magnitudes. While this is statistically correct and does not have much influence when only a lower limit is calculated, it becomes a problem when lower and upper limits are required. The original method systematically prefers $\{M_l, M_u\}$ intervals with lower limits. For an example, see figure 3.11. On 3.11.a, we represented the mean value of r for a synthetic power law with 20000 events (the mean value was calculated over 100 realizations). r drops rapidly when the lower limit of the set M_l increases, even though the power law was simulated. This is particularly problematic in the case of double power-laws, where the detection of the first one will be preferred. To over-

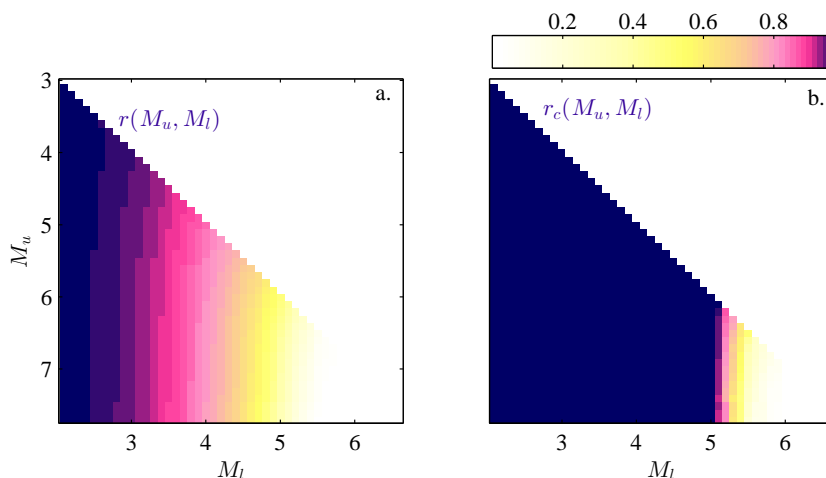


Figure 3.11: Goodness-of-fit for a simulated power law distribution. (a) r , the Wiemer and Wyss goodness-of-fit. (b) r_c , the corrected goodness-of-fit coefficient (according to equation 3.15)

come this problem, the calculation of $r(M_l, M_u)$ should include some renormalisation with respect to the interval containing the greatest number of events:

$$r_c(M_l, M_u) = 1 - \Delta r \frac{\sqrt{N_{max}}}{\sqrt{N(M_l, M_u)}} \quad (3.15)$$

The corrected data is represented on figure 3.11.b. Apart from the estimations on very short power law spans (bottom right), the goodness-of-fit is constant across the different $[M_l, M_h]$ pairs.

3.3 Dealing with STAI

We saw that the incomplete detection of small aftershocks after a great mainshock can influence the estimation of the Omori law c-value and of the b-value of an aftershock sequence. It is thus very important to avoid working with incomplete data. There are two ways of avoiding the effect of STAI. One consists in excluding the very beginning of a sequence, since this is the part concerned by STAI [53, 74]. The second one consists in excluding pairs of events which are too close in time (less than 30 seconds [156], or 2 minutes [28] apart). The idea is to omit events which are in a configuration where STAI might have occurred if the second event was smaller.

When using the second method one needs to arbitrarily impose a constant time corresponding to the detection dead-time provoked by a major earthquake. In reality this dead time depends on the earthquake magnitude (the greater it is, the longer will be its coda), and it is hard to determine it precisely. On figure 3.5 the period of non-detection of earthquakes after the mainshock lasts about 230 s, but omitting all pairs of earthquakes occurring at less than 4 minutes from each-other will induce a considerable loss of events. Also, this method favours the suppression of events which are supposed to be correlated. Thus, it seems more appropriate to deal with STAI using the first method: we simply will not use the data occurring at the beginning of the sequence. We define a minimum time and a minimum magnitude above which the detection is complete. To do this, we use a technique which starts by visually identifying the $\{t_{min}, M_c\}$ pair. Then M_c is recalculated using Wiemer and Wyss method for the completeness magnitude, and finally t_{min} is recalculated as the the c-value of the Omori law, given the completeness magnitude M_c .

3.4 Simulations

The Branching Aftershock Sequence Model

The experimental results will be compared with results for aftershock sequences simulated with the Branching Aftershock Sequence (BASS) model [142]. It is a point process model, meaning that we will model earthquakes as punctual events, characterised by their time and magnitude (earthquakes' positions are not relevant for our study), without considering the details of each earthquake. Basically, BASS is a way of generating power laws similar to earthquakes. It is based on another model, the Epidemic-Type Aftershock Sequence (ETAS) model [51, 94], BASS being the self-similar limit of the former.

The idea is to generate sequences of punctual events following the Gutenberg-Richter, Omori and Båth laws. We will generate data corresponding to the type of configuration that we will study, i.e. one single mainshock-aftershock sequence,

with a strong mainshock. We start by fixing a large value for an earthquakes magnitude (in general larger than 7) and a time $t = 0$. This defines the mainshock. Then we generate the first generation of aftershocks. According to the modified Båth law 3.8, the mainshock will generate n_{as} aftershocks, where n_{as} is given by:

$$n_{as} = 10^{b(m_{ms} - \Delta m - m_{min})}, \quad (3.16)$$

with m_{ms} the mainshock magnitude, Δm is the magnitude difference between the mainshock and its biggest aftershock (as defined in section 2.1.3) and m_{min} the minimal magnitude that can be generated in the simulation¹⁶. These aftershocks should obey the Gutenberg-Richter law and the Omori law, according to which the cumulative distributions of the aftershocks' magnitudes and times are:

$$N(m) = 10^{-b(m - m_{min})} \quad (3.17)$$

$$N(t) = (t + c)^{-p+1} \quad (3.18)$$

To define an aftershock we generate a random number from the interval $[0, 1]$, we substitute it for the value of $N(m)$ or $N(t)$ in equations 3.17 and 3.18, and deduce the value of m or t . The n_{as} aftershocks are generated this way.

When an aftershock is large enough, it can generate its own aftershocks. So we repeat the previous step, only considering the first generation of aftershocks as mainshocks, and we generate a second generation of aftershocks following the same procedure. This operation can be repeated a finite number of times, or until aftershocks get very small and no further aftershock triggering can exist.

¹⁶The number of aftershocks generated by a mainshock is the only difference between the ETAS and the BASS model from the point of view of simulations.

CHAPTER 4.

B-VALUE AND THE FREQUENCY OF ANALYSIS

1	Motivations	76
2	First observations on simulations	77
2.1	The origin of the power law crossover	78
3	What does b_I depend on?	
	A numerical study	82
3.1	Results	83
4	Comparison with the experimental data	86
5	Magnitude correlation	88
5.1	Magnitude correlations in the case of one-generation simulated sequences	
	The effect on the b-value decrease	88
5.2	b-value variation of real aftershock sequences	88
6	Conclusion and perspectives	89

1 Motivations

In the case of experiments on paper fracture, observing the variation of the energy power law exponent with the frequency of analysis (f_a) proved to be a powerful tool for detecting time correlations in discrete processes. Because of the existence of aftershocks in the fracture propagation, a decrease in f_a provoked a decrease of the calculated exponent of the energy distribution. We took this study further by applying the same data treatment on a different system: real earthquake aftershock sequences. Indeed, aftershock sequences present a succession of events strongly correlated in time (an example of autocorrelation of the signal associated to one sequences is shown in figure 4.1), therefore, by analogy with the paper fracture experiments, some effect should be observed when f_a varies.

Earthquakes and our creep fracture of paper both present aftershocks, but their nature is different. For the paper experiments only some of the major fracture events had aftershocks, but most of the events were uncorrelated. For large earthquake sequences the number of aftershocks is bigger (hundreds or even thousands per mainshock) and almost the whole sequence is temporally correlated, so we do not expect the two systems to show identical behaviours.

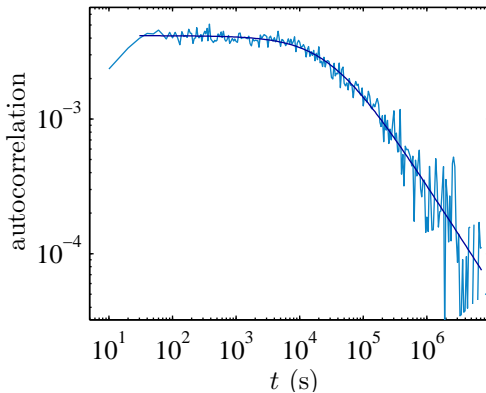


Figure 4.1: Autocorrelation of the time-magnitude signal of the aftershock sequence of the 2005 Fukuoka earthquake.

One of our objectives was to characterise the changes that occur in the distribution of magnitudes when the frequency of analysis is lowered. We wanted to study the nature of these changes, the typical frequency of analysis at which they occur, and how they depend on the aftershock sequence characteristics (Omori law parameters, b-value, productivity). We also wondered if the eventual existence of magnitude correlations (see section 2.3 in chapter 3) would have an effect on the results.

The main motivation for this study was our own experience with paper fracture where low frequency measurements were not reliable for characterising the energy distribution of the fracture events. Our goal is to understand better how the energy distribution changes when the recording frequency of an experiment is too low. This could allow for the analysis to be done the other way round: deduce the original exponent of the power law using a low-frequency measure, which could be useful when a high frequency measure cannot be done.

2 First observations on simulations

We start by using simulated aftershock sequences - this allows us to control the properties of the sequences, and to generate as much events as needed. We used the BASS model (section 3.4, chapter 3) to simulate earthquakes. We are interested in sequences of strong mainshocks where the number of secondary aftershocks is negligible compared to the primary ones. Thus, for now we only produce one generation of aftershocks, perfectly following the Omori law. The duration of each sequence is limited to 10^7 numerical time steps (which can be considered equivalent to seconds) and contains 5000 events. We chose typical parameters for the Omori law and the Gutenberg-Richter law exponents: $p = 1.2$, $b = 1$. A total of 200 sequences were added up in time, each one following the previous one. Then this signal was integrated over time windows of length w , like in section 3.4 of chapter 1: the energies of the earthquakes were summed up¹, and the mean time of the events in each window was calculated. The maximum value of w was 10^5 , so the minimum number of integrated events is around 100. Thus we obtain a new signal, with a frequency $f_a = \frac{1}{w}$. The magnitude of this new signal will be denoted² \underline{m} .

Our first simulations show that, for some values of w , the distribution of \underline{m} presents a crossover between two power laws. Figure 4.2.a shows the probability distribution of magnitudes of the signals integrated over different time windows, and the change of the exponent is visible. Note that to ease the visualisation, the probability is not normalised but multiplied by a constant which makes each curve start from 10^0 . To check that there really are two different power laws, each with a constant exponent, we calculated the exponent of the longest power law (actually the most probable

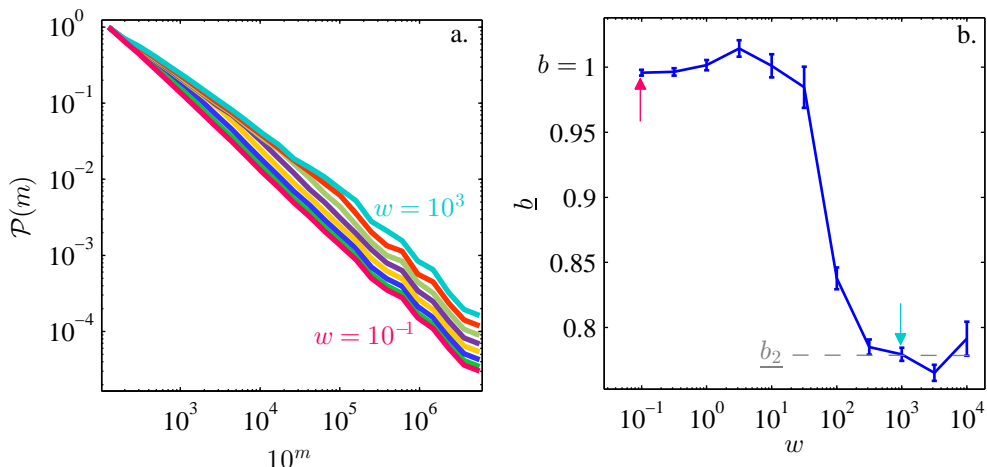


Figure 4.2: (a) Cumulative probability distribution of the magnitudes of simulated aftershock sequences ($p = 1.2$, $b = 1$, $c = 100$, $n_{as} = 5000$), for different integration windows w . A crossover between two power laws can be seen. (b) Exponent of the longest power law in the distribution. The arrows indicate the result from the lowest and the highest curves on figure (a).

¹Notice that we sum up energies rather than magnitudes or amplitudes. This means that magnitudes are transformed in energies first, energies are summed-up within the integration windows, and the newly obtained energies are transformed into magnitudes.

²In order to avoid confusion all variables related to the integrated, low-frequency signal will be underlined.

power law, using the method from section 3.2.2, chapter 3 which occurs to be the longest one too). The result is represented in figure 4.2.b, where one can see that for small integration times the initial power law is valid ($b = 1$), while for large w the second power law becomes longer than the initial one and dictates the exponent estimation.

This observation is in accordance with results on simulated creep fracture of fibre bundles [26], where a crossover between two power laws appearing with the decrease of f_a has already been observed. The statistics of the system are very similar to ours, since the fracture bursts follow the Gutenberg-Richter law and an inverse Omori law.

Remarks

Hereafter, in order to avoid confusion we will denote b the b-value of the original (non integrated) aftershock sequence, and b_I the b-value corresponding to the second power law, resulting from the integrating process. The non-integrated earthquake sequence will systematically be referred to as the *original* sequence (or signal). Also, we will alternatively talk of an increase of the integration window w or decrease of the frequency of analysis f_a , since they both represent the same process.

A choice needs to be made regarding the representation of the magnitude distribution. We will systematically plot the distribution of the amplitudes (10^m) rather than magnitudes, in order to represent a power law and not have confusion between power-law and exponential distributions. We represent a probability integrated over the histogram bins (i.e. we do not normalise by the bins length), in order to represent a power-law with an exponent b (normalising by the bins length would result in plotting the non-cumulative probability distribution, which has an exponent $b+1$). This probability will be denoted \mathcal{P} .

2.1 The origin of the power law crossover

The fact that a new power law emerges when the signal is integrated over finite time windows is not trivial. For the paper fracture experiments we saw that the exponent of the energy distribution does not decrease with the frequency of analysis when magnitudes are uncorrelated. For the earthquake simulations the magnitudes of the earthquakes are completely independent from each other, and a decrease of the b-value is still observed. We will try to provide a qualitative explanation of the phenomenon.

First, let us look at the probability distribution of non integrated and integrated magnitudes, for a simulation with typical earthquake parameters ($b = 1$, $p = 1.2$), and an integration window $w = 316$ (figure 4.3.a). The distribution of high magnitudes does not seem affected by the integration process (note that the distribution is not normalised, and the curves collapse). Low magnitudes follow a new power law with a lower exponent. The two power laws meet in a crossover zone (dashed line) where neither of the power laws could be fitted. We will try to explain the origin of the crossover and calculate its position.

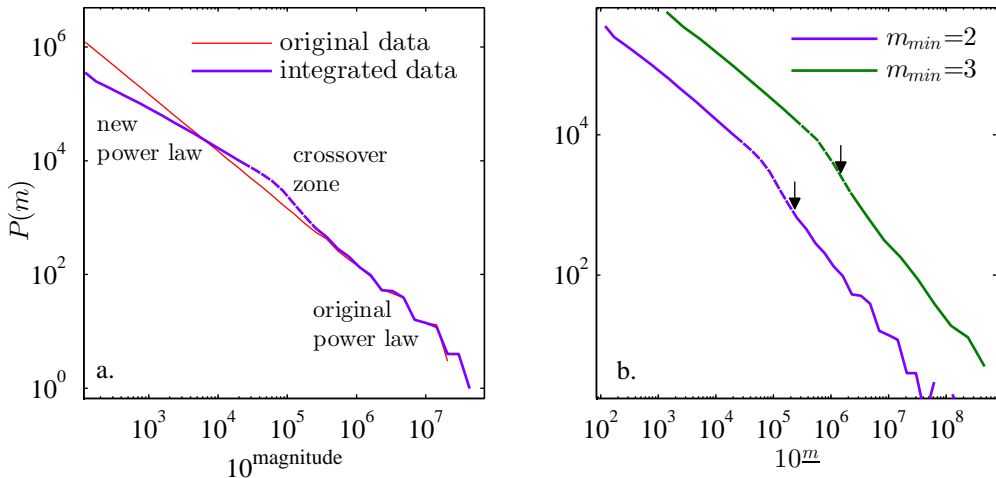


Figure 4.3: (a) Non normalised probability distribution of the magnitudes of the original (red) and integrated (violet) events. (b) Probability distribution of m for two simulations with the parameters: $b = 1$, $p = 1.2$, $n_{as} = 20000$, $c = 1000$, $w = 316$, $m_{min} = 2$ (violet - same as in (a)) or $m_{min} = 3$ (green).

In order to perturb the probability distribution for a given magnitude m , the integrating procedure needs to be able to significantly affect it. Let us consider a great event of magnitude M and energy³ $E = 10^{1.5M}$. Perturbing its distribution is possible if the integration process can result in creating another event with the same magnitude⁴. Since our integrating process consists in integrating energies, this means that we need to sum-up the energies of n_I events, where

$$n_I = \frac{E}{\langle e \rangle}, \quad (4.1)$$

and $\langle e \rangle = \langle 10^{1.5m_i} \rangle$ is the mean energy of the distribution. For an aftershock sequence with $b = 1$ and magnitudes verifying $2 \leq m \leq 6$ the energies are distributed following $\beta = 5/3$ and $10^3 \leq e \leq 10^9$. The mean energy is given by:

$$\langle e \rangle = \frac{-\beta + 1}{-\beta + 2} \cdot \frac{e_{max}^{-\beta+2} - e_{min}^{-\beta+2}}{e_{max}^{-\beta+1} - e_{min}^{-\beta+1}} \quad (4.2)$$

and in this case $\langle e \rangle = 1.12 \cdot 10^6$. Hence, according to equation 4.1, perturbing the distribution of events with magnitude $M = 5$ needs an integration window w where at least 25 events are summed up, and for $M = 6$ n_I goes up to ~ 800 .

³The energy of an earthquake is exactly calculated as $E = C10^{1.5M}$ ergs, where M is its moment magnitude and $C = 10^{11.8}$. In this section we are only interested in the relative energies of earthquakes so we lose the constant C and the unit for commodity. It is as if all the energies are given with respect to the energy of an earthquake with magnitude $\frac{2}{3}$.

⁴In practice, this means that an event with energy E can be created out of smaller events, or that during the integration process the energy of the great event can be doubled.

This explains why the original power-law of the magnitudes stays valid until very large w are applied. The end of the crossover zone should correspond to the magnitudes which are not perturbed by the integration (in this case the equation corresponds to the highest magnitude event perturbed by the integration):

$$\frac{1}{1.5} \log_{10}(n_I^{\max} \langle e \rangle), \quad (4.3)$$

where $n_I^{\max} = \int_{t_0}^{t_0+w} \rho(t) dt$ is the maximum number of original events that can be integrated into one new event (ρ being the Omori law's probability distribution, and t_0 the time of the first aftershock). The calculated crossover magnitude of the distribution we are concerned with here is represented on 4.3.b) with an arrow. The calculation was repeated for a distribution with $m_{\min} = 3$. In both cases m_{CO} seems to correspond to the end of the crossover zone.

The small magnitudes follow a power law with a lower exponent. Comparing the non-normalised distributions on 4.3.a, one can see that the decrease of the exponent is due to a loss of small events, which is quite obvious, since small energy events are lost during the integration process. We still do not know exactly why small magnitudes follow a power law (rather than any other distribution). Our analysis showed that the Omori law distribution of times is crucial for the formation of this second power law. In the next section we will compare the effects of the integration process on sequences with power-law distributed times and uniformly distributed times. We will see that the power law time distribution is crucial for the formation of the low-exponent power law.

2.1.1 The role of the Omori law

We will integrate the signal corresponding to two different sequences: one where the occurrence times of the events follow a power law with $p = 1.5$, and another one where times are uniformly distributed (which is equivalent to $p = 0$). We will be interested into the number of events integrated within one window w , which will be denoted n_I . We want to know how is n_I distributed.

We will start by considering the sequence with uniformly distributed times. Figure 4.4.a represents a histogram of n_I for this case, with $w = 10^5$. n_I is distributed following a Gaussian with a mean value ~ 4 , and n_I^{\max} is around 15. This was expected: since the events are uniformly distributed in time, n_I has a mean value determined by the total number of aftershocks n_{as} , the duration of the sequences t_{max} and the duration of the integration window w , so

$$\langle n \rangle = \frac{w}{t_{max}} n_{as}.$$

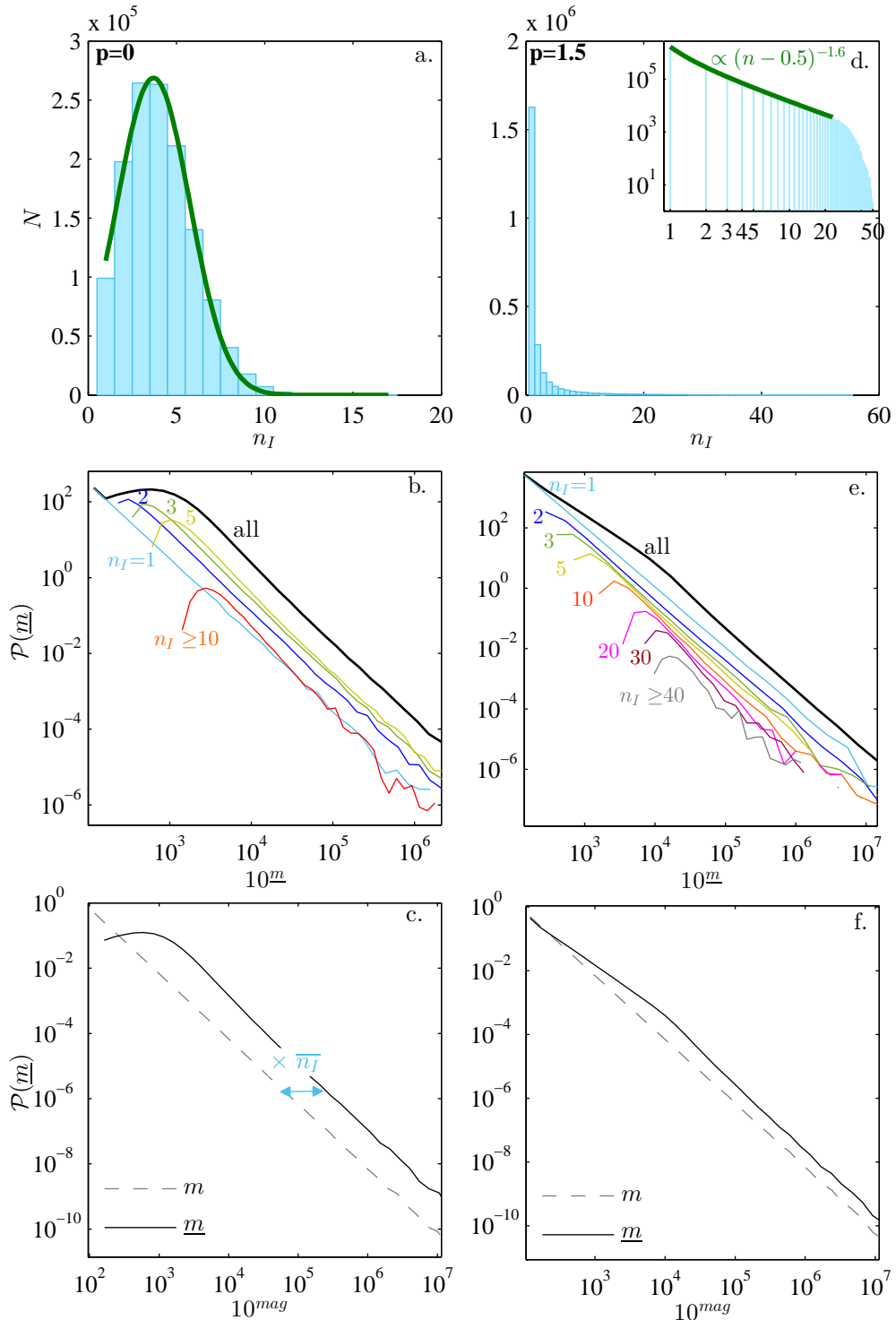


Figure 4.4: (a) Histogram of the number of original events per integration window in the case of uniform time distribution. (b) Probability distributions of integrated magnitudes \underline{m} of events with fixed number of original events (coloured lines), and of all the integrated events (black line). (c) Normalised probability distribution of the original magnitudes (gray dashed line), and the integrated magnitudes (black line). (d-f) same as a-c, for events with power-law distributed times.

(a-c) : $b = 1$, $p = 0$, $t_{max} = 5 \cdot 10^8$, $t_{min} = 100$, $n_{as} = 2 \cdot 10^4$, $w = 10^5$
 (d-f) : $b = 1$, $p = 1.5$, $t_{max} = 5 \cdot 10^8$, $t_{min} = 100$, $n_{as} = 2 \cdot 10^4$, $w = 316$

Figure 4.4.b shows the non-normalised probability distribution of magnitudes of integrated events with fixed n_I . They all follow a power law with an exponent $b = 1$, starting at different magnitudes. The sum of all these power laws constitutes the distribution of \underline{m} , which is also a power-law saturating for low \underline{m} . The power laws of the normalised distributions of the original events magnitudes m and the integrated ones \underline{m} differ only by a multiplicative factor (figure 4.4.c), corresponding to $\overline{n_I}$.

Now, let us consider a signal with power-law distributed times. This signal is integrated over windows with constant length. Because of the power-law distribution of times, the windows at the beginning of the signal will contain a very large number of events. At the end of the signal the events are very far from each-other, and most of them are the unique event of their window ($n_I = 1$). A histogram of the number of events per window n_I is shown in figure 4.4.d. One can see that the number of intervals containing n_I events (which we will call N) drops rapidly with n_I . The inset shows that it can be approximated by a power law $(n_I - \frac{1}{2})^{-1.6}$, followed by a cut-off. The probability distribution of the magnitudes of the integrated signal \underline{m} at fixed n_I all follow power laws (figure 4.4.e.); as n_I increases the starting magnitude of the power law increases too, and the total number of events in the distribution decreases. It is the sum of all these power laws with delayed starts that results in the new power law with exponent b_I . Thus, the way the original events are distributed in the integration windows is crucial for obtaining the low-exponent power law. Figures 4.4.c and 4.4.f show the difference in the result obtained for uniform and power-law distributed occurrence times of earthquakes.

3 What does b_I depend on? A numerical study

An aftershock sequence is characterised by few parameters concerning its temporal dynamic or energy distribution. We still do not know how the variation of these parameters affects the $\beta(w)$ curve. Therefore we studied the difference $\Delta b = b - b_I$ while varying four parameters:

- b , the exponent of the Gutenberg-Richter law
- p , the exponent of the Omori law
- c , the dead time of the Omori law
- n_{as} , the number of aftershock in 10^7 time units (productivity of the sequence).

We made these parameters vary, generating 50 realisations of aftershock sequences for each set of parameters. The exponent of the longest power law was then calculated as a function of the integration window.

3.1 Results

3.1.1 The importance of temporal correlations

Our simulations confirm that temporal correlations between aftershocks are at the origin of the power law crossover. As we see in figure 4.5.a, when $p = 0$ (uniform distribution of the aftershock times), the original power law stays valid even for large integration windows (there is no brutal drop of the b-value on figure 4.5.a, for $p = 0$). This is also true for $p = 0.4$, within the range of integration windows we work with. A much longer simulation with larger w is needed in order to observe the second power law. Then, as p increases, b_I becomes lower and lower, and the crossover time becomes shorter too; the further we get from a uniform distribution (i.e. the more p increases), the greater will be the gap between the two power laws. This means that for low frequency measurements, the estimation of the exponent of

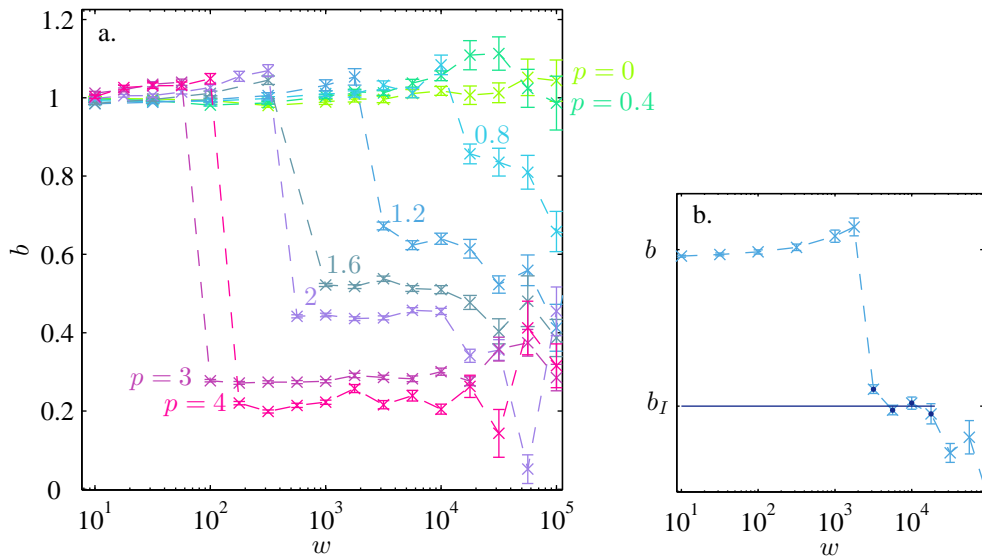


Figure 4.5: (a) Variation of the exponent of the longest power law in the distribution of earthquake magnitudes, for increasing integration window w , and for different values of the Omori law exponent p . $b = 1$, $n_{as} = 2 \cdot 10^4$, $c = 10^5$. (b) Determination of b_I for $p = 1.2$ (other parameters same as in (a)). The mean value is calculated over the points marked with dark blue dots.

the Gutenberg-Richter law depends on the exponent of the Omori law.

Figure 4.5.b illustrates the calculation of b_I . When w decreases, at some point the exponent drops from b to b_I . It stays more-or-less constant during further increase of w , until the fitting technique starts presenting systematic lowering bias because of the lack of statistics. We calculate the mean value of only the stable values of $b(w)$, to estimate the value of b_I . With this method, a value b_I can be determined for each simulated aftershock sequence.

3.1.2 The influence of other parameters

$\Delta b = b - b_I$ was estimated for different sets of parameters $\{b, p, c, n_{as}\}$, always keeping three of them constant and making the fourth one vary. The values of the constant parameters are $b = 1$, $p = 1.2$, $c = 10^4$, $n_{as} = 2 \cdot 10^5$. Some of the varying

parameters have unrealistic values (like $p \geq 2$) which were chosen on purpose, in order to emphasise the effect they have.

We observe that Δb decreases significantly ($|\Delta b|$ increases) when the exponent of the Gutenberg-Richter law b (figure 4.6.a) or of the Omori law p (figure 4.6.c) increase. This means that the difference between the initial and the final distribution of energies intensifies if the distributions of energies and power laws are steeper. On the other hand, Δb does not seem to have a notable variation with the dead time c (4.6.b) nor with the total number of aftershocks per sequence⁵ n_{as} (4.6.d).

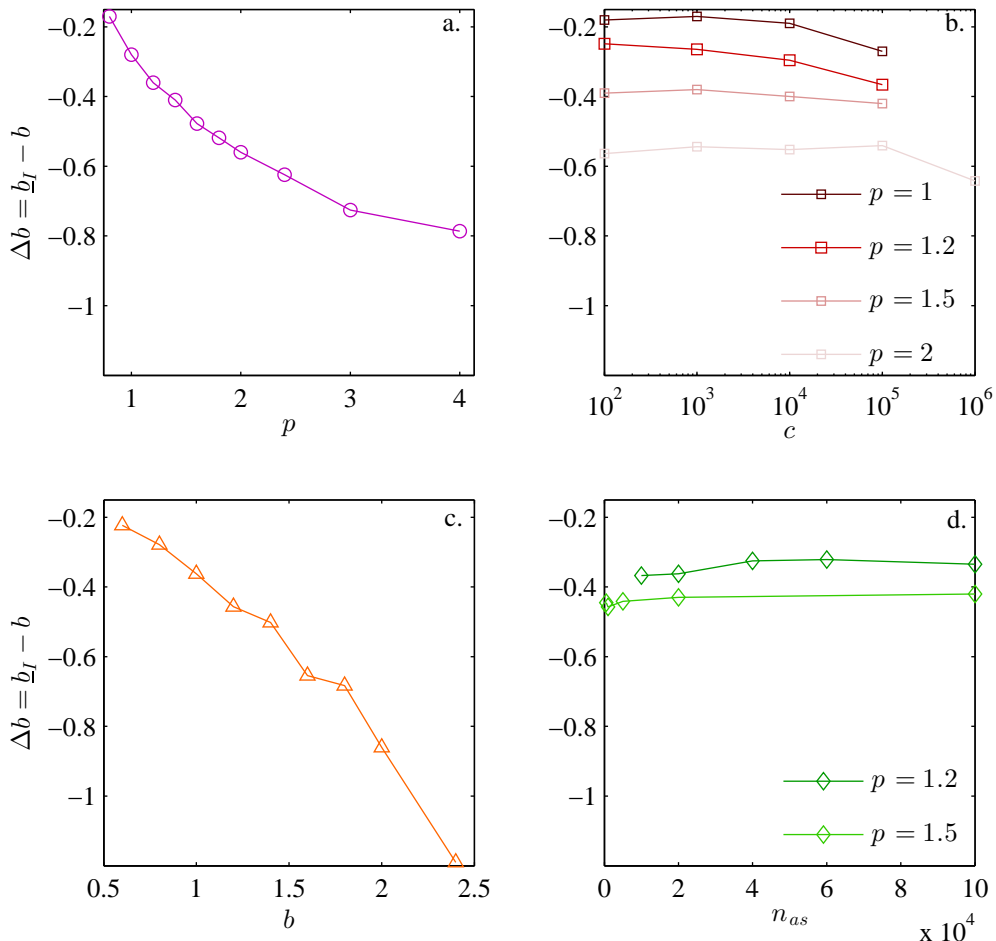


Figure 4.6: Variation of Δb regarding (a) the initial magnitude distribution exponent, (b) the Omori law exponent, (c) the Omori law dead time, (d) number of aftershocks per sequence

3.1.3 Linking b_I to b and p

Since the only two parameters determining Δb are the initial exponent of the Gutenberg-Richter law b and the exponent of the Omori law p , we studied the influence of these two parameters on b_I .

We launched BASS simulations for sequences containing 5000 events with $c = 10^4$. p varied from 0.4 to 3, b varied from 0.6 to 2. For each $\{b, p\}$ set we did 50 realisations.

⁵When n_{as} increases, the drop from b to b_I occurs for smaller integration windows, but the exponent of the power law stays the same.

For low values of p and b (≤ 0.8) 100 realisations were done, because the results were noisier.

Figure 4.7 shows the results of these simulations. On figure 4.7.a we represent the difference between the two energy exponents Δb regarding p , while keeping b constant. A significant decrease of Δb with p is observed. On figure 4.7.b Δb is represented as a function of b , for constant p values, where a decrease is also obvious.

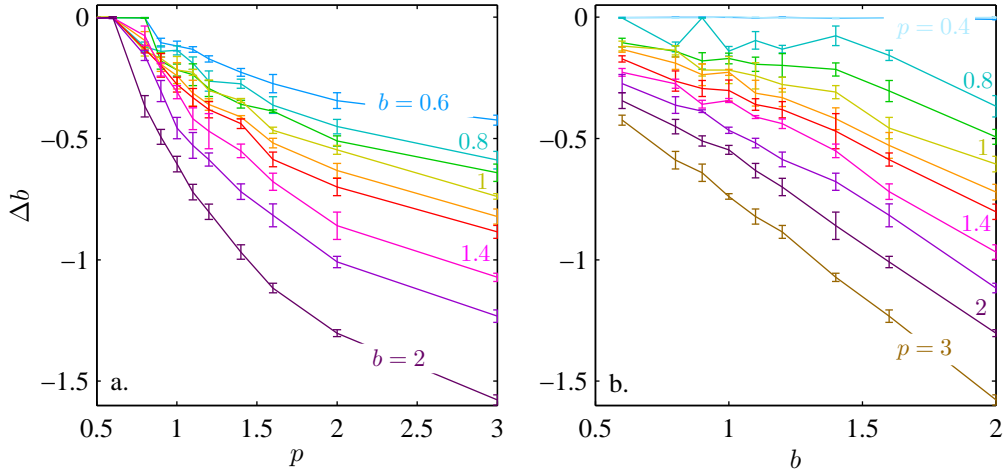


Figure 4.7: Variation of Δb regarding: (a) the exponent of the Omori law, keeping the exponent of the Gutenberg-Richter law constant or (b) the exponent of the Gutebert-Richter law, keeping the exponent of the Omori law constant.

The $\Delta b = f(p)$ curves seem to correspond to a logarithmic decrease. Each one of them was fitted with the equation $\Delta b = a \ln(p/p_0)$. Then, we studied the variation of these two parameters (a and p_0) with the value of b they were obtained for. We find that

$$a = (0.5 \pm 0.03) \cdot b - (0.02 \pm 0.03) \quad (4.4)$$

and

$$p_0 = (0.7 \pm 0.02) - (0.07 \pm 0.01) \cdot b \quad (4.5)$$

We can hence relate the original Gutenberg-Richter exponent b and the integrated signal Gutenberg-Richter exponent b_I , if the exponent of the Omori law p is known, by the equation $b_I = b + \Delta b$, where

$$\Delta b = \frac{1}{2} b \ln \left(\frac{p}{0.7 - 0.07b} \right) \quad (4.6)$$

The result of this relation is compared with the results from the simulations in figure 4.8.

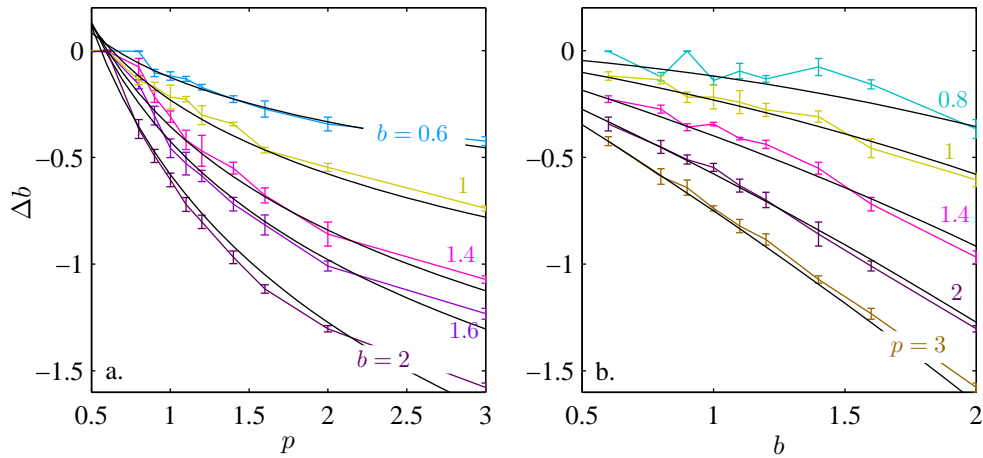


Figure 4.8: Variation of Δb regarding (a) p and (b) b . The coloured lines represent results from the simulation and the black represent equation 4.6.

4 Comparison with the experimental data

We would like to compare the simulation results with experimental data from earthquakes. We calculated the variation of \underline{b} with the length of the integration window for the earthquake sequences from the seismic data from Japan and California catalogues. Earthquake sequences contain few hundreds, or few thousands events in the best case. Integrating the signal of each sequence results in a much smaller number of events, and thus a very noisy power law. The incertitude on the calculated b -value is sometimes so large that any interpretation would be impossible. We decided, when it was possible, to group together sequences with similar statistics (similar p and b) like we did for the simulations, by making them follow each other in time. We put together only sequences whose p and b values differ by no more than 0.2.

Even when several sequences are studied together, the number of earthquakes is not high enough to clearly observe the coexistence of two power laws, like we did in figures 4.2.a. and 4.3. The number of events extracted from the catalogues is much smaller than the number of events we generated for the simulations (less than 10,000 events for a parameter set $\{b, p\}$ for the catalogue earthquake sequences, and at least 250,000 for the simulated ones), so fine measurements of the value of w for which the exponent change occurs can not be made. Still, the fact that the exponent \underline{b} decreases when w increases can be observed, and b_I can be measured.

Figure 4.9.a shows the Δb values obtained for the JMA catalogue, for sequences with $b = 0.9 \pm 0.1$ and different values of p . The results match quite well with results from the simulations. Figure 4.9.b shows the same kind of results for California catalogues. For the experimental seismic data (plain black markers) Δb is lower than for simulations (plain orange line), and the difference goes beyond errorbars. Lists of the sequences used for calculating each point are available in appendix D.

The difference between simulations and real earthquakes in California may result from secondary aftershocks and swarms that were not detected, or we did not consider strong enough to rule-out the sequence. During the selection of the aftershock sequences many of the California sequences were exempted because of the existence

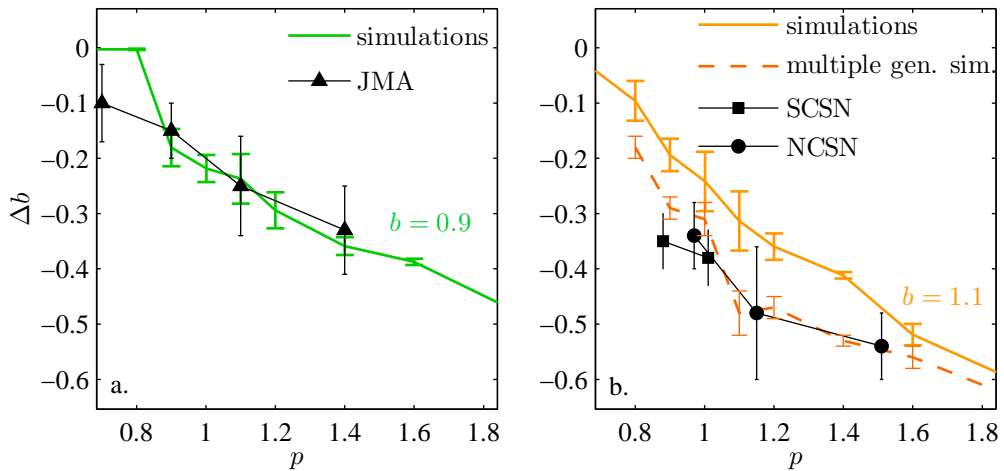


Figure 4.9: Comparison of the value of Δb for sequences from earthquake catalogues (from (a) Japan and (b) California) and simulations.

of great sequences of secondary aftershocks, swarms (figure 4.10), or the occurrence of another major earthquake very soon after the mainshock. Nevertheless, detecting secondary aftershocks is not obvious during visual inspection, or even when examining the variation of the Omori law: most of them occur at the beginning of the aftershock sequence, when the activity is very high, and an increase of few, or few tens of earthquakes can pass without being noticed. It is thus possible that the sequences we used contain a significant fraction of secondary aftershocks, which alter their behaviour.

We did a new series of simulations, corresponding to the parameters of the data from the California catalogues, and containing 5 generations of aftershocks. The number of aftershocks generated by each earthquake was calculated using the modified Båth law (section 2.1.3, chapter 3) with $\Delta m = 1.2$. Figure 4.9.b shows that there is a clear difference in the value of Δb when comparing one-generation and multiple-generation aftershock sequences. Experimental values of Δb for California correspond to the values obtained using the multiple generation model.

There is not an obvious reason for the different behaviour of Japan and California earthquakes. We already discussed briefly some differences between them earth-

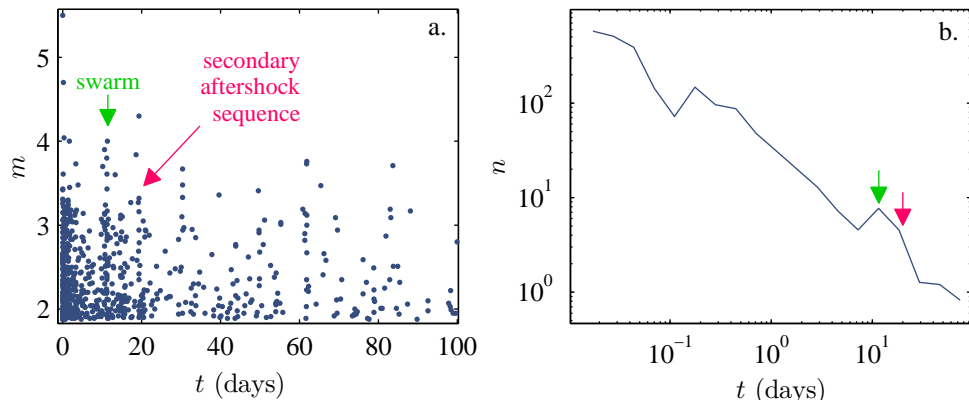


Figure 4.10: A time-magnitude representation of an aftershock sequence containing irregularities (a) and its Omori law (b).

quakes in section 2.1.2. Japan earthquakes are characterised by a lower b-value, and are more probable to be very large (≥ 6). They earthquakes are deeper, thus they occur in a zone of higher stress, which may cause the lower b-value [125]. These differences are important, but they are not supposed to influence the number of secondary aftershocks. It seems more probable that a higher rate of secondary aftershocks should be a consequence of heterogeneities in stress distribution. One could speculate that triggering a slip on California faults is easier: thus there are more secondary aftershocks, and less stress builds up, which would be at the origin of the higher b-value. Unfortunately we did not find any previous work comparing the secondary aftershock level in California and Japan, or the structure's crust in order to support our study.

5 Magnitude correlation

The existence of magnitude correlations within an aftershock sequence is still controversial (section 2.3, chapter 3). Since studying b-value variation with the frequency of analysis reveals the existence of temporal correlations within the signal, it may also provide information about magnitude correlations.

5.1 Magnitude correlations in the case of one-generation simulated sequences

The effect on the b-value decrease

We tested the influence of magnitudes correlation on the variation of the b-value in a very simple simulated case. We generated aftershock sequences using the BASS model, as previously. In the one-generation model all aftershocks are only related to the mainshock. Based on this, we can consider that magnitudes of aftershocks are related to the one of the mainshock only. This means that large earthquakes are more likely to occur at the beginning of a sequence. Hence, in order to simulate a system with correlated magnitudes we can simply switch magnitudes of some pairs of earthquakes and bring more of the large earthquakes at the beginning of the sequence. This is, clearly, a very rough approximation, and parameters should be adjusted very carefully to get a reliable model for simulating correlated earthquake sequences. In our case we just want to check if an increased number of large magnitude earthquakes has any effect on the decrease of the b-value with f_a , and get an approximate idea of the effect in question, so this simple method should be enough.

Several test simulations showed that the value of b_I is very slightly affected by magnitude correlations, but the length of w where the b-value drop occurs depends on magnitude correlations. In the case of "correlated" magnitudes the drop of b occurs for shorter integration windows than for uncorrelated magnitudes (figure 4.11.a). The difference is small (a factor of around 5 in the value of w_{drop} , depending on the intensity of the correlation), but systematic.

5.2 b-value variation of real aftershock sequences

In order to detect the eventual effect of the magnitude correlation we studied the decrease of b with w for the aftershock sequences and compared it with results for sequences with reshuffled magnitudes (so to eliminate magnitude correlation). STAI

can provoke a false impression of magnitude correlation, so in order to be sure that no earthquakes are missing in our data we cannot work with the very beginning of an aftershock sequence (section 3.3, chapter 3). This is regrettable in our case, since it is near the mainshock that inter-event times are the smallest and correlation should be the highest [74].

When the signal is integrated in time, the number of events decreases. The length of the sequences was limited to 10^7 seconds and the largest integration window is $w = 10^5$ s, so the number of integrated events can be as low as 100. For the aftershock sequences that we worked with this results in an incertitude on the calculated b-value so large that any interpretation would be impossible. Thus, as discussed in section 2.1, we will analyse groups of sequences within intervals $p \pm 0.1, b \pm 0.1$. Figure 4.11.b shows the results of the examination of b-values regarding w for one on these groups of aftershock sequences. The case of original seismic data and the case of mixed-up magnitudes are represented with blue circles and red squares, respectively. Because of poor statistics the results are very noisy and the drop is smoother than for simulations. Still, it seems that for the original data the drop of \underline{b} occurs for slightly shorter integration windows. Note that the sequence group that we used here is among the ones that contained the most earthquake events and thus had the best statistics.

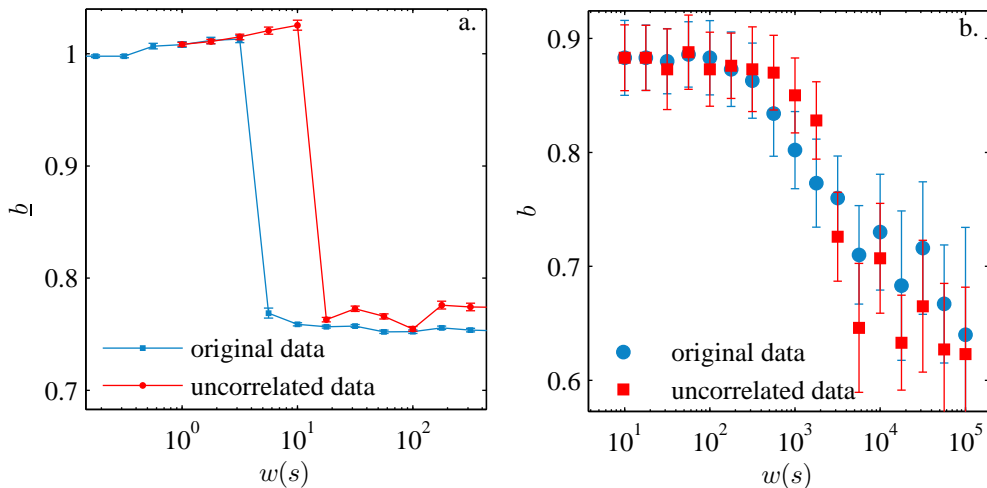


Figure 4.11: Variation of the Gutenberg-Richter exponent for simulated aftershock sequences (a) and real aftershock sequences (b), integrated over a time window of size w . Blue circles: original data (correlated magnitudes), red circles: uncorrelated magnitudes. For the catalogue data: 5 sequences with $p \sim 1.1$ and $b \sim 0.88$ were chosen (details are in Appendix D), table $p = 1.1$ of JMA catalogue.

6 Conclusion and perspectives

We showed, in the case of simulations and earthquake catalogue data that a low frequency observation of temporally correlated phenomena leads to an underestimation of the exponent of the energy power law. The decrease is due to the existence of time correlations in the signal, more precisely an Omori law time distribution. A reliable estimation of the Gutenberg-Richter exponent needs a measurement with high-enough frequency (able to resolve individual events with short waiting times).

We also proposed tools for estimating the exponent of the original power law when the low-frequency exponent is known. Since Omori law time distributions (direct or inverse ones) are encountered in other phenomena than earthquakes (the case of fracture has been previously discussed in this thesis), there exists other situations to which the results presented in this chapter could be applied.

The decrease of the energy distribution exponent is more important when the exponents p and b increase, but also when secondary aftershocks exist in the sequence. This last observation merits to be studied more thoroughly. Multiple generation earthquake simulations and analysis on other aftershock sequences rich in secondary aftershocks could help understand the mechanism behind it. Possibly, a method for estimating the fraction and importance of secondary aftershocks could be derived from the study of the relationship between b and w .

The study on the b-value variation with the frequency of analysis showed a slight effect which may be due to magnitude correlations. Due to poor statistics it is hard to conclude on this subject. The discussion on magnitude correlations continues in the following chapter, using different methods.

CHAPTER 5.

EARLY AFTERSHOCKS

1	Introduction	92
2	Magnitude correlations	93
2.1	Method	93
2.2	Results	96
2.3	Discussion	98
3	Temporal variations of the b-value	99
3.1	State of the art	99
3.2	Methods	100
3.3	Results	101
4	Conclusion	104

1 Introduction

The work presented in this chapter is related to one question: *are early aftershocks different than other aftershocks?* An aftershock sequence results from the process of stress release, at the level of the aftershock zone. Since the earthquake number in a sequence decreases as a power law with time, a great part of earthquakes occur at the beginning of the sequence. Hence most of the energy released during the sequence is released shortly after the mainshock (figure 5.1), and the mechanical properties of the crust in the aftershock zone could vary during this release. It is thus possible that early aftershocks (the ones that are detected within few hours or even days from the mainshock), occur in different systems than late ones, and they could show different behaviours.

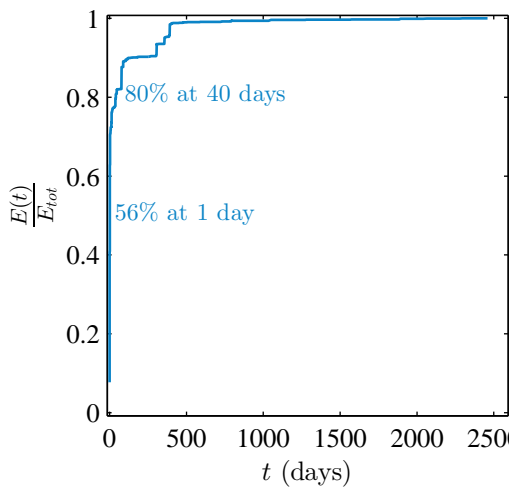


Figure 5.1: Cumulative energy released during an aftershock sequence, normalised by the total released energy.

It has recently been suggested that temporal distribution of the early aftershocks deviates from the Omori law [34], or at least follows a lower-exponent power law [103], which means that the activity rate decrease is slower at the beginning of the sequence. Ziv et al. [156] studied the magnitude distribution of earthquakes along three California faults and suggested that b-values are lower closely after a mainshock. Though it is not presented in the same way, the idea of magnitude correlation can also be interpreted in terms of early aftershock differing from the other earthquakes: the closer they are to the mainshock (spatially and temporally), the greater the magnitudes. These results could indicate that early aftershocks do occur in particular conditions (compared to late ones). Our work will focus on magnitudes, in particular the proportion of earthquakes with great magnitudes and the b-value of the magnitude distribution.

In catalogue data early aftershocks suffer strongly from STAII. It is possible to deal with this problem by completing the catalogue data using continuous seismic signals [70, 103, 104], or by removing data influenced by STAII (section 3.3, chapter 3) from existing catalogues. High quality continuous recordings are not easily available for all regions, and sophisticated data treatments should be applied in order to extract the aftershock properties. Hence, when studying early aftershocks, one approach consists in making a study which is easily generalisable, with methods that can be

applied to *any* catalogue, but with poorer amount of data per sequence, and another one is choosing more data per sequence but on far less samples. We will work with discrete data from earthquake catalogues (the first approach). The results that we will discuss here concern California and Japan earthquakes, but the analysis can easily be reproduced on data from any other earthquake catalogue.

2 Magnitude correlations

2.1 Method

In order to seek for magnitude correlations we propose a method applicable to aftershock sequences. It is based on the idea that if magnitudes are correlated when earthquakes occur closely in time, the ideal situation for observing this correlation is the beginning of an aftershock sequence. Indeed, the beginning of an aftershock sequence is where one can find numerous earthquakes occurring closely (spatially and temporally) to a large magnitude earthquake. Therefore, if any magnitude correlation exists between the mainshock and its aftershocks, early aftershocks should be bigger than late ones. So the simple question we would like to answer is: *is there a larger fraction of large earthquakes among the early aftershocks than among the later ones?*

To answer it, we start by transforming each aftershock sequence into a sequence with uniformly distributed times. This way, we get a sequence where the total number of earthquakes is constant in time. Then we check if there is a significant difference in the number of large magnitude events at the beginning and in the end of the sequence.

The most important characteristic of the method we use is that it is completely independent of STA. The main argument of studies arguing that magnitude correlation does not exist is the fact that the same effects can be observed because of STA, without any magnitude correlation. In our case we will be working with large magnitude events only, which are all well detected. Hence, no corrections need to be applied to the data. As will be seen later, even if there is any influence of STA, it would tend to make correlation observations more difficult, and not ease them.

2.1.1 Converting the power-law of times into a uniform distribution

We first want to transform the power-law distributed time characterising an aftershock sequence into a uniformly distributed time. So basically, we need a new time t_u , such that:

$$p(t)dt = p(t_u)dt_u \quad (5.1)$$

and

$$p(t_u) = C, \quad (5.2)$$

C being a constant.

$p(t)$ is given by the Omori law: $p(t) = \frac{1}{(t+c)^p}$. Let us skip all the discussions about the value of c (sections 2.1.1 and 2.2.1 in chapter 3) and suppose it is equal to 0. This hypothesis is justified because we are interested in large magnitude events for which c tends to be very small. Also, if the real value of c is positive, as some

studies indicate, supposing it is 0 will only make the effect of magnitude correlation more difficult to observe, but will not invalidate our conclusions if we do observe a magnitude correlation effect. So we consider here that

$$p(t) \propto t^{-p}, \quad (5.3)$$

thus

$$t_u \propto \frac{1}{1-p} t^{1-p}. \quad (5.4)$$

To be able to superpose results from different sequences we will synchronise the time scales: and use normalised values of t_u , scaling from 0 to 1, that we denote t_u^n :

$$t_u^n \propto \frac{t_n}{t_u^{max}}. \quad (5.5)$$

The result from converting time in t_u^n for an aftershock sequence can be seen in figure 5.2. Figures (a) and (b) show the original and the transformed sequence for an aftershock sequence in Japan, and (e) and (f) show the same variable for a simulated aftershock sequence.

2.1.2 What will we measure?

Once the sequences are transformed we want to separate the high magnitude (or high energy) events from the others. For each sequence the 0.5%¹ of events with highest magnitudes are defined as high magnitude events. A threshold magnitude m_{high} separating the high magnitude events is defined. Earthquakes with magnitudes lower than m_{high} define the mean and low magnitude events. Here we defined mean magnitude earthquakes by $m_{high} - 0.75 < m < m_{high}$, and low magnitude earthquakes by $m_{high} - 1.5 < m < m_{high} - 0.75$ ². The three types of events are represented with different colors in figure 5.2. The kind of behaviour we are looking for is directly visible on this figure. Figures (a) and (e) show, respectively, the time-magnitude diagram of an aftershock sequence in Japan, and a simulated aftershock sequence. They look very similar. Earthquakes are more numerous at the beginning, and this holds for large earthquakes too. Figure (b) and (f) show the same sequences, but represent magnitudes as a function of t_u^n . In both cases the number of mean and small earthquakes seems uniform with t_u^n (at least for large t_u^n). For the real seismic data (b) large earthquakes are clearly more numerous at the beginning. Many of them occurred within the first month of the sequence, while the total recording we work on is of 3 years. This is not observed on the simulated sequence.

These two different behaviours can be seen more clearly on figures (c) and (g) - they represent the normalised number of events that occurred within intervals of t_u^n , for each magnitude class. For the simulated sequence (g) the three curves are

¹The choice of the fraction of events that are taken was made arbitrarily and does not affect the result as long as it stays small (0.5 – 3%)

²The span of magnitudes including the mean and low energy events can also vary. Intervals of 0.75 contain enough events so that the results are not too noisy, but do not reach to very low magnitude events where the catalogue may be incomplete. Similar results were reproduced with magnitude intervals of 0.5 and 1

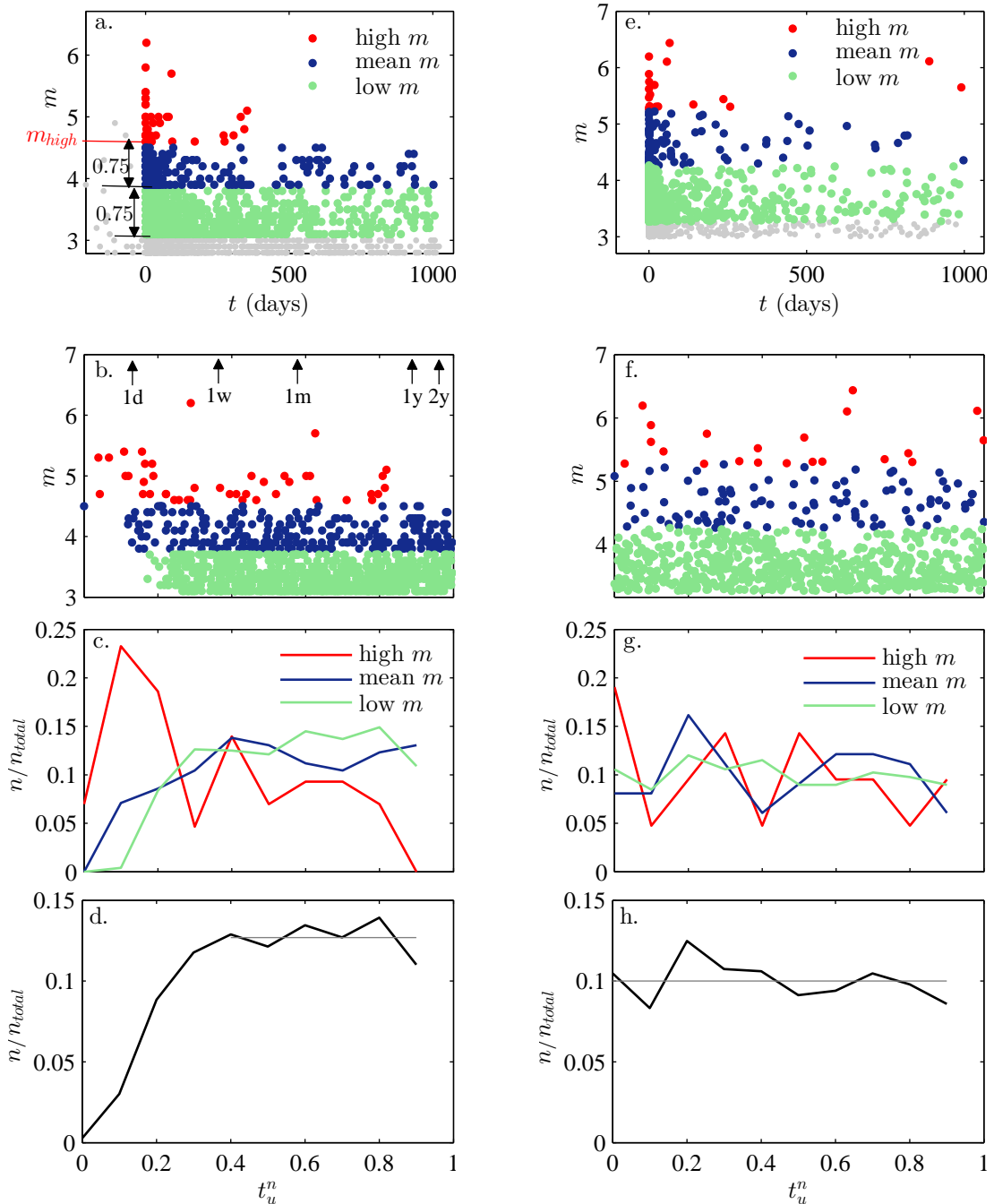


Figure 5.2: Illustration of the effect of time change from t to t_u . Events are separated in high energy (red), mean energy (blue), and low energy (green) events. On the left are represented the results for the aftershock sequence of the October 23, 2004 Chuetsu earthquake and on the right results a simulated sequence with no magnitude correlation with similar parameters. For each example are represented: (a and e) magnitude versus time; (b and f) magnitude versus the uniformly distributed time t_u^n ; (c and g) fraction of occurred events of each type (high, mean and low energy) as per t_u^n interval; (d and h) fraction of occurred events (of all magnitudes) per t_u^n interval.

roughly constant (some noise occurs because of the finite amount of data). For the experimental data (c) the number of low and mean magnitude events increases at the beginning of the sequence and then stays constant. This is a consequence of STAI, small events not being detected shortly after the mainshock. The number of high magnitude events, on the contrary, *decreases* with t_u^n : large-magnitude events are more numerous at the beginning of the sequence. Figures (d) and (h) serve as verification of the method, showing that, considering all magnitudes, the number of earthquakes is (on average) constant with t_u .

Since the number of high energy events that can be used for each sequence is very small - not more than few tens of earthquakes - the results that we get for separate sequences are very noisy. In order to lower the statistical error we will work with all available sequences together.

2.2 Results

2.2.1 Japan earthquakes

We apply the previous analysis on long aftershock sequences, fixing the end of a sequence at 3 years. Thus, we can only work with sequences that present few and small secondary aftershocks and no other ms-as sequences for this duration. The existence of another sequence (secondary or not) would imply waiting times that are shorter than usual, biasing the fact that in an aftershock sequence waiting times between earthquakes become longer with time, which our method is based on. Only 17 sequences from the JMA catalogue satisfy this criteria³. Figure 5.3 shows the result of the analysis for the Japan earthquakes. On the left is represented the fraction of occurring earthquakes as a function of t_u^n . For mean and low magnitude earthquakes the fraction of earthquakes is more-or-less constant, except for low t_u^n where the STAI effect can be seen. On the contrary, the number of high magnitude

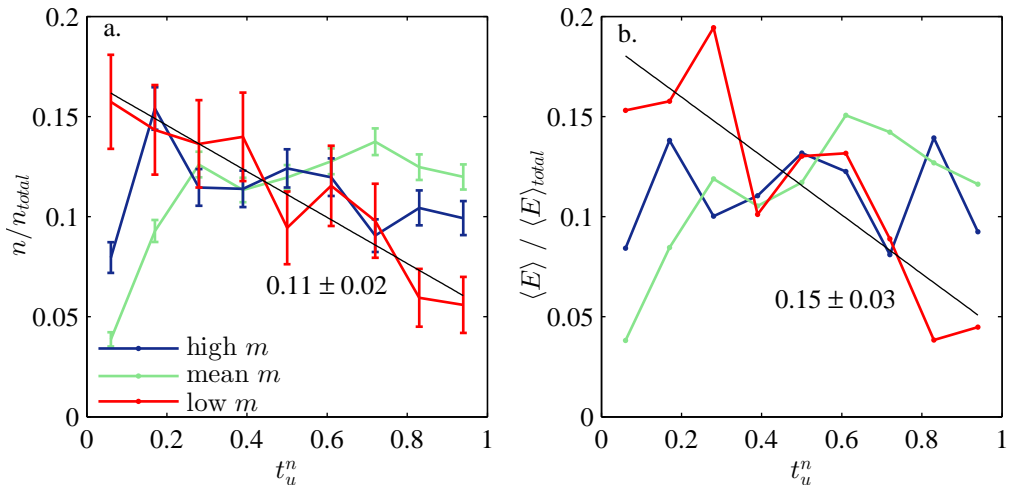


Figure 5.3: (a) Fraction of earthquakes occurring at given t_u^n , for different magnitude groups. 17 3-years-long earthquake sequences from the JMA catalogue were taken for this analysis. Error bars represent statistical errors. (b) Fraction of energy occurring at given t_u^n for different magnitude groups.

³For identification, a list of the sequence's mainshocks and a map of their localisation is available in Appendix E.1

earthquakes decreases with t_u^n . The number of large magnitude earthquakes is about three times bigger at the beginning of a sequence than at its end. A linear fit applied on the relation between high energy events and t_u^n resulted in a slope of -0.11 ± 0.02 . The same analysis applied to the energy of earthquakes gives similar results, with a slightly steeper linear fit.

Almost half of the considered aftershock sequences were close (spatially and temporally) to the $m = 9.0$ 2011 Tohoku earthquake. We verified that the decreasing number of large magnitude events is not only due to these earthquakes, by separating the sequences in two groups (related and non-related to the great Tohoku earthquake) and analysing each one of them.

2.2.2 California earthquakes

The seismic activity in California is much weaker than in Japan. The number of large earthquakes is smaller, and subsequently the number of aftershocks per sequence is smaller too. We also found that a recurrent detection problem exists, and the catalogues are sometimes missing medium or even large earthquakes. More importantly, as we discussed previously (section 4), many of the earthquake sequences present secondary sequences or swarms. Finally, with all these criteria taken into account, only 4 sequences were retained from the NCSN catalogue, and 7 sequences⁴ from the SCSN catalogue. For NCSN this is not enough to make any conclusions on magnitude correlation. The results from the analysis on SCSN sequences are shown in figure 5.4. The correlation effect is less important than in the case of JMA, but a similar tendency is still visible.

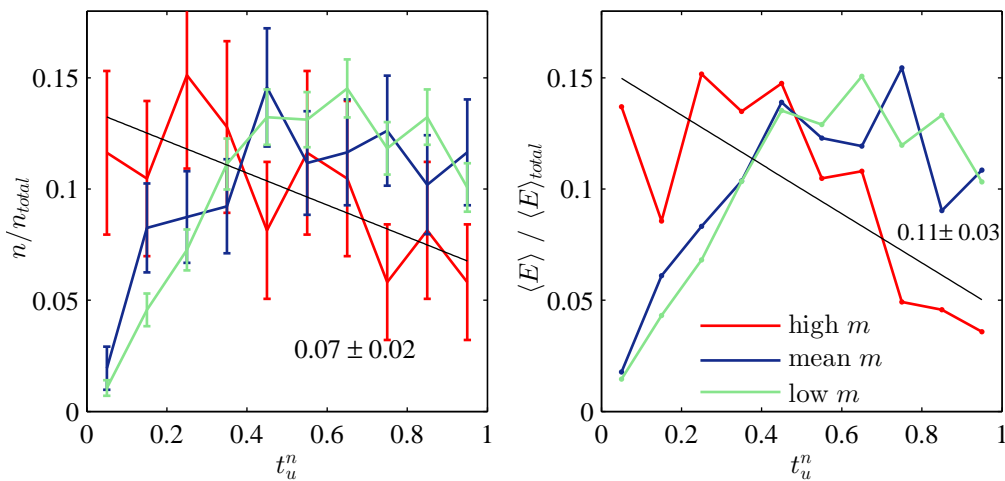


Figure 5.4: (a) Fraction of earthquakes occurring at given t_u^n , for different magnitude groups. 7 sequences from the SCSN catalogue were taken for this analysis. Error bars represent statistical errors. (b) Fraction of energy occurring at given t_u^n for different magnitude groups.

In both cases (California and Japan) we can conclude that *large magnitude events are more likely to occur among the early aftershocks than the late ones*. It seems that the energy of large magnitude events decreases more sharply with t_u^n than their number does. Since the incertitudes in the linear fits are large, for the time being

⁴Listed in Appendix E.1

we can only speculate that large magnitude events are also bigger at the beginning of a sequence. More statistics is needed in order to prove this result.

2.3 Discussion

To our knowledge, this study is the first one showing evidence of magnitude correlation with considerations on large magnitude earthquakes only. We showed that the fraction of large energy aftershocks is considerably bigger among the aftershocks which occur shortly after the mainshock. This is in agreement with Lippiello et al.'s theory which proposes that earthquakes which are close in time and space tend to have similar magnitudes.

Nevertheless, our results impose some changes on the magnitude correlation model proposed by Lippiello et al. [74]. According to this model, and making the assumption that aftershocks magnitudes are correlated only to the mainshock, the probability of having an aftershock of magnitude M_i at the time t_i knowing that a mainshock $M_0(t_0)$ has occurred, can be written as

$$P(M_i(t_i)|\{M_0(t_0)\}) = F\left(\frac{t_i - t_0}{k10^{b(M_0 - M_i)}}\right), \quad (5.6)$$

F being any normalisable function. This probability is deduced from the idea that the time laps between the two events $t_i - t_0$ has a characteristic time scale $k 10^{b(M_0 - M_i)}$ fixed by the magnitude difference $M_0 - M_i$ (k is a constant measured in seconds). Using this probability function one obtains a distribution of magnitudes independent from time, if time is rescaled by $k10^{b(M_0 - M_i)}$.

One of the examples given for F is $F(z) = \frac{A}{z^\lambda + \gamma}$, which results in:

$$P(M_i(t_i)|\{M_0(t_0)\}) = \frac{A}{\left(\frac{t_i - t_0}{k10^{b(M_0 - M_i)}}\right)^\lambda + \gamma} \quad (5.7)$$

The effect of the parameter γ is crucial here. If it is equal to 0 we retrieve a regular power law with no correlations. When it is positive, its effect is to prevent the probability of small magnitudes from getting too large: even for very small magnitudes $P(M_i(t_i)|\{M_0(t_0)\})$ will not increase above $\frac{A}{\gamma}$. So using this function, one induces time correlations in seismic models, by reducing the number of small earthquakes at the beginning of the sequence. We do not know if in reality the number of small earthquakes is lower at the beginning of a sequence or not⁵, but our results show that the number of high energy events certainly is more important at the beginning of an aftershock sequence. Thus, for $F(z)$ one should not simply use any normalisable function, but a function which increases the number of big aftershocks at small (waiting) times.

⁵This seems extremely hard to estimate, given that most of the small earthquakes are difficult to detect shortly after the mainshock

3 Temporal variations of the b-value

As discussed previously (section 2.4, chapter 3) variations in differential stress are widely accepted as the cause of b-value variations. Knowing that the dynamics of earthquakes is a process of accumulation and release of stress in the earth's crust, one should expect the differential stress of a region during an aftershock sequence to vary in time and thus provoke temporal variations of the b-value. This is not obvious to verify since several complications are related to studies of temporal variations of the b-value. Most of the existing studies on the subject did not take these complications into account, or are not systematic enough to be generalised. We will start by a brief summary of these studies.

3.1 State of the art

While spatial variations of b have been thoroughly studied (for a review see [153] and references therein), temporal variations of b - or of the aftershocks' dynamic in general - are more difficult to detect and quantify. Firstly, they are much more subtle than spatial variations [151]. Secondly, temporal changes in the earthquake statistics can be due to temporary detection anomalies (as STAI) [62] or permanent detection changes [157], making reliable studies hard to conduct.

Despite the difficulties, studies on this subject do exist. Most of them treat variations of the b-value on large spatial scales, and more importantly try to detect long lasting variations. These methods show no significant results. Wiemer et al. for example, concluded that "lasting and significant changes of b-value as a function of time are not common" [153]. This is not that surprising, given that lasting temporal variations of b would mean that permanent structural changes have been induced in the considered region. Nevertheless, in a very localised cluster, immediately before or after a sequence of strong earthquakes variations of the b-value should be observed because of the important stress release that occurs. Thus observing temporal variations of b should be easier on local, short-time scales. Probably one of the reasons which make this approach unpopular is the small number of events that can be considered when the space and time span of the considered data is small. It can only be applied on very active regions, where the number of events even on local scales will be of several hundreds, and using very sensitive methods for estimating the b-value.

3.1.1 Short-time, local b-value variation

Earthquake prediction being of a major interest for humanity, most of the studies about local, short-term temporal b-value variation concern precursory phenomena, i.e. variations occurring before a mainshock. The activity before a mainshock is often quite low, thus making precise estimations of the b-value hard (the different results on this subject were discussed in section 2.6.1, chapter 3).

We found few studies that discussed the variation of the b-value *after* a big earthquake on a local scale [44, 86, 156]. They all indicate that immediately after the mainshock and in the region close to it, the b-value starts with a lower-than-usual value, then increases in time. This behaviour could be related to stress or structural changes occurring during the aftershock sequence. Unfortunately, in [44, 86] STAI is not taken into account, even though it has been shown that it can provoke a low-

ering of the b-value [62]. This makes it impossible to discriminate between a real, physical increase of b and the artefact rising from the incomplete detection of small aftershocks. One of the studies [156] deals with STAI by the method of suppressing close pairs of earthquakes (see section 3.3 in chapter 3) with a very low time limit on the time lag between pairs, plus considers only data from three faults in California. This subject merits to be studied more thoroughly, and to our knowledge, a systematic and reliable study about it is still lacking. In this section we will present our attempts on doing one.

3.1.2 The link with magnitude correlation and stress release

We showed previously that the fraction of big earthquakes is more important at the beginning of an earthquake sequence. The b-value being a measure of the ratio of small to large earthquakes, its value should be affected by this. Since larger events are more numerous, we expect the b-value to be smaller at the beginning of a sequence.

Considering previous work done on b variation we decided to concentrate our study on the particular behaviour of the b-value shortly after a mainshock, during the aftershock sequence. Following the hypothesis that the aftershock sequence induces a stress release in the considered region - i.e. a drop of the differential stress, we expect the b-value to increase following a mainshock.

3.2 Methods

In the JMA catalogue, 89 earthquake clusters were isolated, and 88 ms-as sequences were identified within these clusters. Since we want to calculate the b-value over windows of 200 points, only sequences with at least 400 aftershocks above the magnitude threshold are considered. These sequences were inspected for swarms and secondary aftershocks (visually and by estimating the variations of the Omori law) and the ones presenting these features were omitted from the analysis. This leaves 19 ms-as⁶ sequences that we can work with, and a total of less than 27000 earthquakes, meaning that only about 6% of the events in the JMA catalogue could be used in our study.

The same procedure was applied to SCSN catalogue, resulting in a total of 14 ms-as sequences⁷ to be examined⁸.

STAI was taken care of according to the method seen in section 2.2 from chapter 3. Remember that this means that the very beginning of an aftershock sequence is omitted from the analysis.

⁶Listed in E.2.

⁷Listed in E.2.

⁸Almost the same criteria were applied to data selection for the study of magnitude correlations (section 2.2) and this study, but the few existing differences are important. Firstly, in the present case we can truncate sequences earlier than at 3 years, in cases where another mainshock occurs, so some of the sequences ruled out on the magnitude correlation study can be used now. Secondly, the study on magnitude correlation paid little attention to low magnitude earthquakes and their completeness. In the present case we need a sequence which is complete, and whose completeness magnitude is relatively low, in order to be able to fit the power law. Hence some sequences which were suitable for magnitude correlation analysis are not suitable here.

3.3 Results

3.3.1 Observations

The 19 ms-as JMA sequences satisfying the necessary conditions for our study showed few different behaviours:

- For 12 sequences the b-value increases significantly, and then it either stabilises or the sequence is interrupted by another sequence (for an example see figure 5.5.b). A *significant increase* is defined as a non-overlapping in the errorbars of the highest and lowest b-value. This is the behaviour we expect given the stress release considerations.
- For 4 sequences the b-value increases right after the mainshock, and then decreases or oscillates around a mean value higher than its value for short times (5.5.d). After careful inspection of the sequences we saw that some of these oscillations were due to secondary aftershocks (that were very few and thus were not detected during the visual inspection) or detection problems (missing small magnitudes).
- 2 sequences presented a non-significant b increase (5.5.f).
- In one case the b-value seems to remain constant. Nevertheless, this sequence presents important detection anomalies for immediate aftershocks and the calculation of the b-value starts very late - after about ~ 100 days. At this point it is very likely that b already reached a stable value and the increase occurred before the complete recording.

All in all, 16 out of 19 analysed sequences in the JMA catalogue show that the b-value of an aftershock sequence increases with time, starting from the mainshock. No conclusions can be drawn from the remaining 3 sequences. Note that they do not present a behaviour completely opposite to what we expected.

For the SCSN aftershock sequences the situation is similar: 11 out of 14 SCSN sequences show a significant increase in the b-value, 2 have a non-significant increase, and one has an oscillating b-value after the increase.

It seems that an increase of the b-value after a mainshock, and during the beginning of an aftershock sequence is quite a systematic behaviour, at least in Japanese and Californian earthquakes. We will now try to quantify this relation.

3.3.2 Quantitative results

Though qualitative results are encouraging, studying this behaviour quantitatively is more difficult. Because of STAI, the analysis starts at different times after the mainshock, which can vary from few hours (figure 5.5.d) to few days (figure 5.5.f). Plus, the way b increases differs between the different sequences since the rising time and the mean b-values vary between sequences. Still, to get a qualitative idea of the b variation in time, we put together all the $b = f(t)$ curves from the 19 sequences. The mean b-value differs between sequences, but since we are only interested into its increase, we can set them all to the same level without affecting the results of

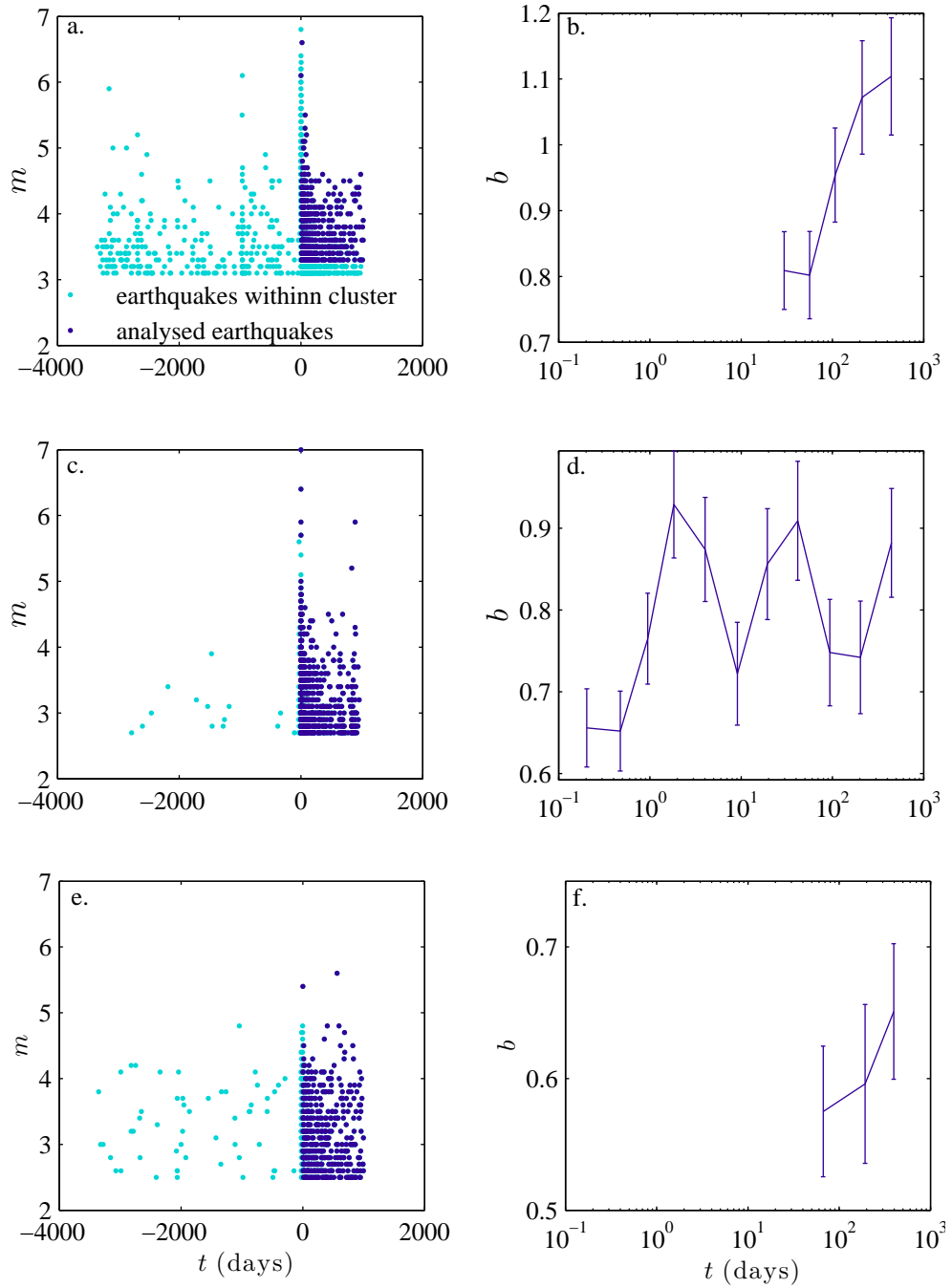


Figure 5.5: Left: time-magnitude representations of three aftershock sequences. The main-shock time has been set to 0. Right: Variation of the b -value during the corresponding sequence. Note that the starting time is different for the three figures - this depends on the recording quality (the severity of STA).

our observations. For each sequence we chose to set to 0 the b-value calculated for the time closest to 10 days. This does not make the curves collapse, but makes it much easier to see whatever tendency they have. The result is represented on figure 5.6. An increase of b can be observed even though the b-values calculated for the individual sequences (circles) are quite scattered. For the mean b value, the total increase between the beginning and the end of the sequence is of 0.28 for Japan earthquakes, and 0.4 for California earthquakes.

When b is represented as a function of the logarithm of time it seems to present a linear increase. Nevertheless, it seems more appropriate to observe b variations with the uniformly distributed time t_u^n : it corresponds to observing the b increase with the number of earthquakes. In this case it seems that the increase of b is the most important at the beginning of the sequence, then slows down. This is particularly visible for the Japan earthquakes (figure 5.6.b). We would expect that if the sequences we work with were longer, we could have observed an increase and then a stabilisation of the b value. Note that in our estimation we do not have access to the b-values corresponding to immediate aftershocks (see section 3.3), so we are certainly underestimating the value of the b increase.

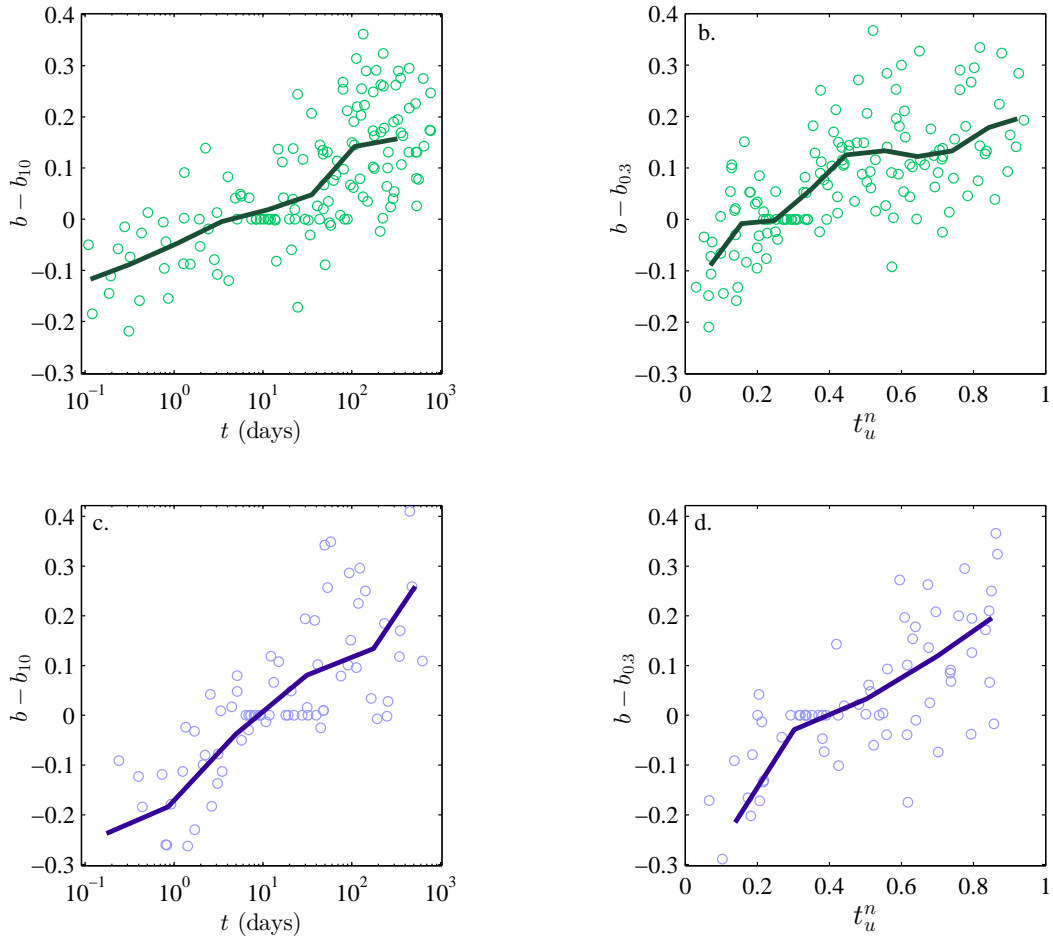


Figure 5.6: Variation of the b-value with respect to time t (a) or the reduced time t_r (b) for JMA earthquakes. Circles correspond to combined results of all the 20 ms-as sequences, the line is the mean value for all sequences combined. (c) and (d): same results for SCSN earthquakes

Even though these variations seem small, they change significantly the statistical properties of a sequence, as was discussed in section 2.1.2 of chapter 3. Considering that the estimation of Δb we made is largely underestimated, we conclude that very large earthquakes are orders of magnitude more likely to occur among the early aftershocks.

4 Conclusion

By studying earthquakes from Japan and California we showed that:

- the fraction of high magnitude earthquakes is greater at the beginning of an aftershock sequence than at the end of it;
- the b-value increases after the mainshock, during the aftershock sequence.

Observations were made using data directly from earthquake catalogues, and with taking precautions in order to avoid spurious effects from the short time aftershock incompleteness. In total about 200 sequences⁹ in three different catalogues were examined in order to search for the ones which are long enough, productive enough, and with few and weak secondary aftershocks. The observations hold for both regions, indicating that this behaviour may be universal.

The two features are related to each-other, and can both be explained considering the hypothesis that the differential stress of the crust decreases during an aftershock sequence. In this case, the early events, which occur in a state of higher stress, are more likely to be of great magnitude [126], and have a lower energy distribution exponent [125, 128].

We can conclude that early aftershocks are different from the rest of an aftershock sequence: they are bigger. Other studies suggest that the number of aftershocks decreases more slowly at the beginning than for the rest of the sequence. Combined, these two observations suggest that there may be a particular state at the beginning of an aftershock sequence. One could speculate that the system is quickly rearranging in order to fit in the new stress configuration induced by the mainshock slip. Once this is done, a stable power-law decrease of the activity and a fix b-value are respected, until the next perturbation of the system.

The observation of magnitude correlations has important consequences on the aftershock prediction (especially the great ones, which are of biggest practical interest), but also on the earthquake modelling. An upgrade would be necessary to current earthquake models in order to include this feature. Also, some of the fundamental laws concerning aftershocks may need a reexamination. In particular, the way we interpret Båth's law is completely based on the independence of the magnitude from each-other. Knowing that magnitude are correlated brings a new element to it.

⁹This corresponds to all great sequences in Japan from 2002 to 2014 and in California from 1970 to 2014.

CONCLUSION

This thesis deals with statistical properties of fracture dynamics in heterogeneous materials and of earthquake aftershocks. Both processes present a scale invariant dynamics, which manifests as power law distributions of event sizes and times (either times between consecutive events or between the mainshock and its aftershocks). The power laws are characterised by their *exponents*, indicating the ratio of small to large events in the case of the energy power law, or the intensity of the dynamics' slowing down for the time distribution power law. The focus of this thesis is mostly on the variation of these exponents and its origins.

Variations of the Omori law exponent

The study on fibre bundle fracture concerned the temporal dynamics of the bundle fracture, and in particular the exponent of the Omori law p . At constant strain, increasing the structural disorder in the bundle can either increase or decrease p , depending on the strength of the broken fibres. The effect of the applied stress on p is different in simulations and experiments, possibly due to the process of damage accumulation in fibres which was not taken into account in the simulations.

Importance of the frequency of the measurement for the exponent of the Gutenberg-Richer law

The subcritical fracture propagation in paper was observed by direct imaging (DI) and acoustic emission (AE) monitoring, originally with the idea of verifying the reliability of AE as damage indicator. Both observation methods result in power-law distributions with similar exponents (for energies and waiting times), provided that they are analysed at the same frequency. This corroborates the idea that all AE bursts originate from the fracture process. Furthermore, we observed that AE monitoring is more sensitive to fracture propagation than DI: while DI allows to observe macroscopic fracture opening due to damage accumulation, AE bursts correspond to more-elementary fracture events (single or few fibres breaking). AE monitoring revealed the existence of time correlations, in particular aftershocks, during the crack propagation.

The exponent of the energy distribution for the low frequency DI observation was lower than the one obtained by high frequency AE. The difference is due to the existence of aftershocks, which could not be discriminated from their mainshock using DI, that led to a lower, misleading value for the exponent of the energy distribution.

The same reasoning was applied to simulated and experimental earthquake aftershock sequences. Using simulated data we observed that when the frequency of analysis decreases, the distribution of energies separates in two power laws. The original power law holds for high magnitudes, and a new power law with a lower exponent value is followed by low magnitudes, with a crossover which depends on the frequency of analysis. If the frequency of analysis gets low enough only the second energy power law is observed for the distribution of energies. This effect is related to

the Omori distribution of aftershocks' times, and the exponent of the second power laws is related to the exponent of the Omori law. Hence, when analysed at low frequencies, the Gutenberg-Richter law and the Omori law are related.

In both cases (paper fracture and earthquake aftershocks) the decrease of the exponent of the energy distribution resulted directly from the existence of temporal correlations between the events. Therefore, we expect that this effect should concern any scale invariant phenomena exhibiting time correlations.

Magnitude correlations in aftershock sequences

We analysed earthquake aftershock sequences by "stretching" the time series of the signal in order to generate uniformly-distributed aftershock times, hence compensate the effect of the Omori law. The number of high magnitude earthquakes is greater in the beginning of the stretched sequences than in the end. This result confirms the recent controversial propositions of the existence of magnitude correlations between events which are close in time. The result is also corroborated by the fact that b-value increases with time during an aftershock sequence. Current methods of earthquake simulation and prediction are based on the hypothesis that magnitudes are independent from each other. Confirming the existence of magnitude correlations could considerably affect them, and change some aspects of the interpretation of aftershocks behaviour.

APPENDICES

A Spectral distance

This appendix provides details about the spectral distance calculation used for analysis of acoustic emission recordings of paper fracture (section 2.2.2 from chapter 1).

In order to detect acoustic bursts in within the acoustic signal, we defined a spectral distance - a new signal relate to the energy (rather than the amplitude) of the acoustic emissions. Usually spectral distance is calculated by considering the logarithms of the power spectra of signals [9]. However, taking into account that the response of the piezoelectric sensor is flat between 100 KHz and 5 MHz, which covers the whole range of the frequencies that concern our experiment (typically 140 KHz), we have chosen to define a linear spectral distance [79] which is directly proportional to the signal's energy and thus makes energy estimations simpler. The spectral distance $D_{S,N}(t)$ is calculated as the integral over a time window w_d of the difference between the power spectra of the signal averaged over all the frequencies, $\langle \bar{S} \rangle_f(t)$, and the power spectra of the noise, averaged over all the frequencies and over a time interval of at least 0.5 s, $\langle \bar{N} \rangle_{f,t}$:

$$D_{S,N}(t) = \frac{1}{w_d} \int_{t-\frac{w_d}{2}}^{t+\frac{w_d}{2}} [\langle \bar{S} \rangle_f(t') - \langle \bar{N} \rangle_{f,t}] dt'. \quad (8)$$

The power spectrum of the noise is determined using the signal recorded during the calibration (without complete loading), in order to have a signal where no rupture has occurred. We choose a time interval of $w_d=100 \mu\text{s}$. This value has been found after an optimization process: the window must be short enough so that short events aren't dominated by the noise part, and long enough to detect long events in one single part. To determine the optimal length tests with different window sizes were performed and the results were compared especially by considering long events.

We detect acoustic events by thresholding the spectral distance. The threshold is defined as the maximum value of the spectral distance of the noise with itself.

$$trsh = \max(D_{N,N}(t)) \quad (9)$$

This method (figure A.1) is much more sensitive to acoustic emissions in paper compared to direct signal thresholding: in our case the number of detected events is almost four times greater. It is possible to detect events whose amplitude is in the range of the noise amplitude (figures A.1 c and d).

Once an event is detected, its energy is defined as the integral of the spectral distance (equation 8) over its duration. The duration of the event corresponds to the

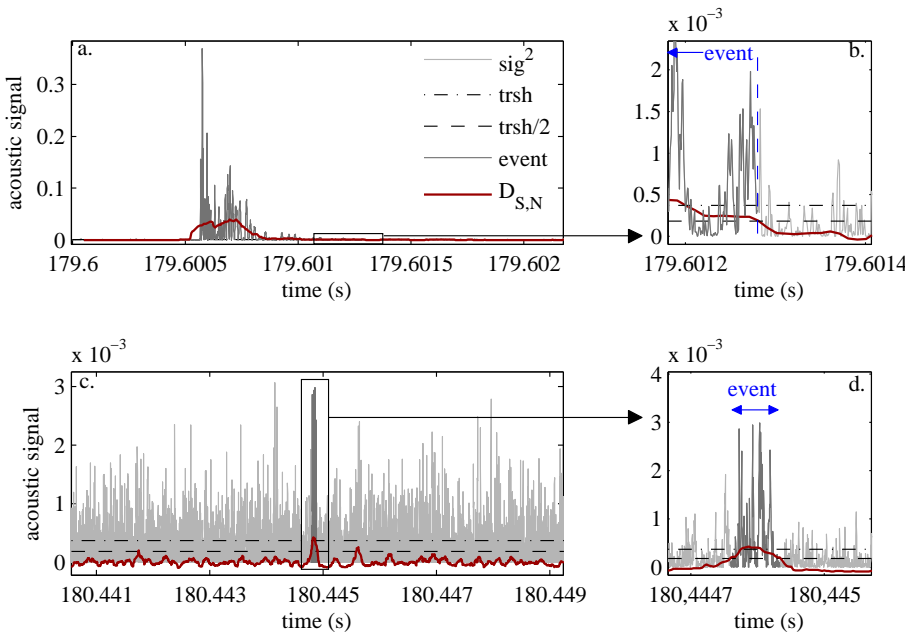


Figure A.1: Detection of acoustic events. Light gray line (sig^2): square of the acoustic signal, red line ($D_{S,N}$): spectral distance of the signal to the noise, black dash-dot line (trsh): threshold value of the spectral distance, black dashed line ($\text{trsh}/2$): threshold value of the spectral value divided by 2, dark gray line (event): acoustic signal corresponding to an event,

a: High energy event: the acoustic signal amplitude presents few local maximums. b: Determining the end of an event by thresholding the spectral distance. c: Low energy event: the event's amplitude is in the range of the noise amplitude. d: Zoom on the low energy event.

part of the spectral distance overcoming the detection threshold divided by 2. This lowering of the threshold and the relatively large time window assure that we take into account the whole duration of events. We prefer this definition of the energy to the maximal amplitude of the signal (or of the spectral distance) because acoustic events are not single punctual bursts: they sometimes have irregular shapes in time, presenting few local maxima as consequence of the fact that few fibers can break consecutively in a very small lapse of time, appearing as one single event (figure A.1.a). Taking into account only one of these maxima would result in neglecting a considerable proportion of the acoustic energy. Finally, once an event's duration is defined, energy is calculated by integrating the spectral distance over time rather than the square of the signal itself, which decreases the influence of the noise.

B Experimental procedure for fibre bundle fracture

Here we provide details about the experimental procedure used for the study of fibre bundle fracture (section 3.2 of chapter 2).

B.1 Bundle preparation

The glass fibres are taken from an industrially produced E-glass bobbin. Fibres come in small bundles of about 200 fibres each.

We pick 10 of these small bundles to prepare our 2000-filament bundles. The bundle is pinched at one of its ends with a metallic peg, than rinsed with ethanol. This allows the fibres to align.

A 6.5 cm zone of the bundle is delimited using a thermoretractable sheath: little portions of sheath are placed around the bundle, then they are heated until they clamp the bundle. The sheaths delimit the part of the bundle which will be studied (in between the sheaths) from the parts used for holding and manipulating the bundle. They also allow for a mechanical extensometer to be fixed.

The external parts of the bundle were rigidified using epoxy: the bundle is soaked with 24-hour epoxy (we pinch the bundle with a metallic tweezers to help the epoxy penetrate between the fibres), then straightened-up by hand, and the epoxy dries in an oven at 70°C for 40 minutes.

When both ends are prepared this way, they become rigid, and can be introduced into the metallic supports' cylindrical holes, which are filled with epoxy. For each metallic supported the bundle is again left in the oven for 40 minutes for the epoxy to dry. The metallic supports contain placements for the acoustic sensors allow for the sample to be held by chucks. The final result is represented in figure A.2.c.

B.2 Experimental set-up

Before setting the bundle specimen on the traction machine, one needs to prepare it for immersion and acoustic emission monitoring. The result of this preparation is schematically represented on figure A.2.a - a glance at it before reading the description of the preparation procedure may help visualising the process.

Immersion and acoustic monitoring

To be able to completely immerse the bundle, we simply use the top part of a plastic bottle cut in half. First, a hole of the diameter of the metallic edge's narrow part is made in the cap, so the lower metallic edge of the bundle can pass through it. This way the totality of the bundle can be immersed, while the bottom metallic edge is on the outside of the bottle and can be fixed to the traction machine. Once the cap is on the metallic edge and the bottle is around the bundle, the bottle is closed and glued on the cap, to assure impermeability. The upper metallic edge of the bundle contains a sensor-shaped hole, where the sensor (Micro 80) is placed, and fixed with a metallic clamp. Good contact between the metallic edge and the sensor is assured using vacuum grease. When these steps are accomplished, the bundle is ready to be mounted on the traction machine. Each of the metallic edges is held by a chuck mounted on the traction machine.

Force measurement and control

The traction machine used for this experiments, *Instron 1195*, is a commercial

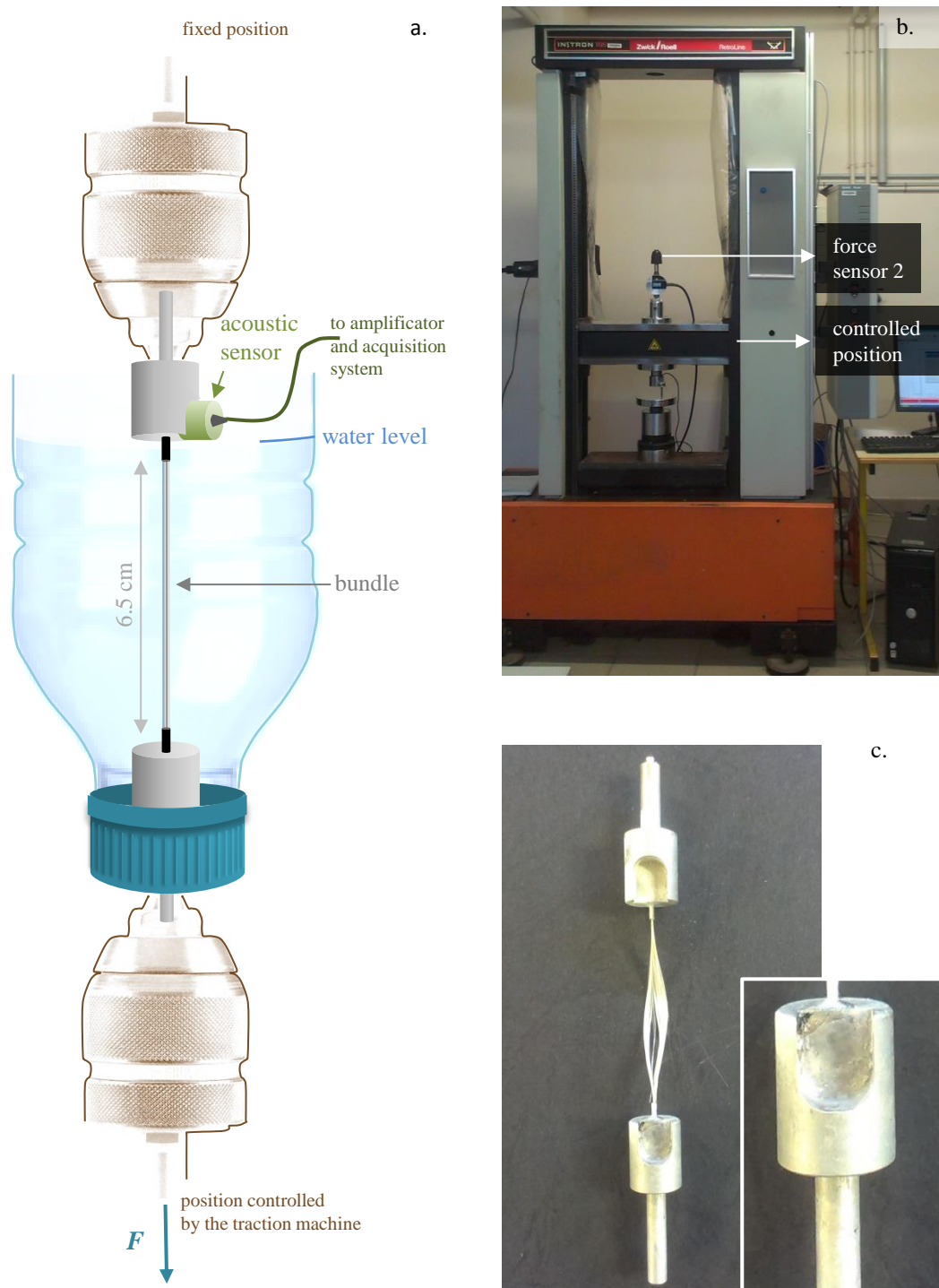


Figure A.2: a. Schematic representation of the experimental set-up. b. Photography of the traction machine (Instron 1195) used for the experiments. c. Photography of a prepared bundle.

stepper-motor machine which can control force or deformation, for traction and compression experiments. A commercial software - *TestXpert* is used to control the parameters of each experiment. The Instron machine uses a built-in force sensor placed on the top of the machine for controlling the force during the experiments. The upper chuck is connected to this sensor. The bottom end of the bundle is held by a second chuck, mounted on a second force sensor (*Kyowa LTZ-200KA*), related to the moving bar of the traction machine. This sensor was added in order to have a second, independent measure of the force. Its signal is recorded by a *NI BNC2110* card, independently from other data from the testing machine.

Temperature control

Most of the experiments were done at room temperature, but few tests were also made by varying the temperature. For this purpose we used a thermostatic bath. The water level on our experiments must not vary for more than few millimetres: the bundle must be completely immersed and the acoustic sensor should not get in contact with water. Unfortunately, finding thermostatic baths which regulate the flow well enough to be used in this case is not obvious. Thus it was impossible for us to use a thermostatic bath as an open circuit, directly regulating the temperature of the water the bundle is immersed in. Instead we used a long silicone tube which we wrap around the bottle (before closing up the bottle) and connect to the thermostatic bath. We used a 50% – 50% water-glycol mixture for the bath liquid. The liquid in the tube can heat up (or cool down) the water in the bottle, thus the temperature of the water is somewhere between room temperature and the bath temperature. For example, for bath temperature of 65°C and room temperature of 23°C, the water temperature is 45°C¹⁰.

Acoustic emission monitoring

Acoustic data was measured using a PZT transducer (Acoustic Emission type μ 80), whose signal was amplified by 40dB and then recorded using *PCI2*, a data acquisition system from Mistras, used with *AE Win* software. The acoustic signal is monitored continuously and the software detects acoustic events simultaneously, by thresholding the amplitude of the signal. The signal is not stored continuously: the system automatically stores some characteristics (occurrence time, amplitude, duration, energy, peak frequency), and the waveform (i.e. the continuous acoustic signal recorded right before and after the event) of each detected event. With our settings, for each event we dispose of the acoustic signal measured from 2.5 ms before to 0.5 ms after the starting time of the event, at a sample frequency of 5 MHz.

B.3 Experimental protocol

Before starting the experiment, the thermostatic bath temperature is set and stabilised to the value we need.

Once the equipped bundle is mounted on the test machine, the tube is related to the thermostatic bath. The temperature in the bath changes due to the increased contact it has with the exterior. We wait for the temperature in the bath to stabilize before continuing the experiment.

¹⁰A temperature calibration was done before the series of fracture experiments. The room temperature was rather stable (around 23°C), so fixing the bath temperature fixed the water temperature too.

When the temperature is stable, we apply a very small charge (~ 2 N) to the bundle. We verify if the sensor is recording, by lightly hitting the metallic edge it is fixed-on, and checking the recording on the acoustic monitoring software.

We fill the bottle with water. For controlled-temperature experiments the water should already be on the desired temperature. Note that the bath liquid has been circulating in the tube before the water is added. The water is already at its stable temperature (for the given bath temperature), thus the temperature is quasi constant during the experiment.

Finally, we launch the experiment. The bundle is loaded at a constant displacement rate of 0.5 mm s^{-1} . When a pre-defined value of the force on the bundle is reached (typically 150-200 N) the loading stops and a constant displacement is maintained. Each experiment lasted about 4 h and a few longer tests were made.

C Details about the fibre bundle experiments

C.1 Some basic considerations on mechanics

This appendix provides details about the calculation of physical variables which are not directly accessible during an experiment (listed in section 3.4 from chapter 2).

The initial fibre number

Bundles have a variable number of fibres. For each bundle the exact initial number of fibres N_0 is calculated using the slope of the force-deformation curve S_0 at the beginning of the experiment. Since the Young modulus of individual fibres is known ($Y=72$ GPa), one can estimate the initial number of fibres as:

$$N_0 = \frac{S_0}{\pi r^2 Y}, \quad (10)$$

r being the radius of the fibre. For our bundles N_0 varied from about 1500 to 2200.

Estimating the strain

A direct measurement of the fibre elongation during the experiment is impossible, because the bundle is immersed. The test machine controls the displacement of the lower bar supporting the experimental set-up, so we have access to the position of this bar. Hence we know the deformation of the system consisting of the bundle, the chucks, the force sensors and metallic supports, which we note δl_{system} . During tests on non-immersed bundles we recorded the elongation of the bundle δl_{bundle} using an extensometer, and then compared it with δl_{system} . We found that the deformation of the bundle and the deformation of the machine are linked linearly, and verify:

$$\delta l_{bundle} \sim 0.85 \delta l_{system}. \quad (11)$$

Hence the strain is calculated as $\epsilon = \frac{0.85 \delta l_{system}}{l_0}$, with $l_0 = 6.5$ cm.

The force per fibre

After the loading, a constant force per fibre $F_{/fib}$ is applied to each fibre:

$$F_{/fib} = \frac{F_0}{N_I} = \frac{F_0}{N_0 - n_{loading}}, \quad (12)$$

N_I being the number of fibres remaining in the bundle when loading is complete, and $n_{loading}$ the number of fibres broken during loading. $n_{loading}$ can be estimated either from the number of acoustic fracture events detected before the force reaches F_0 , or from the difference between F_0 and the value of the linear extrapolation of the force-displacement relation F_0^{extr} (see figure 2.13.b in chapter 2). The two values, which we will note F_{fib}^{AE} and F_{fib}^F , are quite similar (figure A.3.a).

The stress-strain relation for fibres

Once the loading phase of an experiment is done, each fibre is subjected to a constant stress σ and a constant strain ϵ in time. The calculation of stress is based either on the $F_{/fib}^{AE}$ or the $F_{/fib}^F$ estimation, so two values of σ are determined. Both σ^{AE} and σ^F are linearly related to the strain ϵ . Figure A.3.b shows this relation for all the experiments. The proportionality coefficient corresponds to the Young modulus of the fibres $Y = 72$ GPa.

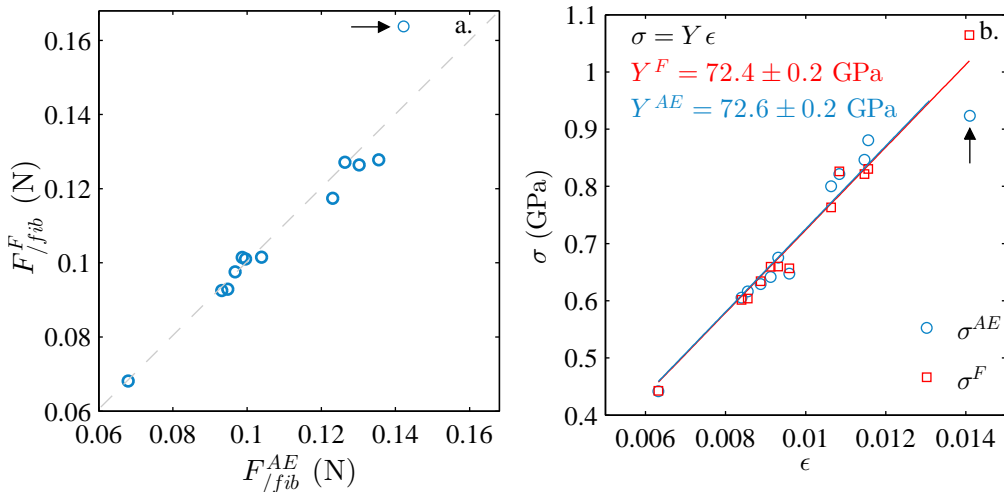


Figure A.3: (a) Relation between the force per fibre calculated by estimating $n_{loading}$ acoustically, and the force per fibre calculated by estimating $n_{loading}$ mechanically. (b) Stress-strain relation for all experiments, and the resulting fit for the Young modulus of glass fibres. The arrows point towards an experiments that presented problems in the acoustic emission recording during the loading.

The arrow on figure A.3.b points to an experiment which we suspected to have acoustic detection problems at the beginning, during the loading. The lack of acoustic events led to an underestimating of $n_{loading}$ and so of F_{fib}^{AE} too¹¹.

C.2 The fibres' strength

Here we explicit the method on determining the bundle's strength discussed in section 3.5 of chapter 2 and show results of the strength distribution on some of the bundles.

Distribution of strengths within a bundle

We can access the distribution of strengths by loading a sample at a constant strain rate until all fibres are broken. If AE and the strain are continuously recorded one can later estimate the failure stress of each fibre as

$$\sigma_s = \frac{F(t)}{S(N_0 - n(t))}, \quad (13)$$

t being the occurrence time of the fibre's fracture, $n(t)$ the number of fibres broken up to time t , and $S = \pi r^2$ the fibre's section. Since the experiment is quite fast (takes few minutes) there is very little time for subcritical fracture to occur in each fibre, so this method allows to estimate the distribution of initial strengths in the bundle. The distribution of strengths is usually supposed to be a Weibull or normal distribution [77]. For consistency with the model and for simplicity we chose to fit by a normal distribution¹².

¹¹Later analysis showed that some other experiments had detection problems too. Nevertheless, these problems sometimes developed with time (figure 2.15.a), so are not very important at the beginning, hence the value of σ^{AE} is not significantly biased.

¹²We do not focus on the differences between Weibull and normal distribution, since this is not important for the rest of the chapter.

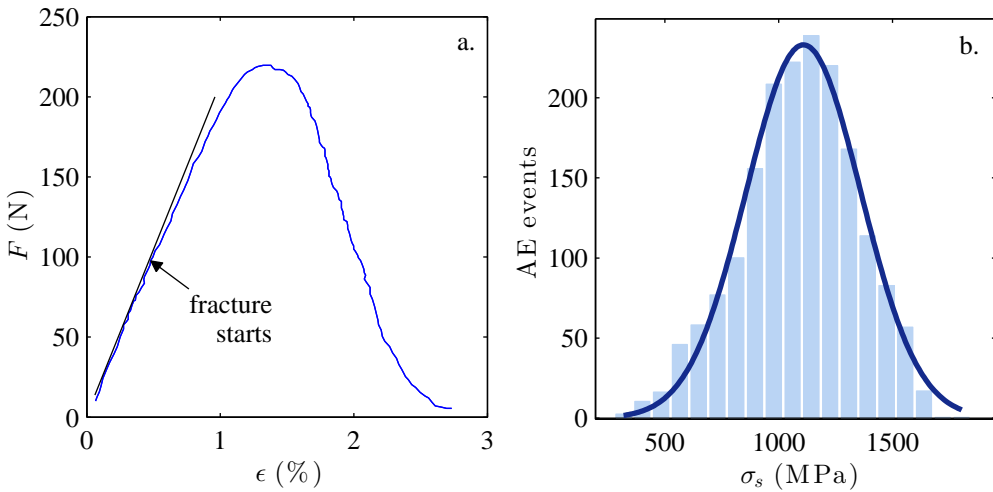


Figure A.4: (a) Force-strain relation during an experiment of loading a bundle with a constant strain rate. (b) Histogram of the stress value at which events were detected, i.e. histogram of fibre's strength.

Variability between bundles

We studied the distribution of σ_c on the bundles used for the constant strain experiments¹³. The same analysis as previously was applied, but we could only use the loading part of each experiment.

First, we analysed the bundle's behaviour during the loading and saw some differences: the time needed to make them deviate from the linear increase of the force varies between experiments. Figure A.5.a, represents the force variation with time (the elongation rate is constant, so this is equivalent to a force-elongation plot) for 4 experiments (including the two extreme cases: the strongest and the weakest bundles). The 4 experiments are done at room temperature. The difference is partially due to the varying number of fibres in each bundle. For example, one can see that the bundle with the highest modulus on figure A.5.a is the one which contains the most fibres. But this does not explain everything, since the bundle with $N_0 = 1716$ (violet) has a lower modulus than the $N_0 = 1675$ bundle (yellow). This is due to a variability of the fibre's strength.

If we apply the method used for figure A.4.b. to the loading part of each experiment, we get an estimation of the strength of the fibres broken during the loading. Figure A.5.b represents the distribution of σ_c for the 4 bundles in figure A.5.a. One bundle stands out by the large number of fibres broken at low stress, while the three others seem to have similar distributions of fibre strengths.

¹³This is same series of experiments that we used for studying the Omori law exponent in section 3.6.3

The estimation of fibre strength was done for all the bundles, and except for the one represented in A.5.b they all have similar strengths¹⁴. The weak bundle was left out from all future analysis since we do not know if it is generally weaker than the others, or the low strength only concerned its weakest fibres.

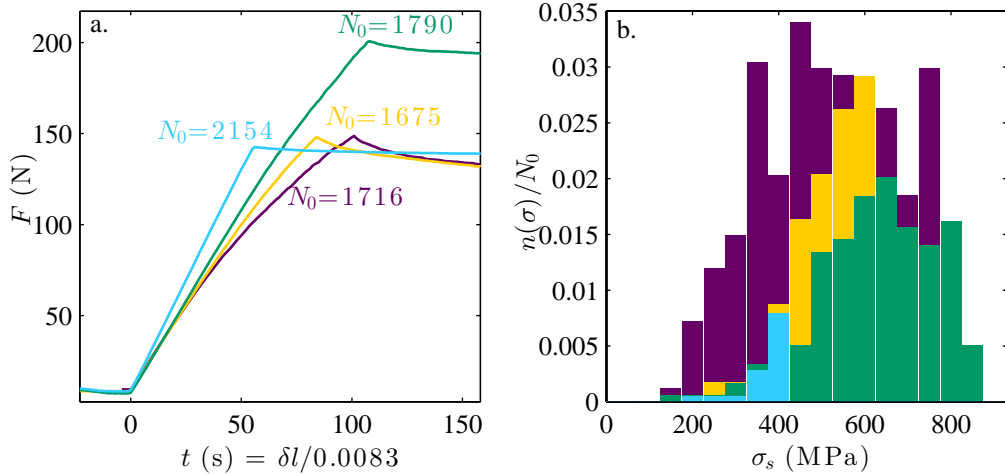


Figure A.5: (a) Force variation during the loading for 4 different experiments conducted at room temperature. (b) Histogram of failure stress for the fibres broken during the loading for the four experiments on the right.

¹⁴Some small variations in the strength exist, and future results were examined considering these variations, but they did not have any obvious effect.

D Details on the earthquake sequences used for the analysis of the b-value decrease with f_a

Here we provide details about the sequences used in the study on b-value variation with the frequency of analysis (chapter 4, section 4). The sequences which were used for the calculation of each experimental point from figure 4.9 are identified by their mainshock. One table per point is presented.

D.1 JMA catalogue

$$p = 0.7$$

date	magnitude	longitude	latitude
20 April 2005	5.8000	130.2880	33.6780
17 March 2008	4.5000	136.2100	37.0690
11 March 2011	5.7000	140.5760	36.7170
16 March 2011	6.1000	140.9060	35.8370

$$p = 0.9$$

date	magnitude	longitude	latitude
20 March 2005	7.0000	130.1760	33.7390
23 July 2005	6.0000	140.1380	35.5820
25 March 2007	6.9000	136.6860	37.2210
29 September 2009	6.1000	127.8580	27.8690
11 December 2011	5.5000	129.5430	28.1310
18 April 2013	6.1000	123.4540	25.0020

$$p = 1.1$$

date	magnitude	longitude	latitude
26 July 2003	6.4000	141.1710	38.4050
05 September 2004	7.4000	137.1410	33.1380
27 February 2010	7.2000	128.6800	25.9190
11 March 2011	7.6000	141.2650	36.1080
11 April 2011	7.0000	140.6730	36.9460

$$p = 1.4$$

date	magnitude	longitude	latitude
16 July 2007	6.8000	138.6090	37.5570
15 March 2010	5.2000	128.2640	28.8110

D.1.1 SCSN catalogue

$p = 0.97$

date	magnitude	longitude	latitude
08 July 1986	5.6500	-116.6080	33.9990
16 October 1999	4.7400	-116.3410	34.7060
04 April 2010	7.2000	-115.2950	32.2860

$p = 1.15$

date	magnitude	longitude	latitude
16 October 1999	5.7700	-116.2900	34.6780

$p = 1.51$

date	magnitude	longitude	latitude
24 November 1987	6.6000	-115.8520	33.0150
28 June 1992	6.3000	-116.8270	34.2030

D.1.2 NCSN catalogue

$p = 0.86$

date	magnitude	longitude	latitude
22 December 2003	6.5000	-121.1005	35.7005

$p = 0.1.01$

date	magnitude	longitude	latitude
2 May 1983	6.7000	-120.3120	36.2317
21 July 1986	6.4000	-118.4428	37.5380
24 April 1992	6.4500	-124.5660	40.4325
25 April 1992	6.6900	-124.2287	40.3353

E Details on the earthquake sequences used in chapter 5

E.1 Sequences for magnitude correlation analysis

Here we provide details about the analysis on magnitude correlation (section 2.2 of chapter 5) and the sequences used for it.

E.1.1 Japan earthquakes

17 sequences of the JMA catalogue were used. The date, magnitude and position of each sequence's mainshock are given in table 1. Sequences were selected as the cluster of events around each mainshock, visually delimited by defining a containing polygon, and they each lasted 3 years. The clusters of events are represented on a spatial map in figure A.6.

date	magnitude	longitude	latitude
26 May 2003	7.1	141.6510	38.8210
26 July 2003	6.4	141.171	38.405
23 October 2004	6.8	138.8670	37.292
20 April 2005	5.8	130.2880	33.6780
15 March 2006	7.9	154.0480	46.7030
16 June 2008	7.2	140.8810	39.0300
11 March 2011	7.6	141.2650	36.1080
11 March 2011	6.6	142.2800	39.0310
11 March 2011	6.4	141.9110	37.6760
11 March 2011	6.2	144.6030	38.0910
11 March 2011	6.1	142.2080	37.3720
11 March 2011	5.8	141.1950	36.2910
11 March 2011	5.7	140.5760	36.7170
11 March 2011	5.5	141.9070	37.3710
28 March 2011	6.5	142.3460	38.3840
09 April 2011	5.4	141.815	38.247
11 April 2011	7.0	140.6730	36.9460
14 April 2012	6.9	145.2270	40.7750

Table 1: Characteristics of the mainshocks of the sequences used for the magnitude correlation analysis in the JMA catalogue.

Eight of the considered sequences occurred at the same day as the $m = 9.0$ 2011 Tohoku earthquake¹⁵. They are possibly aftershocks of this earthquake. This should not interfere with our analysis since we simply want to study earthquakes which are close spatially and temporally, whatever their source. Figure A.7 shows the fraction of high, mean and low magnitude earthquakes as a function of t_u^n for (a) sequences non-related to the 2011 Tohoku earthquake, and (b) sequences probably related to it. Both present a decreasing number of high magnitude aftershocks with t_u^n . The effect is more drastic for Tohoku earthquake's aftershocks. Looking for an explanation of this behaviour we calculated the mean waiting times between the first 50 aftershocks with $m \geq 3$. For the sequences Tohoku earthquake's aftershocks

¹⁵The great Tohoku earthquake itself could not be included in this analysis, since a limited small aftershock zone cannot be associated to it.

the mean waiting time is of approximately 2.5 hours, while it is equal to 12 hours for the other sequences. According to recent observations of magnitude correlation [74], magnitude correlation is greater between earthquakes which are close in time, which could explain the difference between the two groups of sequences.

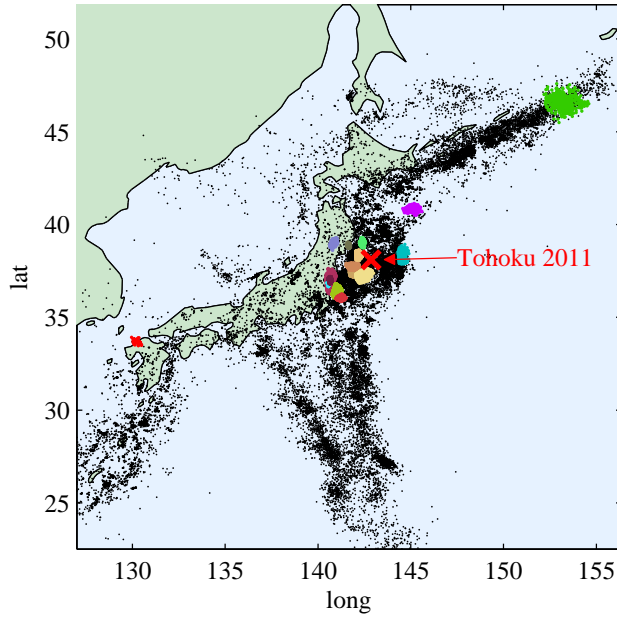


Figure A.6: Position of the events clusters used for the magnitude correlation analysis in the JMA catalogue.

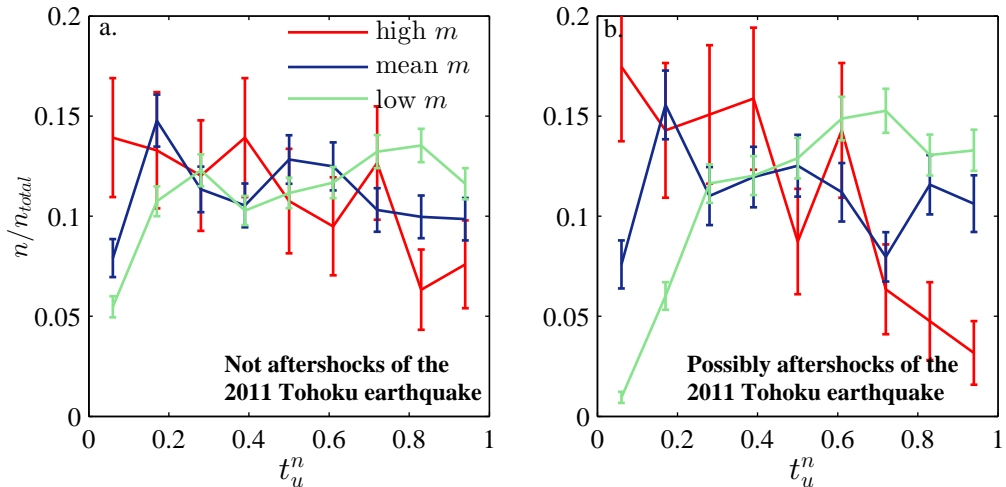


Figure A.7: Fraction of earthquakes occurring at given t_u , for different magnitude groups. (a) 9 sequences non related to the 2011 Tohoku eqrthsucke. (b) 8 sequences probably related to the 2011 Tohoku earthquake.

E.1.2 California earthquakes

Here we provide characteristics and locations of the 7 sequences suitable for analysis on magnitude correlation in the SCSN catalogue.

date	magnitude	longitude	latitude
28 June 1992	7.3	-116.4370	34.2000
28 June 1992	4.3	-116.5200	34.4760
01 July 1992	5.3	-116.4640	34.3300
17 January 1994	6.7	-118.5370	34.2130
16 October 1999	5.8	-116.2900	34.6780
16 July 2001	5.2	-117.8740	36.0160
04 April 2010	7.2	-115.2950	32.2860

Table 2: Characteristics of the mainshocks of the sequences used for the magnitude correlation analysis in the SCSN catalogue.

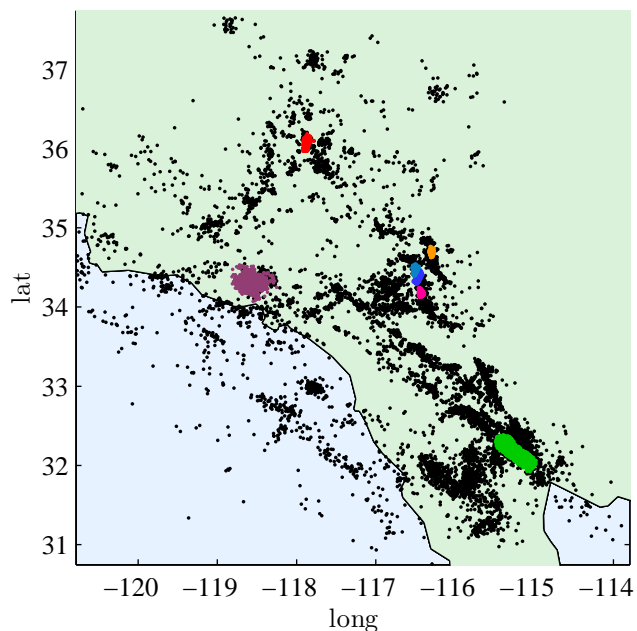


Figure A.8: Position of the events clusters used for the magnitude correlation analysis in the SCSN catalogue.

E.2 Details on the b-value variation analysis

Tables 3 and 4 resume the characteristics of the mainshocks of sequences used for the analysis of temporal variation of the b-value (section 3.2 of chapter 5) in Japan and California respectively.

date	magnitude	longitude	latitude
26 February 2003	8.0	144.0780	41.7790
26 July 2003	6.4	141.1710	38.4050
23 October 2004	6.8	138.8670	37.2920
20 April 2005	5.8	130.2880	33.6780
15 March 2006	7.9	154.0480	46.7030
25 March 2007	6.9	136.6860	37.2210
17 March 2008	4.5	136.2100	37.0690
16 June 2008	7.2	140.8810	39.0300
11 March 2011	7.6	141.2650	36.1080
11 March 2011	6.6	142.2800	39.0310
28 March 2011	6.5	142.3460	38.3840
11 March 2011	6.4	141.9110	37.6760
11 March 2011	6.1	142.2080	37.3720
11 March 2011	5.8	141.1950	36.2910
11 March 2011	5.7	140.5760	36.7170
11 March 2011	5.5	141.9070	37.3710
19 March 2011	6.1	140.5710	36.7840
09 April 2011	5.4	141.8150	38.2470
11 April 2011	7.0	140.6730	36.9460

Table 3: Characteristics of the mainshocks of the sequences used for the magnitude correlation analysis in the SCSN catalogue.

date	magnitude	longitude	latitude
15 March 1979	4.45	34.3490	-116.4290
08 July 1986	5.7	33.9990	-116.6080
08 July 1986	5.7	33.9990	-116.6080
28 June 1992	7.3 34.2000 -116.4370		
28 June 1992	6.3	34.2030	-116.8270
28 June 1992	4.1	34.2890	-116.4440
28 June 1992	4.3	34.4760	-116.5200
29 June 1992	4.2	34.6420	-116.4880
01 July 1992	5.3	34.3300	-116.4640
17 January 1994	6.7	34.2130	-118.5370
16 October 1999	5.8	34.6780	-116.2900
16 October 1999	4.5	34.8030	-116.3200
16 July 2001	5.2	36.0160	-117.8740
04 April 2010	7.2	32.2860	-115.2950

Table 4: Characteristics of the mainshocks of the sequences used for the magnitude correlation analysis in the SCSN catalogue.

BIBLIOGRAPHY

- [1] J. R. A R Bunsell. *Fundamentals of Fibre Reinforced Composite Materials*. Marcel Dekker, 2005.
- [2] K. Aki. Maximum Likelihood Estimate of b in the Formula $\log N = a - bM$ and its Confidence Limits. *Bull. Earthq. Res. Inst.*, 43:237–239, 1965.
- [3] M. J. Alava, P. K. V. V. Nukala, and S. Zapperi. Statistical models of fracture. *Adv. Phys.*, 55(3-4):349–476, 2006.
- [4] E. Altshuler, O. Ramos, C. Martínez, L. E. Flores, and C. Noda. Avalanches in One-Dimensional Piles with Different Types of Bases. *Phys. Rev. Lett.*, 86(24):5490–5493, 2001.
- [5] D. Amitrano. Brittle-ductile transition and associated seismicity: Experimental and numerical studies and relationship with the b value. *J. Geophys. Res.*, 108(B1):2044, 2003.
- [6] J. G. Anderson, J. N. Brune, J. N. Louis, Y. Zeng, M. Savage, G. C. Yu, Qingbin, and D. DePolo. Seismicity in the western Great Basin apparently triggered by the Landers, California, earthquake, 28 June 1992. *Bull. Seismol. Soc. Am.*, 84(3):863–891, 1992.
- [7] P. Bak, C. Tang, and K. Wiesenfeld. Self-Organized Criticality: An Explanation of $1/f$ Noise. *Phys. Rev. Lett.*, 59(4):381–384, 1987.
- [8] J. Baró and E. Vives. Analysis of power-law exponents by maximum-likelihood maps. *Phys. Rev. E*, 85(6):066121, 2012.
- [9] M. Basseville. Distance measures for signal processing and pattern recognition. *Signal Processing*, 18(4):349–369, 1989.
- [10] H. Bauke. Parameter estimation for power-law distributions by maximum likelihood methods. *Eur. Phys. J. B*, 58(2):167–173, 2007.
- [11] T. Baumberger, C. Caroli, and D. Martina. Solvent control of crack dynamics in a reversible hydrogel. *Nat. Mater.*, 5(7):552–555, 2006.
- [12] O. Ben-David, G. Cohen, and J. Fineberg. The dynamics of the onset of frictional slip. *Science*, 330(6001):211–214, 2010.
- [13] K. Birkeland and C. Landry. Power laws and snow avalanches. *Geophys. Res. Lett.*, 29(11):49,1–49,3, 2002.
- [14] G. Boffetta, V. Carbone, P. Giuliani, P. Veltri, and A. Vulpiani. Power laws in solar flares: self-organized criticality or turbulence? *Phys. Rev. Lett. Lett.*, 83(22):4662–4665, 1999.

- [15] D. Bonamy. **Intermittency and roughening in the failure of brittle heterogeneous materials.** *J. Phys. D. Appl. Phys.*, 42(21):214014, 2009.
- [16] D. Bonamy and E. Bouchaud. **Failure of heterogeneous materials: A dynamic phase transition?** *Phys. Rep.*, 498(1):1–44, 2011.
- [17] M. Bottiglieri, L. de Arcangelis, C. Godano, and E. Lippiello. **Multiple-Time Scaling and Universal Behavior of the Earthquake Interevent Time Distribution.** *Phys. Rev. Lett.*, 104(15):158501, 2010.
- [18] A. Cao and S. S. Gao. **Temporal variation of seismic b -values beneath north-eastern Japan island arc.** *Geophys. Res. Lett.*, 29(9):48,1–48,3, 2002.
- [19] R. Capozza, S. M. Rubinstein, I. Barel, M. Urbakh, and J. Fineberg. **Stabilizing Stick-Slip Friction.** *Phys. Rev. Lett.*, 107(2):024301, 2011.
- [20] S. Ciliberto, a. Guarino, and R. Scorreretti. **The effect of disorder on the fracture nucleation process.** *Phys. D Nonlinear Phenom.*, 158(1-4):83–104, 2001.
- [21] A. Clauset, C. R. Shalizi, and M. E. J. Newman. **Power-Law Distributions in Empirical Data.** *SIAM Rev.*, 51(4):661–703, 2009.
- [22] P.-P. Cortet, L. Vanel, and S. Ciliberto. **Dynamical Law for Slow Crack Growth in Polycarbonate Films.** *Phys. Rev. Lett.*, 99(20):205502, 2007.
- [23] A. Cowking, A. Attou, A. M. Siddiqui, M. A. S. Sweet, and R. Hill. **Testing E-glass fibre bundles using acoustic emission.** *J. Mater. Sci.*, 26(5):1301–1310, 1991.
- [24] P. Daguer, B. Nghiem, E. Bouchaud, and F. Creuzet. **Pinning and Depinning of Crack Fronts in Heterogeneous Materials.** *Phys. Rev. Lett.*, 78(6):1062–1065, 1997.
- [25] H. E. Daniels. **The statistical theory of the strength of bundles of threads.** i. *Proceedings of the Royal Society of London A: Mathematical, Physical and Engineering Sciences*, 183(995):405–435, 1945.
- [26] Z. Danku and F. Kun. **Creep rupture as a non-homogeneous Poissonian process.** *Sci. Rep.*, 3:2688, 2013.
- [27] J. Davidsen and G. Christian. **Are seismic waiting time distributions universal?** *Geophys. Res. Lett.*, 31(21):L21612, 2004.
- [28] J. Davidsen and A. Green. **Are Earthquake Magnitudes Clustered?** *Phys. Rev. Lett.*, 106(10):108502, 2011.
- [29] J. Davidsen, G. Kwiatek, and G. Dresen. **No Evidence of Magnitude Clustering in an Aftershock Sequence of Nano- and Picoseismicity.** *Phys. Rev. Lett.*, 108 (3):038501, 2012.
- [30] A. Delaplace, S. Roux, and G. Pijaudier-Cabot. **Avalanche statistics of interface crack propagation in fiber bundle model: characterization of cohesive crack.** *J. Eng. Mec.*, 127(7), 2001.

- [31] A. Deluca and A. Corral. **Fitting and goodness-of-fit test of non-truncated and truncated power-law distributions.** *Acta Geophys.*, 61(6):1351–1394, 2013.
- [32] S. Deschanel, L. Vanel, N. Godin, G. Vigier, and S. Ciliberto. **Experimental study of crackling noise: conditions on power law scaling correlated with fracture precursors.** *J. Stat. Mech. Theory Exp.*, 01:P01018, 2009.
- [33] B. Enescu and K. Ito. **Values of b and p: their Variations and Relation to Physical Processes for Earthquakes in Japan.** *Annals of Disas. Prev. Res. Inst., Kyoto Univ.*, (46 B), 2003.
- [34] B. Enescu, J. Mori, and M. Miyazawa. **Quantifying early aftershock activity of the 2004 mid-Niigata Prefecture earthquake (M w 6.6).** *J. Geophys. Res.*, 112(B4):B04310, 2007.
- [35] K. E. Evans, B. D. Caddock, and K. L. Ainsworth. **Statistical changes during the corrosion of glass fibre bundles.** *J. Mater. Sci.*, 23(8):2926–2930, 1988.
- [36] K. Felzer. **Secondary aftershocks and their importance for aftershock forecasting.** *Bull. Seismol. Soc. Am.*, 93(4):1433–1448, 2003.
- [37] K. R. Felzer and E. E. Brodsky. **Decay of aftershock density with distance indicates triggering by dynamic stress.** *Nature*, 441:735–738, 2006.
- [38] K. R. Felzer and D. Kilb. **A Case Study of Two M 5 Mainshocks in Anza, California: Is the Footprint of an Aftershock Sequence Larger Than We Think?** *Bull. Seismol. Soc. Am.*, (5):2721–2735.
- [39] A. M. Freed. **Earthquake Triggering By Static, Dynamic, and Postseismic Stress Transfer.** *Annu. Rev. Earth Planet. Sci.*, 33(1):335–367, 2005.
- [40] V. Frette, K. Christensen, and A. Malthe-Sørensen. **Avalanche dynamics in a pile of rice.** *Nature*, 379:49–52, 1996.
- [41] S. Frohlich, Cliff; Davis. **Teleseismic b Values; Or, Much Ado About 1.0.** *J. Geophys. Res.*, 98(B1):631–644, 1993.
- [42] X. Gabaix, P. Gopikrishnan, V. Plerou, and H. Stanley. **A theory of power-law distributions in financial market fluctuations.** *Nature*, 423:1–4, 2003.
- [43] A. Garcimartin, A. Guarino, L. Bellon, and S. Ciliberto. **Statistical properties of fracture precursors.** *Phys. Rev. Lett.*, 79(17), 1997.
- [44] S. J. Gibowicz. **Variation of the Frequency-Magnitude Relation During the 1931 Hawkes Bay, 1934 Pahiatua, and 1942 Wairarapa Aftershock Sequences.** *New Zeal. J. Geol. Geophys.*, 16(4):1009–1045, 1973.
- [45] K. Goda and H. Fukunaga. **The evaluation of the strength distribution of silicon carbide and alumina fibres by a multi-modal Weibull distribution.** *J. Mater. Sci.*, 21(12):4475–4480, 1986.
- [46] A. A. Griffith. **The phenomena of rupture and flow in solids.** *Philos. Trans. R. Soc. London*, 22:163–198, 1921.

- [47] B. Gutenberg and C. F. Richter. Frequency of earthquakes in California. *Bull. Seism. Soc. Am.*, 34(4):185–188, 1944.
- [48] B. Gutenberg and C. F. Richter. Magnitude and energy of earthquakes. *Ann. Geophys.*, 53(1), 1956.
- [49] H. Hamaguchi and A. Hasegawa. Investigation on the Aftershocks of the Tokachi-oki Earthquake of 1968 , (2) Statistical Study on Time Distribution. *Sci. Reports Tohoku Univ. Ser. 5, Geophys.*, 20(3):119–133, 1970.
- [50] T. C. Hanks and H. Kanamori. A Moment Magnitude Scale. *J. Geophys. Res.*, 84(B5):2348–2350, 1979.
- [51] A. Helmstetter. Mainshocks are aftershocks of conditional foreshocks: How do foreshock statistical properties emerge from aftershock laws. *J. Geophys. Res.*, 108(B1):2046, 2003.
- [52] A. Helmstetter and D. Sornette. Bath’s law Derived from the Gutenberg-Richter law and from Aftershock Properties. *Geophys. Res. Lett.*, 30(20), 2003.
- [53] A. Helmstetter, Y. Y. Kagan, and J. D. D. Importance of small earthquakes for stress transfers and earthquake triggering. *J. Geophys. Res.*, 110(B5), 2005.
- [54] A. Helmstetterl and B. E. Shawl. Relation between stress heterogeneity and aftershock rate in the rate-and-state model. *J. Geophys. Res.*, 111(B7), 2006.
- [55] J. Henderson, I. Main, P. Meredith, and P. Sammonds. The evolution of seismicity at Parkfield: observation, experiment and a fracture-mechanical interpretation. *J. Struct. Geol.*, 14(8):905–913, 1992.
- [56] R. C. Hidalgo, F. Kun, and H. J. Herrmann. Bursts in a fiber bundle model with continuous damage. *Phys. Rev. E*, 64(6):066122, 2001.
- [57] G. W. Housner and M. D. Trifunac. Analysis of accelerograms–Parkfield earthquake. *Bull. Seismol. Soc. Am.*, 57(6):1193–1220, 1967.
- [58] M. Ishii, P. M. Shearer, H. Houston, and J. E. Vidale. Extent, duration and speed of the 2004 Sumatra-Andaman earthquake imaged by the Hi-Net array. *Nature*, 435:933–936, 2005.
- [59] E. A. Jagla and . Creep rupture of materials: Insights from a fiber bundle model with relaxation. *Phys. Rev. E*, 83(4):046119, 2011.
- [60] K. Janos. Fractal fracture. *Physica A*, 191:208–212, 1992.
- [61] Y. Y. Kagan. Universality of the Seismic Moment-frequency Relation. *Pure Appl. Geophys.*, 155(2-4):537–573, 1999.
- [62] Y. Y. Kagan. Short-Term Properties of Earthquake Catalogs and Models of Earthquake Source. *Bull. Seismol. Soc. Am.*, 94(4):1207–1228, 2004.

- [63] Y. Y. Kagan and H. Houston. Relation between mainshock rupture process and Omori's law for aftershock moment release rate. *Geophys. J. Int.*, 163(3): 1039–1048, 2005.
- [64] G. King, R. Stein, and J. Lin. Static stress changes and the triggering of earthquakes. *Bull. Seismol. Soc. Am.*, 84(3):935–953, 1994.
- [65] C. Kisslinger and L. M. Jones. Properties of Aftershock Sequences in Southern California. *J. Geophys. Res.*, 96(B7):947–958, 1991.
- [66] F. Kun, S. Zapperi, and H. Herrmann. Damage in fiber bundle models. *Eur. Phys. J. B*, 17:269–279, 2000.
- [67] F. Kun, Z. Halász, J. S. Andrade Jr, and H. J. Herrmann. Crackling noise in sub-critical fracture of heterogeneous materials. *J. Stat. Mech. Theory Exp.*, 01:P01021, 2009.
- [68] F. Lechenault, C. L. Rountree, F. Cousin, J.-P. Bouchaud, L. Ponson, and E. Bouchaud. Evidence of Deep Water Penetration in Silica during Stress Corrosion Fracture. *Phys. Rev. Lett.*, 106(16):165504, 2011.
- [69] S. Y. Lehman, E. Baker, H. a. Henry, A. J. Kindschuh, L. C. Markley, M. B. Browning, M. E. Mills, R. M. Winters, and D. T. Jacobs. Avalanches on a conical bead pile: scaling with tuning parameters. *Granul. Matter*, 14(5): 553–561, 2012.
- [70] O. Lengliné, B. Enescu, Z. Peng, and K. Shiomi. Decay and expansion of the early aftershock activity following the 2011, M w 9.0 Tohoku earthquake. *Geophys. Res. Lett.*, 39(18):n/a–n/a, 2012.
- [71] S. Lennartz, A. Bunde, and D. L. Turcotte. Missing data in aftershock sequences: Explaining the deviations from scaling laws. *Phys. Rev. E*, 78(4): 041115, 2008.
- [72] S. Lennartz-Sassinek, I. G. Main, Z. Danku, and F. Kun. Time evolution of damage due to environmentally assisted aging in a fiber bundle model. *Phys. Rev. E*, 88(3):032802, 2013.
- [73] E. Lippiello, L. D. Arcangelis, and C. Godano. Memory in self-organized criticality. *Europhys. Lett.*, 72(4):678–684, 2005.
- [74] E. Lippiello, L. de Arcangelis, and C. Godano. Influence of Time and Space Correlations on Earthquake Magnitude. *Phys. Rev. Lett.*, 100(2):038501, 2008.
- [75] E. Lippiello, L. de Arcangelis, and C. Godano. Role of Static Stress Diffusion in the Spatiotemporal Organization of Aftershocks. *Phys. Rev. Lett.*, 103(3): 038501, 2009.
- [76] E. Lippiello, C. Godano, and L. de Arcangelis. The earthquake magnitude is influenced by previous seismicity. *Geophys. Res. Lett.*, 39(5), 2012.
- [77] C. Lu, R. Danzer, and F. Fischer. Fracture statistics of brittle materials: Weibull or normal distribution. *Phys. Rev. E*, 65(6):067102, 2002.

- [78] K. J. Mäløy, S. Santucci, J. Schmittbuhl, and R. Toussaint. Local Waiting Time Fluctuations along a Randomly Pinned Crack Front. *Phys. Rev. Lett.*, 96(4):045501, 2006.
- [79] N. Mallick. *Exemples d'invariances d'échelle dans la fracture des matériaux fragiles désordonnés*. PhD thesis, Université Lyon 1, 2010.
- [80] B. B. Mandelbrot, D. E. Passoja, and A. J. Paullay. Fractal character of fracture surfaces of metals. *Nature*, 308:721–722, 1984.
- [81] D. Marsan and O. Lengliné. A new estimation of the decay of aftershock density with distance to the mainshock. *J. Geophys. Res.*, 115(B9):B09302, 2010.
- [82] W. Marzocchi and L. Sandri. A review and new insights on the estimation of the b-value and its uncertainty. *Ann. Geophys.*, 46(6), 2003.
- [83] D. Maugis. Review Subcritical crack growth, surface energy, fracture toughness, stick-slip and embrittlement. *J. Mater. Sci.*, 20(9):3041–3073, 1985.
- [84] T. A. Michalske and B. C. Bunker. Slow fracture model based on strained silicate structures. *Journal of Applied Physics*, 56(10), 1984.
- [85] T. A. Michalske and S. W. Freiman. A molecular interpretation of stress corrosion in silica. *Nature*, 295:511–512, 1982.
- [86] S. K. Midya and P. K. Gole. Variation of regional Gutenberg–Richter law parameter before and after large earthquakes in some earthquake prone zones around the world. *Indian J. Phys.*, 88(12):1227–1234, 2014.
- [87] K. Mogi. Magnitude-Frequency Relation for Elastic Shocks Accompanying Fractures of Various Materials and Some Related Problems in earthquakes. *Bull. Earthq. Res. Inst.*, 40:831–853, 1962.
- [88] K. Mogi. On the time distribution of aftershocks accompanying the recent major earthquakes in and near Japan. *Bull. Earthq. Res. Inst.*, 40:107–124, 1962.
- [89] K. Mogi. Some Discussions on Aftershocks, Foreshocks and Earthquake Swarms : the Fracture of a Semi-infinite Body Caused by an Inner Stress Origin and Its Relation to the Earthquake Phenomena (Third Paper). *Bull. Earthq. Res. Inst.*, 41:615–658, 1963.
- [90] K. Mogi. Earthquakes and fractures. *Tectonophysics*, 5(1):35–55, 1967.
- [91] G. M. Molchan, T. L. Kronrod, and A. K. Nekrasova. Immediate foreshocks : time variation of the b-value. *Phys. Earth Planet. Inter.*, 111:229–240, 1999.
- [92] J. Mori, Y. Kano, and B. Enescu. Comparison of early aftershock sequences for the 2004 Mid-Niigata and 2007 Noto Hanto earthquakes in central Japan. *Earth, Planets Sp.*, 60(2):151–154, 2008.
- [93] A. Nair and C. Cai. Acoustic emission monitoring of bridges: Review and case studies. *Eng. Struct.*, 32(6):1704–1714, 2010.

- [94] Y. Ogata. Statistical models for earthquake occurrences and residual analysis for point processes. *J. Am. Stat. Assoc.*, 83(401):9–27, 1988.
- [95] Y. Ogata. Seismicity Analysis through Point-process Modeling: A Review. *Pure Appl. Geophys.*, 155:471–507, 1999.
- [96] M. Ohnaka. *The Physics of Rock Failure and Earthquakes*. Cambridge University Press, 2013.
- [97] M. Ohtsu. The history and development of acoustic emission in concrete engineering. *Concr. Libr. JSCE*, (25):9–19, 1995.
- [98] I. O. Ojala. Strain rate and temperature dependence of Omori law scaling constants of AE data: Implications for earthquake foreshock-aftershock sequences. *Geophys. Res. Lett.*, 31(24), 2004.
- [99] T. Omi, Y. Ogata, Y. Hirata, and K. Aihara. Estimating the ETAS model from an early aftershock sequence. *Geophys. Res. Lett.*, 41:850–857, 2014.
- [100] R. Omori. On the Aftershocks of Earthquakes. *J. Coll. Sci. Imp. Univ. Japan*, 7:111–200, 1894.
- [101] I. Osorio, M. G. Frei, D. Sornette, J. Milton, and Y.-C. Lai. Epileptic seizures: Quakes of the brain? *Phys. Rev. E*, 82(2):021919, 2010.
- [102] D. Pantosti and G. Valensise. Faulting Mechanism and Complexity of the November 23 , 1980 , Campania- Lucania Earthquake , Inferred From Surface Observations. *J. Geophys. Res.*, 95(B10):15,319–15,341, 1990.
- [103] Z. Peng, J. E. Vidale, and H. Houston. Anomalous early aftershock decay rate of the 2004 Mw6.0 Parkfield, California, earthquake. *Geophys. Res. Lett.*, 33 (17):L17307, 2006.
- [104] Z. Peng, J. E. Vidale, M. Ishii, and A. Helmstetter. Seismicity rate immediately before and after main shock rupture from high-frequency waveforms in Japan. *J. Geophys. Res.*, 112(B3):B03306, 2007.
- [105] A. Petri, G. Paparo, and A. Vespignani. Experimental evidence for critical dynamics in microfracturing processes. *Phys. Rev. Lett.*, 73(25):3423–3426, 1994.
- [106] A. Politi, S. Ciliberto, and R. Scroretti. Failure time in the fiber-bundle model with thermal noise and disorder. *Phys. Rev. E*, 66(2):026107, 2002.
- [107] L. Ponson, D. Bonamy, and E. Bouchaud. Two-Dimensional Scaling Properties of Experimental Fracture Surfaces. *Phys. Rev. Lett.*, 96(3):035506, 2006.
- [108] S. Prades, D. Bonamy, D. Dalmas, E. Bouchaud, and C. Guillot. Nano-ductile crack propagation in glasses under stress corrosion: spatiotemporal evolution of damage in the vicinity of the crack tip. *Int. J. Solids Struct.*, 42(2):637–645, 2005.
- [109] S. Pradhan, A. Hansen, and B. K. Chakrabarti. Failure processes in elastic fiber bundles. *Rev. Mod. Phys.*, 82(1):499–555, 2010.

- [110] O. Ramos, E. Altshuler, and K. J. Må løy. **Quasiperiodic Events in an Earthquake Model.** *Phys. Rev. Lett.*, 96(9):098501, 2006.
- [111] O. Ramos, P.-P. Cortet, S. Ciliberto, and L. Vanel. **Experimental Study of the Effect of Disorder on Subcritical Crack Growth Dynamics.** *Phys. Rev. Lett.*, 110(16):165506, 2013.
- [112] J. Rosti, J. Koivisto, and M. J. Alava. **Statistics of acoustic emission in paper fracture: precursors and criticality.** *J. Stat. Mech. Theory Exp.*, page P02016., 2010.
- [113] S. Rubinstein, G. Cohen, and J. Fineberg. **Cracklike processes within frictional motion: is slow frictional sliding really a slow process?** *MRS Bull.*, 33:1181–1189, 2008.
- [114] S. M. Rubinstein, I. Barel, Z. Reches, O. M. Braun, M. Urbakh, and J. Fineberg. **Slip Sequences in Laboratory Experiments Resulting from Inhomogeneous Shear as Analogs of Earthquakes Associated with a Fault Edge.** *Pure Appl. Geophys.*, 168(12):2151–2166, 2011.
- [115] P. Rydelek and S. Sacks. **Testing the completeness of earthquake catalogues and the hypothesis of self-similarity.** *Nature*, 337:251–253, 1989.
- [116] M. R'Mili and J. Lamon. **Investigation of subcritical crack growth using load relaxation tests on fiber bundles.** *Acta Mater.*, 59(7):2850–2857, 2011.
- [117] M. R'Mili, M. Moevus, and N. Godin. **Statistical fracture of E-glass fibres using a bundle tensile test and acoustic emission monitoring.** *Compos. Sci. Technol.*, 68(7-8):1800–1808, 2008.
- [118] A. Saichev and D. Sornette. **Andrade, Omori, and time-to-failure laws from thermal noise in material rupture.** *Phys. Rev. E*, 71(1):016608, 2005.
- [119] L. I. Salminen, a. I. Tolvanen, and M. J. Alava. **Acoustic Emission from Paper Fracture.** *Phys. Rev. Lett.*, 89(18):185503, 2002.
- [120] S. Santucci, L. Vanel, and S. Ciliberto. **Subcritical Statistics in Rupture of Fibrous Materials: Experiments and Model.** *Phys. Rev. Lett.*, 93(9):095505, 2004.
- [121] S. Santucci, P.-P. Cortet, S. Deschanel, L. Vanel, and S. Ciliberto. **Subcritical crack growth in fibrous materials.** *Europhys. Lett.*, 74(4):595–601, 2006.
- [122] S. Santucci, L. Vanel, and S. Ciliberto. **Slow crack growth : models and experiments.** *Eur. Phys. J. Spec. Top.*, 146(341), 2007.
- [123] S. Santucci, M. Grob, A. Hansen, R. Toussaint, J. Schmittbuhl, and K. J. r. Må løy. **Fracture Roughness Scaling: a case study on planar cracks.** *Europhys. Lett.*, 92(4):44001, 2010.
- [124] S. Santucci, Stéphane; Cortet, Pierre-Philippe; Vanel, Loïc; Ciliberto. **Physics of Sub-critical Crack Growth in a Fibrous Material: Experiments and Model.** In *Proc. 11th Int. Congr. Fract. (ICF11)*, Turin, Italy, 2005.

- [125] C. Scholz. On the stress dependence of the earthquake b value. *Geophys. Res. Lett.*, pages 1–4, 2015.
- [126] C. H. Scholz. The frequency - magnitude relation of microfracturing in rock and its relation to earthquakes. *Bull. Seismological Soc. Am.*, 58(1):399–415, 1968.
- [127] C. H. Scholz. *The Mechanics of Earthquakes and Faulting*. Cambridge University Press, 2 edition, 1990.
- [128] D. Schorlemmer, S. Wiemer, and M. Wyss. Variations in earthquake-size distribution across different stress regimes. *Nature*, 437(7058):539–42, 2005.
- [129] B. E. Shaw. Constant Stress Drop from Small to Great Earthquakes in Magnitude-Area Scaling. *Bull. Seismol. Soc. Am.*, 99(2A):871–875, 2009.
- [130] R. Shcherbakov. A generalized Omori’s law for earthquake aftershock decay. *Geophys. Res. Lett.*, 31(11):L11613, 2004.
- [131] R. Shcherbakov. Statistical analysis of the 2010 MW 7.1 Darfield Earthquake aftershock sequence. *New Zeal. J. Geol. Geop.*, 55(3):305–311, 2012.
- [132] D. L. Shcherbakov, Robert; Turcotte. A Modified Form of Bath’s Law. *Bull. Seismol. Soc. Am.*, 94(5):1968–1975, 2004.
- [133] D. W. Smith. The b-value as an earthquake precursor. *Nature*, 289:136–139, 1981.
- [134] M. Spada, T. Tormann, S. Wiemer, and B. Enescu. Generic dependence of the frequency-size distribution of earthquakes on depth and its relation to the strength profile of the crust. *Geophys. Res. Lett.*, 40(4):709–714, 2013.
- [135] S. Steacy, J. Gomberg, and M. Cocco. Introduction to special section: Stress transfer, earthquake triggering, and time-dependent seismic hazard. *J. Geophys. Res.*, 110(B5):B05S01, 2005.
- [136] R. S. Stein and M. Lisowski. The 1979 Homestead Valley Earthquake Sequence, California: Control of Aftershocks and Postseismic Deformation. *J. Geophys. Res.*, 88(B8):6477–6490, 1983.
- [137] S. Stein and M. Liu. Long aftershock sequences within continents and implications for earthquake hazard assessment. *Nature*, 462(7269):87–9, 2009.
- [138] M. W. Stirling, S. G. Wesnousky, and K. Shimazaki. Fault trace complexity, cumulative slip, and the shape of the magnitude-frequency distribution for strike-slip faults: a global survey. *Geophys. J. Int.*, 124(3):833–868, 1996.
- [139] M. Stojanova, S. Santucci, L. Vanel, and O. Ramos. High Frequency Monitoring Reveals Aftershocks in Subcritical Crack Growth. *Phys. Rev. Lett.*, 112(11):115502, 2014.
- [140] I. Svetlizky and J. Fineberg. Classical shear cracks drive the onset of dry frictional motion. *Nature*, 509:205–208, 2014.

- [141] T. Tormann, S. Wiemer, and J. L. Hardebeck. **Earthquake recurrence models fail when earthquakes fail to reset the stress field.** *Geophys. Res. Lett.*, 39(18), 2012.
- [142] D. L. Turcotte, J. R. Holliday, and J. B. Rundle. **BASS, an alternative to ETAS.** *Geophys. Res. Lett.*, 34(12):L12303, 2007.
- [143] T. Utsu. **Aftershocks and Earthquake Statistics (I) -Some Parameters Which Characterize an Aftershock Sequence and Their Interrelations.** *J. Fac. Sci. Hokkaido Univ.*, 3(3):129–195, 1969.
- [144] T. Utsu, Y. Ogata, and R. S. Matsu’ura. **The Centenary a Decay of the Omori Formula Activity for Law of Aftershock.** *J. Phys. Earth*, 43:1–33, 1995.
- [145] L. Vanel, S. Ciliberto, P.-P. Cortet, and S. Santucci. **Time-dependent rupture and slow crack growth: elastic and viscoplastic dynamics.** *J. Phys. D. Appl. Phys.*, 42(21):214007, 2009.
- [146] T. H. W. Goebel, D. Schorlemmer, T. W. Becker, G. Dresen, and C. G. Sammis. **Acoustic emissions document stress changes over many seismic cycles in stick-slip experiments.** *Geophys. Res. Lett.*, 40(10):2049–2054, 2013.
- [147] N. W. Warren and G. V. Latham. **An experimental study of thermally induced microfracturing and its relation to volcanic seismicity.** *J. Geophys. Res.*, 75 (23):4455–4464, 1970.
- [148] J. Weiss, T. Richeton, F. Louchet, F. Chmelik, P. Dobron, D. Entemeyer, M. Lebyodkin, T. Lebedkina, C. Fressengeas, and R. J. McDonald. **Evidence for universal intermittent crystal plasticity from acoustic emission and high-resolution extensometry experiments.** *Phys. Rev. B*, 76(22):224110, 2007.
- [149] S. M. Wiederhorn. **Crack Propagation in Soda-Lime Glass.** *J. Am. Ceram. Soc.*, 50(8):407–414, 1967.
- [150] S. M. Wiederhorn and L. H. Bolz. **Stress Corrosion and Static Fatigue of Glass.** *J. Am. Ceram. Soc.*, 53(10):543–548, 1970.
- [151] S. Wiemer and M. Wyss. **Mapping the frequency-magnitude distribution in asperities. An improved technique to calculate recurrence times.** *J. Geophys. Res.*, 102(B7):15,115–15,128, 1997.
- [152] S. Wiemer and M. Wyss. **Minimum magnitude of completeness in earthquake catalogs: examples from Alaska, the western United States, and Japan.** *Bull. Seismol. Soc. Am.*, (August):859–869, 2000.
- [153] S. Wiemer and M. Wyss. **Mapping spatial variability of the frequency-magnitude distribution of earthquakes.** *Adv. Geophys.*, 45:259–302, 2002.
- [154] S.-D. Zhang and E.-J. Ding. **Failure of fiber bundles with local load sharing.** *Phys. Rev. B*, 53(2):646–654, 1996.
- [155] Y. Zhou, M. a. Baseer, H. Mahfuz, and S. Jeelani. **Statistical analysis on the fatigue strength distribution of T700 carbon fiber.** *Compos. Sci. Technol.*, 66 (13):2100–2106, 2006.

- [156] A. Ziv, A. M. Rubin, and D. Kilb. Spatiotemporal Analyses of Earthquake Productivity and Size Distribution : Observations and Simulations. *Bull. Seismol. Soc. Am.*, 93(5):2069–2081, 2003.
- [157] F. Zúñiga and M. Wyss. Inadvertent changes in magnitude reported in earthquake catalogs: Their evaluation through b-value estimates. *Bull. Seismol. Soc. Am.*, 85(6):1858–1866, 1995.

CONTENTS

Introduction	1
1 Subcritical fracture	3
1.1 Stress concentration	3
1.2 Griffith's energy balance	4
1.3 The role of the disorder	5
2 Fracture and earthquakes	6
3 Power laws	7
3.1 Power-law distributed energies The Gutenberg-Richter law	8
3.2 Power-law distributed occurrence times The Omori law	9
4 Thesis summary	9

I Experiments on subcritical fracture	11
1 Fracture propagation in paper. The effects of time correlation	13
1 Introduction	14
1.1 Why paper?	14
1.2 Previous creep experiments on paper	14
1.3 Motivation	15
2 The experiment	16
2.1 Data recording	17
2.2 Data analysis	17
2.2.1 Image analysis	17
2.2.2 Acoustic emission analysis	18
2.3 Details about the acoustic emissions	18
3 Results	19
3.1 First observations	19
3.2 A rough comparison between acoustics and visualisation	20
3.3 Probability distributions of time and energy	22

3.3.1	Waiting times	22
3.3.2	Energies	22
3.4	The influence of the acquisition frequency	24
3.5	Aftershocks	26
4	Conclusion	27
5	Perspectives	28
2	Fracture of a fibre bundle: experiments and model	31
1	Introduction	32
2	Model on thermally activated rupture in fibre bundles	33
2.1	The democratic fibre bundle model with thermal noise Previous results on creep simulations	33
2.2	Simulations at constant strain	34
2.2.1	Results	35
3	Experiments on bundle fracture	39
3.1	Stress corrosion of glass	39
3.2	Experimental procedure	40
3.3	Analysing the acoustic events	42
3.4	Some basic considerations on mechanics	43
3.5	Strength distribution of fibres	43
3.6	Experimental results	44
3.6.1	A typical experiment	44
3.6.2	Total number of broken fibres	45
3.6.3	Omori law	46
4	Comparing experiments and simulations	49
5	Conclusion and perspectives	49
II	Earthquake statistics	51
3	Some history and a few technicalities	53
1	Introduction	54
1.1	Time clustering of earthquakes	54
1.2	Our focus: mainshock-aftershock sequence	55
2	The statistics of aftershocks - a matter of details	55

2.1	The well known (power) laws	55
2.1.1	Omori law	56
2.1.2	Gutenberg-Richter law	57
2.1.3	Båth law	58
2.1.4	Spatial distribution of aftershocks	60
2.2	Short time aftershock incompleteness - STAI	60
2.2.1	STAI and Omori law's c value	61
2.2.2	STAI and magnitudes statistics	62
2.3	Magnitude correlation	62
2.4	b-value and differential stress	62
2.5	Earthquake triggering	63
2.5.1	Static triggering	63
2.5.2	Dynamic triggering	64
2.6	The challenge of studying earthquakes	64
2.6.1	The main problems	65
3	Methods	66
3.1	Data collection	66
3.1.1	Defining an earthquake sequence	66
3.2	Extracting the power law exponent	66
3.2.1	Estimating the exponent of a power law	67
3.2.2	Determining the power-law span	69
3.3	Dealing with STAI	72
3.4	Simulations The Branching Aftershock Sequence Model	72
4	b-value and the frequency of analysis	75
1	Motivations	76
2	First observations on simulations	77
2.1	The origin of the power law crossover	78
2.1.1	The role of the Omori law	80
3	What does b_I depend on? A numerical study	82
3.1	Results	83
3.1.1	The importance of temporal correlations	83

3.1.2	The influence of other parameters	83
3.1.3	Linking b_2 to b and p	84
4	Comparison with the experimental data	86
5	Magnitude correlation	88
5.1	Magnitude correlations in the case of one-generation simulated sequences The effect on the b-value decrease	88
5.2	b-value variation of real aftershock sequences	88
6	Conclusion and perspectives	89
5	Early aftershocks	91
1	Introduction	92
2	Magnitude correlations	93
2.1	Method	93
2.1.1	Converting the power-law of times into a uniform distribution	93
2.1.2	What will we measure?	94
2.2	Results	96
2.2.1	Japan earthquakes	96
2.2.2	California earthquakes	97
2.3	Discussion	98
3	Temporal variations of the b-value	99
3.1	State of the art	99
3.1.1	Short-time, local b-value variation	99
3.1.2	The link with magnitude correlation and stress release	100
3.2	Methods	100
3.3	Results	101
3.3.1	Observations	101
3.3.2	Quantitative results	101
4	Conclusion	104
Conclusion		105

Appendices	107
A Spectral distance	107
B Experimental procedure for fibre bundle fracture	109
B.1 Bundle preparation	109
B.2 Experimental set-up	109
B.3 Experimental protocol	111
C Details about the fibre bundle experiments	113
C.1 Some basic considerations on mechanics	113
C.2 The fibres' strength	114
D Details on the earthquake sequences used for the analysis of the b-value decrease with f_a	117
D.1 JMA catalogue	117
D.1.1 SCSN catalogue	118
D.1.2 NCSN catalogue	118
E Details on the earthquake sequences used in chapter 5	119
E.1 Sequences for magnitude correlation analysis	119
E.1.1 Japan earthquakes	119
E.1.2 California earthquakes	120
E.2 Details on the b-value variation analysis	122